Characterisation of 64 channel SiPM arrays for the Silicon Elementary Cell Add-on

Charakterisierung von 64-Kanal SiPM-Arrays für das Silicon Elementary Cell Add-On

Master Thesis of

Max Renschler

at the
KIT - Department of Physics
Institut für Kernphysik (IKP)

Reviewer:	Prof. Johannes Blümer
Second reviewer:	Prof. Ivan Perić
Advisor:	Dr. Andreas Haungs

July 2015 – July 2016

I declare that I have developed and written the enclosed thesis completely by myself, and have not used sources or means without declaration in the text.

Karlsruhe, July 2016

. . . .

(Max Renschler)

CHARACTERISATION OF 64 CHANNEL SIPM ARRAYS FOR THE SILICON ELEMENTARY CELL ADD-ON

To essentially contribute to the research of ultra-high energy cosmic rays, the Extreme Universe Space Observatory onboard the Japanese Experimental Module (JEM-EUSO) is currently under development. The aim of JEM-EUSO is to increase the statistics of detected ultra-high energy cosmic rays with energies in the range of $10^{19} - 10^{21}\ eV$. The base-line design of JEM-EUSO provides a $4\,\mathrm{m}^2$ focal surface consisting of around 5000 photomultiplier tubes. Due to the progress in the field of semi-conductor based photo detectors, options of replacing the standard-design photomultiplier tubes with Silicon Photomultiplier (SiPM) are investigated. To test SiPM in active operation of cosmic ray detection, the Silicone Elementary Cell Add-On (SiECA) is developed at KIT. SiECA is an add-on to the JEM-EUSO pathfinder experiment EUSO-SPB in which a down-scaled version of the JEM-EUSO detector will be tested during a long duration super pressure balloon flight.

During this thesis, a measurement setup consisting of printed circuit boards as well as measurement control and analysing software was developed to characterize 64 channel SiPM arrays of the newest generation. The build-up measurement was used to test two different series SiPM arrays manufactured by Hamamatsu for their abilities of a use within SiECA. Suitable is found to be the SiPM array *S13361-3050AS-08*. The average measured breakdown voltage of the array is $(51.65 \pm 0.12)\,\mathrm{V}$, the average gain is measured to $(2.12 \pm 0.7) \cdot 10^6$, the average photo detection efficiency results to $(44.60 \pm 1.78)\%$, the average dark-count rate is $(0.68 \pm 0.11)\,\mathrm{MHz}$ and the crosstalk probability is measured to $(3.90 \pm 0.66)\%$. The uniformity over the whole array is sufficient in the characteristic parameters to build up a focal surface of SiPM arrays fulfilling the requirements for such a camera.

The performed measurements show that the new-series SiPM array has important improvements in all the tested characteristics compared to earlier series SiPM arrays and can compete against conventional photomultiplier tubes. In addition, the manufacturers rough information on these SiPM characteristics are confirmed. Temperature dependent measurements were performed to investigate the high temperature dependency of several SiPM characteristics. These temperature dependent measurements confirm the effects of a changing ambient temperature on the SiPM characteristics and imply a cooling system for further SiPM-based JEM-EUSO-like focal surface detectors.

CHARAKTERISIERUNG VON 64-KANAL SIPM-ARRAYS FÜR DAS SILICON ELEMENTARY CELL ADD-ON

Um entscheidend zu der Erforschung der kosmischen Strahlung beizutragen, wird derzeit das Extreme Universe Space Observatory angedockt an das Japanese Experimental Module (JEM-EUSO) der Internationalen Raumstation entwickelt. Ziel des JEM-EUSO Experiments ist es, die Statistik der detektierten kosmischen Teilchen mit Energien von $10^{19} - 10^{21}$ eV bedeutend zu erhöhen. In der geplanten Standardausführung von JEM-EUSO ist eine photosensitive Fokalfläche von $4\,\mathrm{m}^2$ bestehend aus etwa 5000 Photomultiplier Röhren (PMTs) vorgesehen. Aufgrund der stetigen Entwicklung im Bereich der auf Silizium basierten Photodetektoren, wird der Einsatz von 'Silicone Photomultiplier' (SiPM) an Stelle von konventionellen PMTs in Betracht gezogen. Um SiPM unter realen Messbedingungen zu testen, wird derzeit am KIT das 'Silicon Elementary Cell Add-On' (SiECA) entwickelt. SiECA ist eine Erweiterung des JEM-EUSO Pfadfinder Experiments EUSO-SPB, bei dem die Detektion von kosmischer Strahlung mit einem verkleinerten, JEM-EUSO ähnlichen Teleskop während eines Hochdruckballonflugs getestet wird.

Im Rahmen dieser Masterarbeit wurde ein Messaufbau zur Charakterisierung von 64-Kanal SiPM-Arrays der neusten Generation bestehend aus mehreren Ausleseplatinen, Messsteuerung- und Analysesoftware entwickelt. Mit diesem Aufbau wurden zwei SiPM Arrays aus verschiedenen Modellreihen des Herstellers Hamamatsu auf ihre Eignung getestet bei SiECA eingesetzt zu werden. Als am besten geeignet stellte sich das SiPM Array *S13361-3050AS-08* der neusten Modellreihe heraus. Die gemessene und über das gesamte Array gemittelte Durchbruchspannung ist $(51.65 \pm 0.12)\,\mathrm{V}$, der mittlere Gain ist $(2.12 \pm 0.7) \cdot 10^6$, die Messung der mittleren Photodetektionseffizienz ergab $(44.60 \pm 1.78)\%$, die mittlere Dunkelzählrate ist $(0.68 \pm 0.11)\,\mathrm{MHz}$ und die Messung der Wahrscheinlichkeit eines Crosstalk Ereignisses ergab $(3.90 \pm 0.66)\%$. Die Uniformität der einzelnen SiPM Kanäle ist in den gemessenen charakteristischen Parametern hinreichend groß, um eine SiPM basierte Fokalfläche zu realisieren, die die Bedingungen einer solchen Kamera erfüllt.

Die Messungen zeigen, dass das SiPM Array der neueren Modellreihe in allen untersuchten Belangen Vorteile gegenüber dem älteren Modell bietet. Die Charakteristika der gemessenen SiPM sind vergleichbar mit denen konventioneller Photomultiplier Röhren. Außerdem konnten die Messungen die nur grob angegebenen Herstellerangaben über verschiedene SiPM Charakteristika bestätigen. Um das Verhalten von SiPM bei unterschiedlichen Temperaturen zu untersuchen, wurden temperaturabhängige Messungen verschiedener SiPM Eigenschaften durchgeführt. Die Ergebnisse der temperaturabhängigen Messungen bestätigen die starke Abhängigkeit der SiPM von der Umgebungstemperatur und legen ein Kühlung von aus SiPM bestehenden Fokalflächen in weiterführenden JEM-EUSO-ähnlichen Experimenten nahe.

CONTENTS

1

INTRODUCTION

Cosmic-rays are the most energetic particles that ever have been detected by humanity. Particle accelerators like the Large Hadron Collider (LHC), which is for now the most powerful particle accelerator built by human beings, has an energy limit in the TeV range (10^{12} eV) [1]. In contrast, galactic and extra-galactic sources accelerate charged particles to energies of hundreds of EeV (10^{18} eV) and most probably even above. Detecting and investigating these Ultra-High Energy Cosmic Rays (UHECRs) contributes to our knowledge about particle physics in a kind that maybe never can be reached by human-build accelerator experiments [2].
Beside of this, the observation of cosmic rays opens a not substitutable new window to the galactic and the extra-galactic cosmos which surrounds our Earth. Cosmic accelerators of UHECRs might be the most powerful objects in space and their exploration will definitely increase our knowledge about the history of our mysterious Universe. In addition, the investigation of UHECRs can give information about the magnetic fields in our galactic environment, it can test the special relativity and and can give information about more exotic physics like loop quantum gravity, the existence of strangelets and possible Lorentz invariance violation [3–6]. Due to low statistics of detected UHECRs, no individual source have been identified so far. Also, the mechanisms which accelerate charged particles to extreme energies are not unveiled.
The key for all these information obtainable by cosmic ray research is a better statistics of detected events of UHECRs with energies of around 10^{20} eV. Due to limitations of geographical or financial kind, ground-based experiments like the Pierre Auger Observatory in Argentina [7], which is the worldwide largest cosmic ray observatory, can not increase their observation area in a sufficient way in the next decades. A solution for this is to not detect cosmic rays from ground by looking to the sky, but to observe air showers induced by ultra-high energetic particles from space by looking down to the Earth's atmosphere. With this new approach, the observation area can be increased by about 50 times the actual observation area of Auger [8]. A proposed mission using this detection method is the Extreme Universe Space Observatory onboard the Japanese Experimental Module (JEM-EUSO). JEM-EUSO is proposed to be attached to the International Space Station and will measure cosmic ray air showers by detecting fluorescence light emitted during a shower event with a full sky coverage and an observation area of around 10^5 km^2 [9].

Due to the low number of fluorescence photons (~ 400/GTU[2] [10]) which reach the

---

[2] Gate Time Unit = 2.5μs

JEM-EUSO telescope in a height of around 400 km above ground, very sensitive photo detectors have to be chosen with the capability of detecting single photons. In the baseline design of JEM-EUSO, Multi Anode Photomultiplier Tubes (MAPMTs) with 64 channels each are foreseen as photo detectors. In the last few years, photo detectors based on silicon - Silicon Photomultiplier (SiPM) - made great progress which make them comparable to conventional PMTs. Compared to PMTs, SiPM have several advantages like a low operation voltage of below 70 V and a lightweight and robust structure, which both is benefiting especially regarding an operation in space. To discover the possibility of replacing the standard-design MAPMTs with SiPM in the JEM-EUSO experiment, work on a photo detection device build out of SiPM (Silicon Elementary Cell Add-On, SiECA) is ongoing at KIT which will test the SiPM in operation during a long duration super pressure balloon flight in 2017.

Within this thesis, a SiPM characterizing measurement setup consisting of several printed circuit boards as well as measurement and analysis software has been designed and brought into operation. With this setup, two series of 64 channel SiPM arrays manufactured by Hamamasu have been measured in order to find the more suitable for a use in SiECA. One of the tested SiPM arrays belongs to the newest generation of 64 channel SiPM arrays and has never before been characterized in such an extended detail by an independent facility.

In the second chapter of this thesis, cosmic rays and extensive air showers are introduced and the detection of cosmic rays by measuring fluorescence light emitted during an air shower is described.

The JEM-EUSO experiment together with several pathfinder missions is presented in chapter three. SiECA, as an add-on to the pathfinder experiment EUSO-Super Pressure Balloon, will be described in more details.

In chapter four, Silicon photomultiplier will be introduced. The working principle of SiPM will be explained, the two tested SiPM arrays will be presented and the characterizing process of SiPM is described in detail.

The preparations of the measurements, like the designed printed circuit boards and the measurement control and analysing software, and the measurement setup is introduced in the chapters five and six.

The measurement results are presented in chapter seven. Together with the results, a comparison of the measured results and the manufacturers information and a comparison of the measured SiPM characteristics of the two different SiPM series is given to identify the more suitable SiPM array for SiECA.

2

COSMIC RAYS AND DETECTION METHODS

In the early 20th century, it was a common opinion that atmospheric electricity comes from the radiation of radioactive elements in the ground. First Victor Hess found out that the origin of the atmospheric electricity is not the ground but the cosmos by performing balloon experiments measuring the ionization of the air to heights up to 5300 m above ground [11]. In the 1930's, Bruno Rossi and Pierre Auger independently found evidences for extensive air showers by observing coincidental events in remote Geiger counters [12] [13]. Auger suggested, that these air showers are generated by a cosmic ray particle interacting with the Earth's atmosphere and initialising a shower of photons and electrons by secondary interactions.

Cosmic ray measurements with an array of detectors were first performed 1954 by the Rossi Cosmic Ray Group at the MIT[2] by deploying eleven scintillation detectors at Agassiz Station of the Harvard College Observatory [14]. Nowadays, the two leading cosmic ray observatories for the highest energies are the Pierre Auger Observatory in Argentina and the Telescope Array (TA) in Utah, USA which investigate extensive air showers induced by cosmic rays with a primary energy of up to 10^{20} eV [7, 15].

In this chapter, Cosmic Rays (CRs) and Extensive Air Showers (EAS) will be briefly introduced and the detection methods of EAS will be described.

COSMIC RAYS

The Earth's atmosphere is exposed continuously to the impact of charged particles and photons which have their origin in the cosmos. This cosmic radiation consists mainly of ionised atomic nuclei. Electrons and photons contribute only with around 2% to the total number of cosmic-ray particles (table 2.1).

Protons	85%
Helium nuclei	12%
Nuclei with $Z \geqslant 3$	1-2%
Electrons and positrons	1-2%
Photons	0.1%

Table 2.1: Composition of the cosmic-ray particles up to an energy of 10^{12} eV [16].

---

[2] Massachusetts Institute of Technology

Figure 2.1 shows the elemental distribution of cosmic rays in the low energy range (TeV). A higher occurrence for elements with a smaller atomic number than iron (Z=26) is visible.

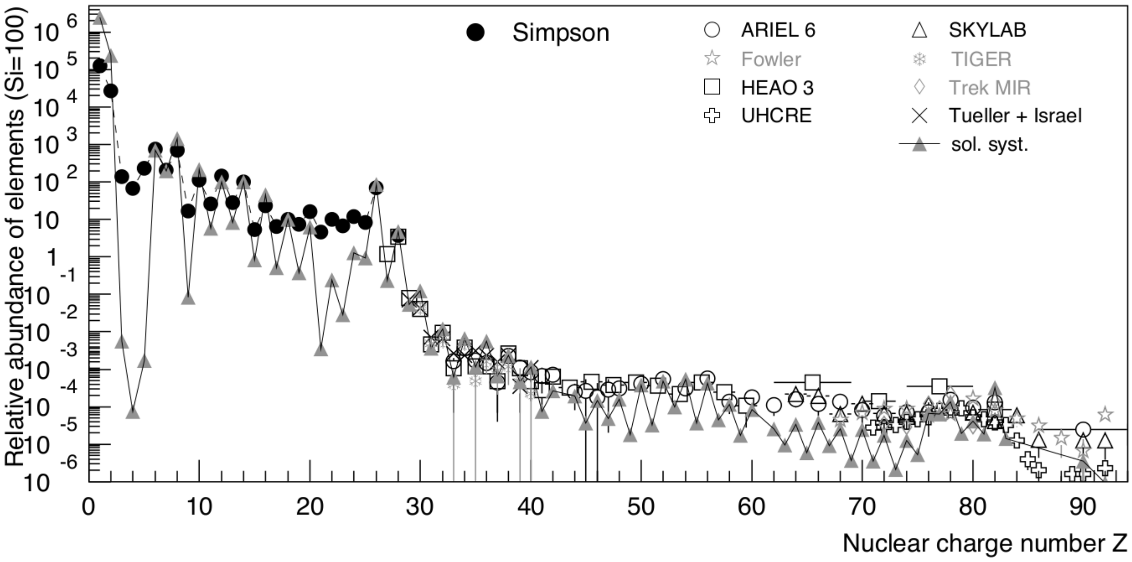

Figure 2.1: Relative abundance of cosmic rays in the solar system for low energies. The relative abundance is shown normalized to silicon [17].

An explanation for this rareness of elements with an atomic number higher than 27 is the interaction of heavy nuclei with the interstellar medium.
Comparing the composition of the cosmic rays with the element distribution in our solar system (fig. 2.1), similarities are visible. Since elements with even atomic number are more stable due to their higher nuclear binding energy, these elements have higher abundances in both the cosmic ray and the solar system element composition.
Discrepancies of the elemental compositions of low energy cosmic rays and the solar system are visible for elements of low atomic numbers of around 4 and for elements of atomic numbers of around 24. In both cases the cosmic-ray composition has a higher frequency of elements in this regions of atomic numbers compared to the elemental composition of the solar system. The reason for these discrepancies is the spallation of the elements ^{12}C and Fe in the cosmos enriching the cosmic-ray spectrum with their spallation products.

Energy spectrum of cosmic rays

The energy spectrum $\phi(E)$ of the cosmic-ray particles impacting on the Earth's atmosphere follows a power law behaviour of the form

$$\phi(E) \sim E^{-\gamma}. \tag{2.1}$$

Figure 2.2 shows the energy spectrum of the cosmic-ray particles obtained by many experiments above the atmosphere and on ground. In the energy spectrum, three features are visible. First, the gradient of the spectrum changes from $\gamma = 2.7$ to $\gamma = 3.1$ at an energy of around $4 \cdot 10^{15}$ eV ("knee") [17]. At an energy of around 10^{18} eV the spectrum flattens again ("ankle"). After an energy of around $5 \cdot 10^{18}$ eV the flux of the ultra-high energetic cosmic rays drops sharply with increasing energy of the particles.

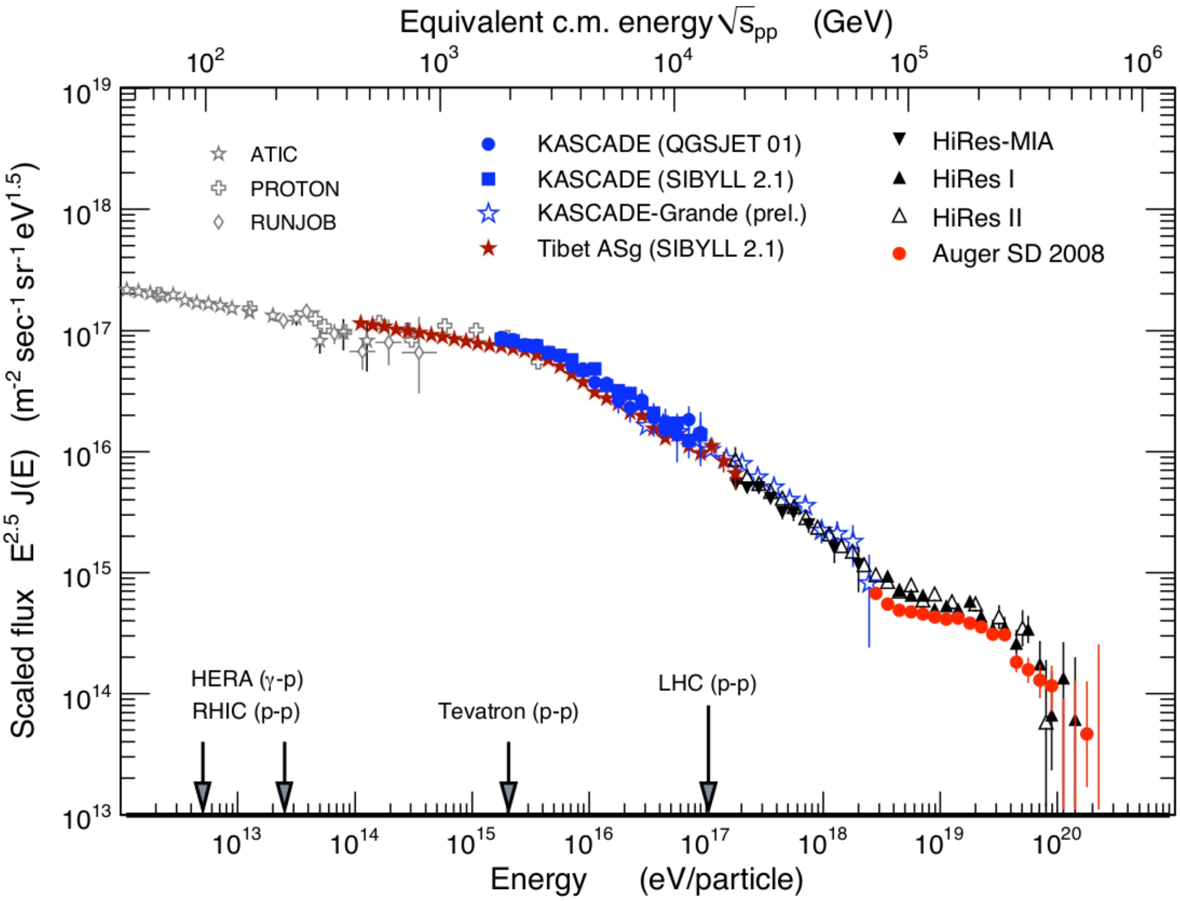

Figure 2.2: All-particle energy spectrum of the cosmic-ray particles multiplied with a factor of $E^{2.5}$ [17].

A reason for the 'knee' in the spectrum at energies around $4 \cdot 10^{15}$ eV is the decrease of the particle flux of light elements [18]. The ankle, the flattening of the flux between 10^{18} eV and 10^{19} eV, can have two possible reasons. The ankle is traditionally seen as the transition of galactic to extra-galactic sources of the cosmic-ray particles. In this scenario, cosmic rays with an extra-galactic origin dominate the flux for energies above about 10^{19} eV [17]. Second, the energy of protons is in this energy regime high enough to produce an electron-position pair during an interaction with the cosmic microwave background photons (dip model)

$$p + \gamma = p + e^- + e^+. \tag{2.2}$$

Considering only protons as cosmic rays, this also could explain the flattening of the flux between 10^{18} eV and 10^{19} eV.

Above energies of about $5 \cdot 10^{19}$ eV the flux of the cosmic rays drops sharply. The rate of cosmic-ray particles at energies of 10^{20} eV equals one particle per square kilometre per century. Possible explanations for this are missing accelerators for particles in this energy regime and the GZK[1]-effect. The GZK-effect describes the interaction of high-energy protons ($E > 5 \cdot 10^{19}$ eV) with the Cosmic Microwave Background (CMB). Protons can interact with the photons of the CMB, produce pions and loose energy during this process

$$p + \gamma \rightarrow \Delta^+ \rightarrow p + \pi^0, n + \pi^+. \tag{2.3}$$

Due to the GZK-effect, protons with higher energies than 10^{20} eV decelerate to energies less than 10^{20} eV within distances of around 100 Mpc.

The answer to the question, whether the GZK-effect or the lack of suitable particle accelerators is responsible for the drop of the flux at energies around $5 \cdot 10^{19}$ eV is still subject of research. Regarding the low flux of one particle per square kilometre per century for cosmic-ray particles of the highest energies, the measured statistics of detected events has to be increased to obtain further information. A way to increase the measured statistics is to increase the observation area in which cosmic rays can be detected. To increase the observation area might be possible by looking from space down to the Earth's atmosphere as proposed for the JEM-EUSO experiment.

EXTENSIVE AIR SHOWERS

Cosmic-ray particles which interact with molecules in the Earth's atmosphere produce a cascade of secondary interactions. This cascade is called Extensive Air Shower (EAS). Figure 2.3 shows a sketch of the composition of an EAS. The EAS cascade has a hadronic, a muonic and an electro-magnetic component. In the first interaction of a cosmic ray particle and an air molecule, mainly pions and kaons are produced. Via inelastic scattering and hadronic interactions, new hadronic particles are generated (hadronic component) which are the source for the other two components of an EAS.

Charged pions and kaons belonging to the hadronic cascade can decay into muons and neutrinos, which build the muonic component of the EAS. Due to the small muon cross-section this component can penetrate deeply into the ground.

With the decay of neutral pions into photons, the electro-magnetic cascade starts. During the cascade, photons generate an electron-positron pair via pair production and

---

[1] Greisen, Zatsepin, Kuzmin

the electrons and positrons emit photons as bremsstrahlung. The cascade stops when the bremsstrahlung cross-section becomes smaller than the ionisation cross-section at an energy limit ϵ.

The *Heitler model* describes the growth of the electromagnetic component of an EAS in more detail. Since the cascade is driven by the processes of bremsstrahlung and pair production, the *Heitler model* describes a doubling of the number of particles in the cascade for every interaction. For n interactions, the number of particles $N(x)$ in the electro-magnetic component is

$$N(x) = 2^n \tag{2.4}$$

where x is the shower length in the atmosphere. The creation of new particle stops when the energy limit ϵ is reached. The maximum number of particles in the cascade is

$$N_{max} = \frac{E}{\epsilon} \tag{2.5}$$

with the energy E of the primary cosmic-ray particle. Combining both equations and considering a constant interaction length λ between two interactions in the electro-magnetic cascade, the height of the shower maximum can be calculated as

$$x_{max} = \frac{\lambda}{\ln(2)} \cdot \ln\left(\frac{E}{\epsilon}\right). \tag{2.6}$$

With the relationships $N_{max} \sim E$ and $x_{max} \sim \ln(E)$ the energy of the primary cosmic ray particle can be derived by measuring the EAS generated by it.

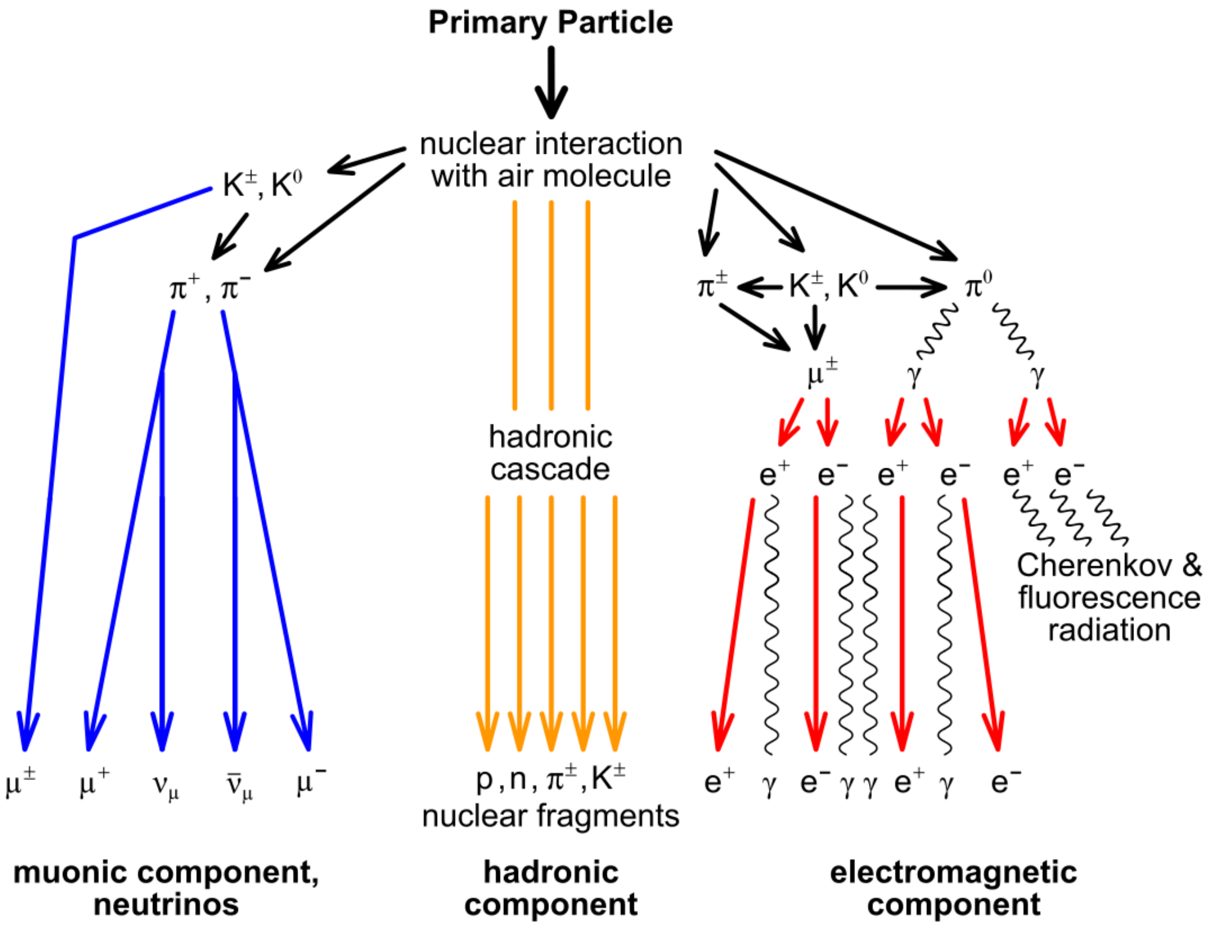

Figure 2.3: Schematic view of the composition of an EAS. The primary cosmic-ray particle interacts with an air molecule and produces a cascade with a hadronic, a muonic and an electro-magnetic component [19].

To obtain information about the direction of the cosmic ray particle, for example the relative arrival times of the EAS particles on ground can be measured. Especially for cosmic-ray particles of highest energies the information of their arrival direction is important since these particles are only slightly deflected by the galactic magnetic fields and can point towards the source they came from.

DETECTION METHODS

Cosmic rays can be detected by direct measurements or by detecting and measuring the EAS produced by them. In direct measurements, the cosmic-ray particle is detected above the Earth's atmosphere by satellite- or balloon-based experiments. This kind of detection method is only suitable for cosmic rays with energies lower than around

10^{15} eV since the flux of the cosmic rays becomes too low for higher energies. Also the high energy itself makes a proper measurement of the cosmic rays abilities difficult for flying experiments regarding the needed size of the detector.
Due to their low flux and high energy, cosmic rays with energies above circa 10^{15} eV can only be measured by detecting EAS and measuring their various components. The electrons, positrons and muons of an EAS can be measured by using Cherenkov water detectors or scintillation detectors like it was done at KASCADE-Grande [20]. Also radio emission signals around a frequency of 50 MHz can be observed during an EAS and can be used to draw conclusions about the EAS and the primary cosmic ray particle, which is a rather new field of research investigated for example by AERA[1] [21]. Last, fluorescence light emitted by excited nitrogen during an EAS can give direct information about the longitudinal profile of air showers with energies above circa 10^{17} eV. Hybrid approaches of combined ground-based particle detection with Cherenkov water detectors and fluorescence light detection with telescopes are used in the Pierre Auger Observatory and Telescope Array [22, 23]. Since JEM-EUSO will measure EAS mainly by detecting fluorescence light emitted by exited nitrogen, this method will be presented in more detail.

Detection of cosmic rays with fluorescence light

Fluorescence means the emission of light by an energy state which has been excited by electro-magnetic radiation or any other energy deposition. Fluorescence light is emitted isotropically when the excited substance relaxes to its ground state. The wavelength of the emitted fluorescence light depends on the energy difference between the initial state E_I and the final ground state E_F

$$\lambda = \frac{hc}{E_I - E_F}. \tag{2.7}$$

Regarding EAS, the observed fluorescence light is emitted by excited nitrogen molecules which emit fluorescence light in the UV region (fig. 2.4). The quantity of fluorescence light during an EAS is proportional to the energy deposited in the atmosphere. Therefore, a conclusion about the number of particles in the shower is possible by measuring the fluorescence light produced during the EAS. Nitrogen has excitation stages that can be divided in vibrational states, rotational states and electronic states. A relaxation of an electronic excitation state to the ground state leads to the emission of a fluorescence photon. For a nitrogen molecule, two transitions of electronic states are possible, called *2P* (second positive transition) and *1N* (first negative transition). A further splitting of the fluorescence spectrum has its origin in the additional changes of vibrational and rotational states during the change of the electromagnetic state (see fig. 2.4) [17, 24].

---

[1] Auger Engineering Radio Array

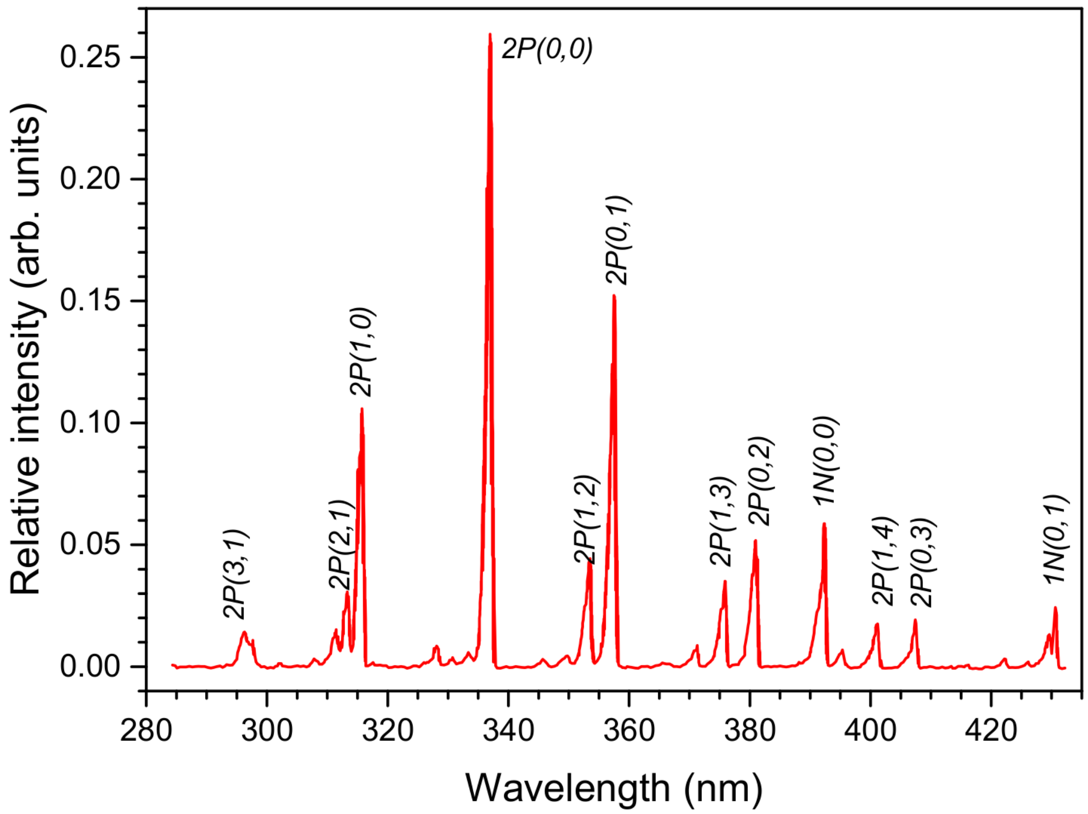

Figure 2.4: Spectrum of the fluorescence emission of nitrogen in units of relative intensity (adopted from [19]).

Figure 2.4 shows the fluorescence spectrum of nitrogen in the UV range of $280\,\mathrm{nm}$ to $430\,\mathrm{nm}$. The most intense emission is at a wavelength of around $337.1\,\mathrm{nm}$.

The first fully functional fluorescence air shower detector was the Fly's Eye experiment consisting of two detector stations (Fly's Eye I and II) which started operation in the year 1982 in Utah, USA. With the Fly's Eye I detector the until now most energetic cosmic ray event with an energy of $(3.2 \pm 0.9) \cdot 10^{20}$ eV was detected in the year 1991 [17].

With the JEM-EUSO experiment, a space-based fluorescence telescope is planned which is going to improve the measurement statistics of these ultra-high cosmic ray events.

3

EXTREME UNIVERSE SPACE OBSERVATORY ONBOARD THE JAPANESE EXPERIMENT MODULE (JEM-EUSO)

To obtain information about the high energy universe, the JEM-EUSO mission was established to detect and measure cosmic-ray events with energies above 10^{19} eV. The observation of these Ultra-High Energy Cosmic Ray (UHECR) events is not only important to increase the statistics of detected events in this ultra-high energy regime but also to find individual extra-galactic sources of cosmic-ray particles. Since cosmic rays with energies above $8 \cdot 10^{19}$ eV are only slightly deflected in the galactic magnetic field, the arrival direction of an UHECR event can point towards the source, if it is close enough. This will enable the opportunity to make astronomy with cosmic rays.
Contemporary ground based cosmic-ray observatories like the Pierre Auger Observatory or the Telescope Array are limited in available observation area due to geographical or financial reasons. The idea behind the JEM-EUSO mission is to observe the Earth's atmosphere from space and thereby increase the available observation area to a size of 50 times of the observation area of the Auger experiment, which is until today the largest cosmic ray observatory. To detect EAS induced by UHECRs, fluorescence emissions of nitrogen molecules in the air and back-scattered Cherenkov light shall be detected.
In this chapter, the scientific goals and the baseline design of JEM-EUSO will be described. Furthermore, several pathfinder experiments including a test device for detecting cosmic rays with SiPM will be presented.

SCIENTIFIC GOALS

The scientific goals of the JEM-EUSO mission can be divided into one main objective and several exploratory objectives.
The main objective is to initiate an new field of astronomy using the extreme energy particle channel. JEM-EUSO will be the first cosmic-ray observatory, that explores cosmic rays with energies above 10^{19} eV with high statistics. Due to the high exposure of more than $10^5\ \mathrm{km}^2 \cdot \mathrm{sr} \cdot \mathrm{yr}$ a statistics of a hundreds of cosmic-ray events with energies above $7 \cdot 10^{19}$ eV during a three year operation is achievable [25]. Based on the increased statistics, four main scientific goals have been declared:

- Detection and high statistic measurements of UHECRs above $5 \cdot 10^{19}$ eV.
- Study of anisotropies in the cosmic ray arrival directions.
- Identification of cosmic ray sources and measurement of source energy spectra.

- High statistics measurement of the trans-GZK spectrum.

Beside of the main scientific goals there are several exploratory objectives in which JEM-EUSO can contribute [26]:

- Detection of extreme energy gamma rays
- Detection of extreme energy neutrinos
- Study of the galactic magnetic field
- Verification of the relativity and the quantum gravity effect
- Atmospheric science
- Detection of meteoroids and meteors
- Tracking of space debris

JEM-EUSO BASELINE DESIGN

In the baseline design, JEM-EUSO shall be connected to the Japanese Experimental Module (JEM) onboard the International Space Station ISS. The ISS orbits in a height of $380 - 430\,\mathrm{km}$ above ground with a speed of $7\,\mathrm{km/s}$.

JEM-EUSO is designed to detect fluorescence light of excited nitrogen molecules in the UV region emitted during an EAS. Also, the experiment is sensitive to Cherenkov light which is scattered in the atmosphere or reflected from clouds or the ground (see fig. 3.1).

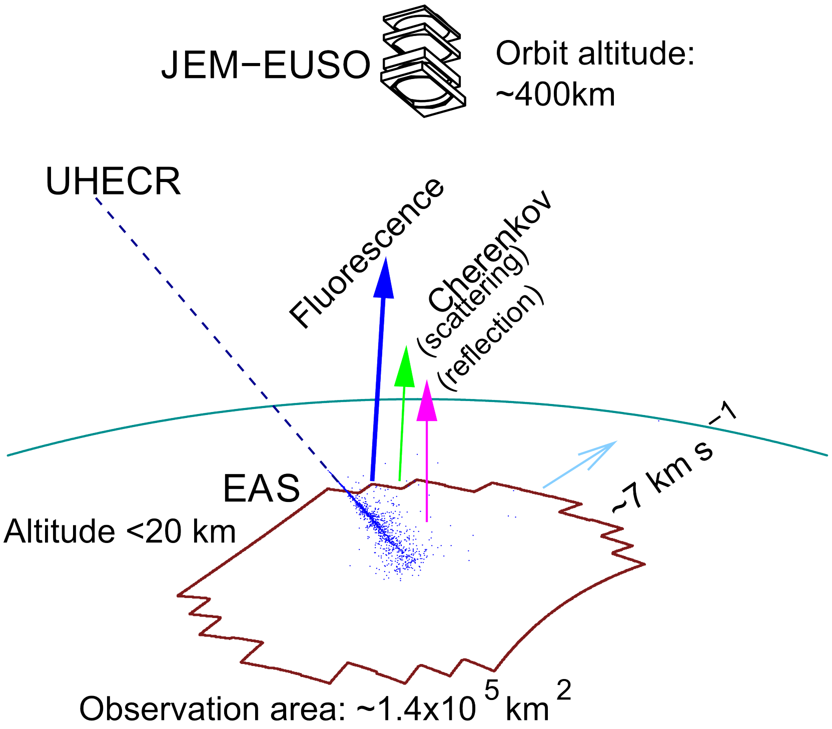

Figure 3.1: Sketch of the detection principle of JEM-EUSO [27].

By observing the shower development of the EAS in the atmosphere and measuring the amount of fluorescence and Cherenkov light generated during the EAS, conclusions about the primary cosmic-ray particle and the arrival direction can be made. The main part of the instrument is the telescope to detect fluorescence and Cherenkov light in the UV region which will be described in more detail. Beside of this, an observation system to monitor the area of the sky the telescope is pointed to and a calibration system to control the hardware parameters are part of the JEM-EUSO design.

JEM-EUSO telescope

The telescope of JEM-EUSO consists of a focussing optic, the focal surface for the detection of UV photons, and the electronics (fig. 3.2).

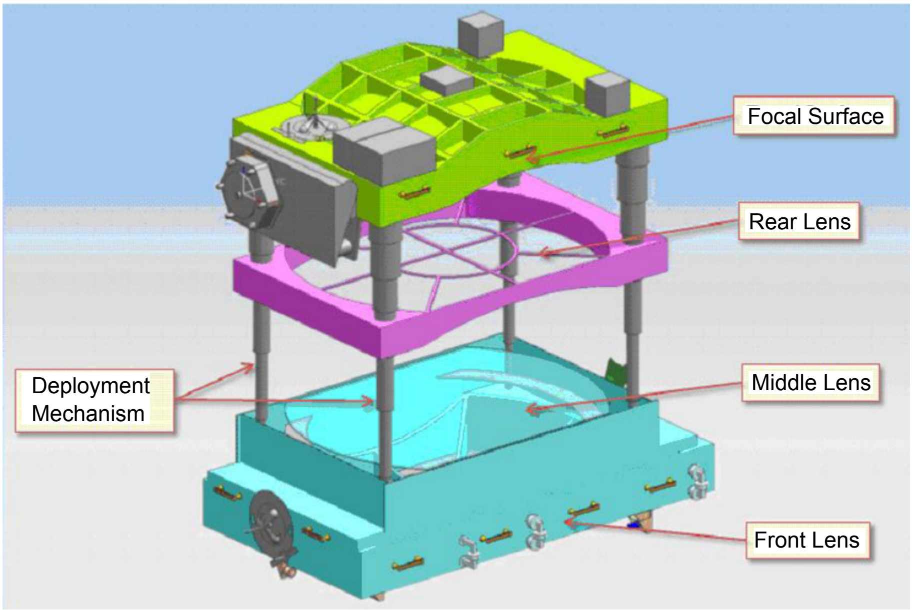

Figure 3.2: Illustration of the UV telescope of JEM-EUSO [28].

FOCUSSING OPTIC The focussing optic consists of two curved double sided Fresnel lenses at the front and at the rear side of the optics part and of a precision Fresnel lens to suppress the color aberration in the middle. Fresnel lenses are chosen since they are more lightweight and have lower volumes compared to conventional lenses. The front and rear Fresnel lenses have a diameter of $2.65\,\mathrm{m}$ and a thickness of $10\,\mathrm{mm}$. The lenses are made out of PMAA (polymethyl metacrylate, acrylic glass or "Plexiglas") which has a UV transmittance of $75-90\%$ for wavelengths between $300-400\,\mathrm{nm}$ [29]. The optics system achieves a full angle field of view of $60°$ and an angular resolution of $0.07°$ [28].

FOCAL SURFACE The focal surface has a diameter of $2.3\,\mathrm{m}$ and a $2.5\,\mathrm{m}$ curvature radius which gives a focal surface area of circa $4\,\mathrm{m}^2$. The focal surface area is covered with about 5000 Multi-Anode Photomultiplier Tubes (MAPMTs) with 64 pixels each. The single MAPMTs are grouped in cells of four MAPMTs which is called one Elementary Cell (EC) (fig. 3.3). One EC contains 256 pixels. Nine ECs are connected to a Photodetector Module (PDM, 2304 Pixel). The focal surface is made of 137 PDMs which gives a number of more than 300,000 pixels.

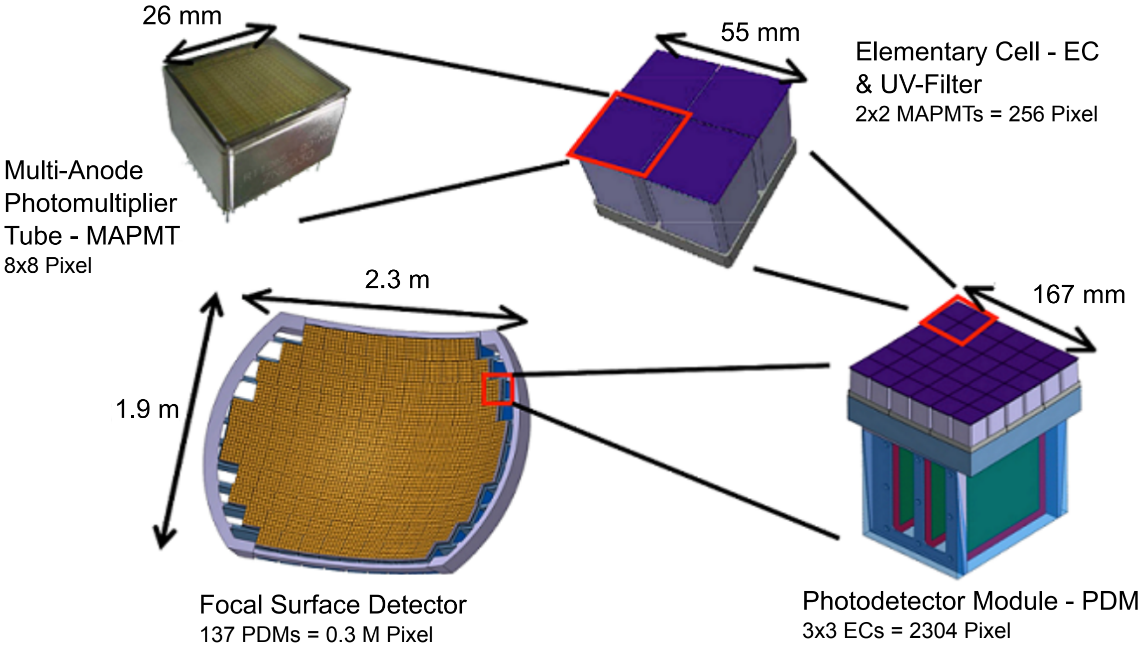

Figure 3.3: Composition of the focal surface of JEM-EUSO [9].

FOCAL SURFACE ELECTRONICS The focal surface electronic system records and processes the signals of UV photons generated by EAS. Requirements to the electronics are to keep up a high trigger efficiency with a flexible trigger algorithm as well as a reasonable linearity for the energy range of $10^{19} - 10^{21}$ eV. Also the electronic system has to have a very low power consumption in order to manage $3.2 \cdot 10^5$ signal channels and, since JEM-EUSO is operated outside the Earth's atmosphere, has to be intolerant to radiation in the space environment.
According to the three level structure of the focal surface (EC, PDM, FS), the electronic system is also build-up in three levels. In the first two electronic levels, the signals produced by the PMTs is read out at the anode of each PMT, digitized and recorded in ring memories during a Gate Time Unit (GTU) of 2.5 µs. In case of a trigger assertion, the stored data is read and send to control boards. In the last electronic level, Cluster Control Boards (CCBs) are used to perform further processing and a reduction of the data before the transmission from the ISS to the Earth.

PATHFINDER EXPERIMENTS

Several pathfinder experiments of JEM-EUSO have successfully been finished, are still in operation or are planed for the near future to test the detection principle of JEM-EUSO and to demonstrate the technical readiness level of the mission. Due to the topic of this master thesis, the focus will lie on the upcoming pathfinder experiment EUSO-

Super Pressure Balloon (EUSO-SPB) and the Silicon Elementary Cell Add-On (SiECA) testing the possibility to detect and measure EAS with Silicon Photomultiplier (SiPM).

euso-ta EUSO-TA is a ground based JEM-EUSO prototype located at the Telescope Array (TA) site in Utah, USA (fig. 3.4 right panel). The telescope of EUSO-TA consists of two square Fresnel lenses with a side length of $1\,\mathrm{m}$ which focus the light within a field of view of $\pm 4^\circ$ on the focal surface. The focal surface is made of one PDM (9 ECs, 36 MAPMTS, fig. 3.3) and has a detection area of $13.6\,\mathrm{x}\,13.6\,\mathrm{cm}^2$ [30].

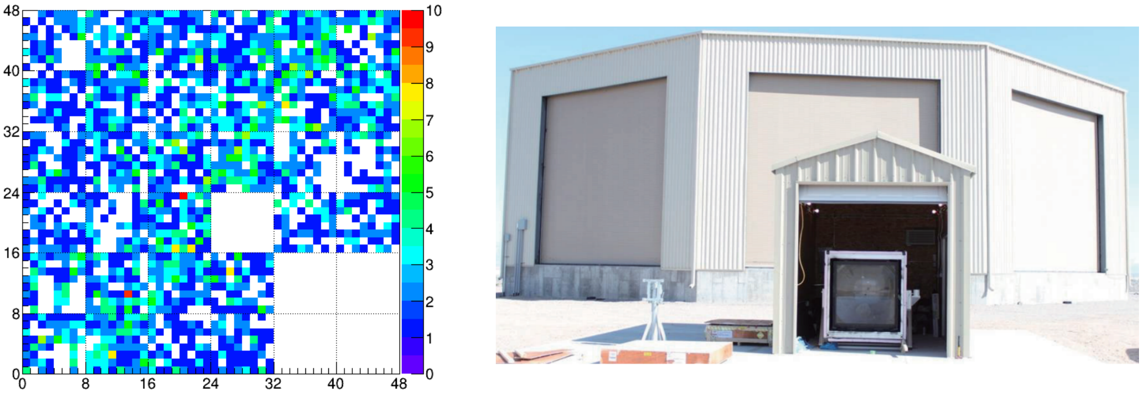

Figure 3.4: Left: Cosmic ray event observed with EUSO-TA. The event crosses the field of view from the top right side to the bottom left side. The energy of the primary particle was $10^{18}\,\mathrm{eV}$, the distance to the telescope was $2.5\,\mathrm{km}$ [31, 32]. **Right:** Picture of EUSO-TA located in front of a telescope station of TA [33].

At the TA site, an Electron Light Source (ELS) and a Central Laser Facility (CLF) are installed to artificially generate EAS. The aim of EUSO-TA is to calibrate the prototype PDM with these instruments and prove the readiness of the technique. In addition, EUSO-TA gets a trigger when the TA telescope detects an EAS and starts taking data. With this method, already three cosmic ray events with energies between $10^{18} - 10^{18.63}\,\mathrm{eV}$ have successfully been observed with EUSO-TA (see fig. 3.4 left panel) [31].

euso-balloon EUSO-Balloon is a successfully finished pathfinder experiment, testing the detection principle of JEM-EUSO in the atmosphere. Goals of the mission have been [34]:

- Full scale end-to-end test of all the key technologies and instrumentation of JEM-EUSO.
- Data acquisition and UV background studies.
- Detection of one or several EAS.

The optics of EUSO-Balloon consist of three[1] 8 mm thick, square Fresnel lenses with side lengths of 1 m (fig. 3.5). The field of view is ±6° which equals a surface on the ground of about 50 km^2. The focal surface is made of one PDM, similar to the PDM of EUSO-TA and the PDMs used for JEM-EUSO.

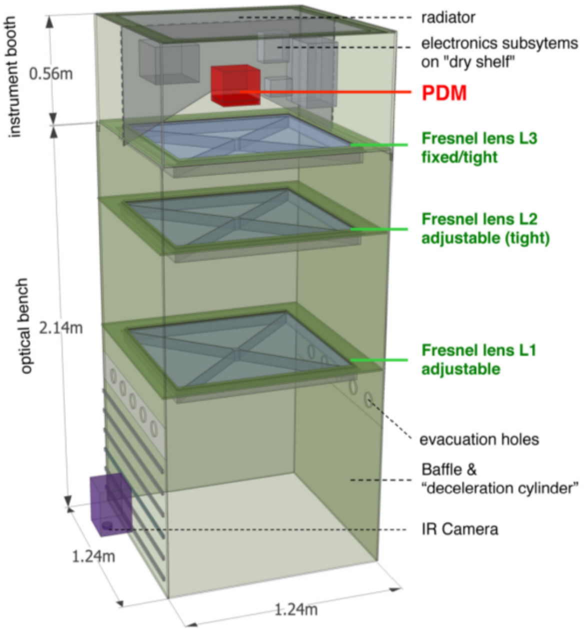

Figure 3.5: Schematic view of the composition of the EUSO-Balloon gondola [34].

EUSO-Balloon was launched on August 25, 2014, from Timmins Stratospheric Balloon Base in Ontario, Canada. The flight altitude was 38 km and the instrument operated during one entire astronomical night. During the flight, laser pulses and xenon flashes have been send by a helicopter into the field of view of EUSO-Balloon, simulating cosmic ray events.
The results of the EUSO-Balloon flight are presently being analysed.

EUSO-SPB EUSO-Super Pressure Balloon (EUSO-SPB) is an intended flight of a down-scaled JEM-EUSO detector setup with a Super Pressure Balloon (SPB) provided by the National Space Agency NASA in 2017. The aim of the mission is to make the first measurements of high-energy cosmic ray extensive air showers from near space and with this to provide an end-to-end test of JEM-EUSO.
NASA SPB flights start from Wanaka, New Zealand. The flightpath can not be controlled. After the start winds carry the balloon eastward approximately following 45°S

---

[1] The actual flight device of EUSO-Balloon had no middle lens to correct color aberration but was only equipped with the front and the rear lens [35].

latitude. An engineering flight of an SPB was performed in March 2015 by NASA to investigate the flight characteristics. The balloon travelled at an altitude of around 40 km for 32 days before its intended landing in Australia (see fig. 3.6).

Figure 3.6: The path of the 2015 NASA Super Pressure Balloon engineering flight of 32 days launched from Wanaka, New Zealand [35].

The instrumentation of EUSO-SPB will be similar to the instrumentation of EUSO-Balloon (fig. 3.5). Some upgrades compared to the EUSO-Balloon setup will be included which are listed in table 3.1.

Item	Description
MAPMTs	Upgrade to higher quantum efficiency multi-anode photomultiplier tubes
Solar power	Solar Panels and updated power system. Panels will be mounted on the 4 sides of the gondola for redundancy
Optics	Include a third fresnel lens that was in the original design to provide chromatic correction over the EAS UV spectrum
Power supply	Updated high voltage distribution system
Trigger	Upgraded trigger for EASs
Control	Update system control programming for a 50 day mission
Telemetry	Interface to the Columbia Scientific Balloon Facility's Support Instrument Package
Auxiliaries	SiECA, IR camera

Table 3.1: Upgrades for EUSO-SPB based on the EUSO-Balloon design [35].

Monte Carlo simulations were performed to estimate the detection rates of EAS during the EUSO-SPB flight. Within an energy range of $10^{17.75} - 10^{19.25}$ eV the simulation predicts detection rates between 0.09 and 0.42 events per hour of measurement time,

depending on the photon threshold of the trigger.
After a start in March 2017, EUSO-SPB will stay in the air for more then 18 nights with at least 2.5 hours dark time per night. This makes a total measurement time for EUSO-SPB of around 118 hours [35].

SIECA FOR EUSO-SPB

The Silicon Elementary Cell Add-On (SiECA) is a test device to investigate the possibility of using Silicon Photomultiplier (SiPM) as a replacement for the MAPMTs. SiPM have several advantages compared to MAPMTs, especially regarding an operation in a space-based experiment. SiPM do not need high voltage but can operate with bias voltages lower than 70 V like measurement in this thesis show. Also SiPM are more lightweight and robust, compared to PMTs. Disadvantages are the high dark count rate at room temperatures and a high temperature dependency of the SiPM characteristics which implies the need of a cooling mechanism for the SiPM or at least a thermal regulation of the bias voltage.

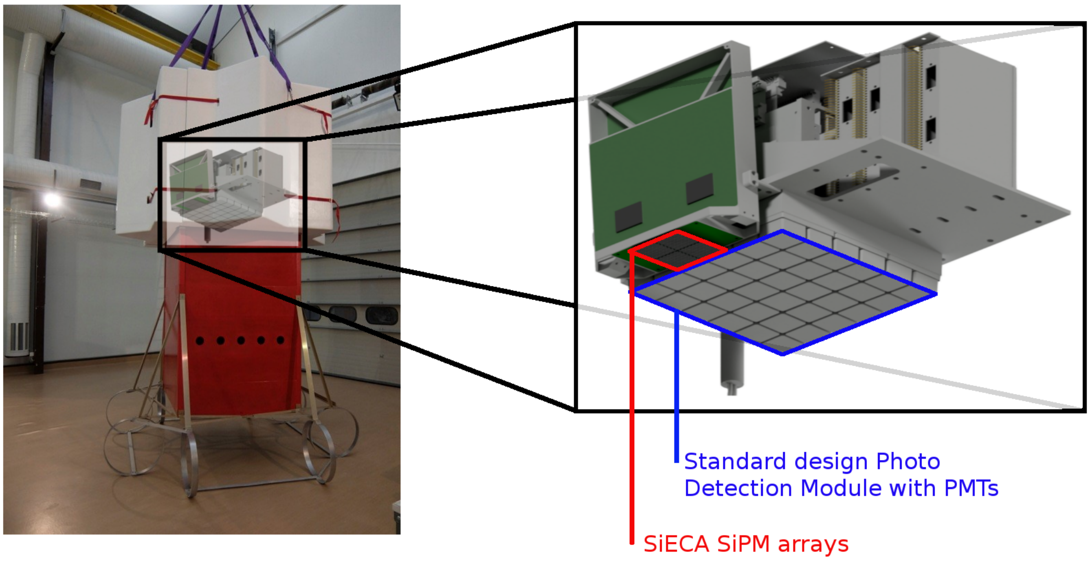

Figure 3.7: Illustration of the location of SiECA beside of the EUSO-SPB PDM which is located inside the gondola of the SPB. The gondola shown is from the EUSO-Balloon experiment. This picture is not to scale and does not represent the real construction.

SiECA is located beside of the PDM of EUSO-SPB and looks through the optical system to the ground (fig. 3.7).
SiECA is equipped with four 64 channel SiPM arrays covered with UV-transparent *Schott BG3* filter glass (fig. 3.8) which build an Elementary Cell (EC). Based on the characterization measurements made within this thesis, SiPM arrays of the type *S13361-*

3050AS-08 manufactured by Hamamatsu Corperation have been chosen. The read-out and signal processing electronics of SiECA are independent of the electronics of EUSO-SPB. The main experiment supplies SiECA with power and a 40 MHz clock signal via hard-wired connections. The EUSO-SPB electronics pass a trigger signal to SiECA when the EUSO-SPB PDM discovers an event. SiECA records the measured SiPM signals during the whole time of active operation and stores the data in a buffer of 1024 GTUs (GTU = Gate Time Unit = 2.4 μs). If a trigger is passed to SiECA, a signal sequence of 128 GTUs around the trigger event plus information about time, temperature of the device and other parameters are send back to the EUSO-SPB electronics via a USB connection between SiECA and EUSO-SPB. There they are stored together with the EUSO-SPB PDM data for the particular event and transmitted to the ground station.

The SiPM EC, consisting of the four 64 channel SiPM arrays, is located on the Si-EC board together with several capacitors and resistors to operate the SiPM in a correct way. The SiPM signals are passed to eight *Citiroc* ASIC read-out chips each with 32 input channels which are located on two independent boards. The uniformity of the focal surface consisting of 256 SiPM channels is guaranteed by slightly adjusting the individual bias voltage for each channel with the *Citiroc* ASICs [36]. The *Spartan 6* FPGA processes and stores the data from the ASICs and handles the communication with the EUSO-SPB main experiment.

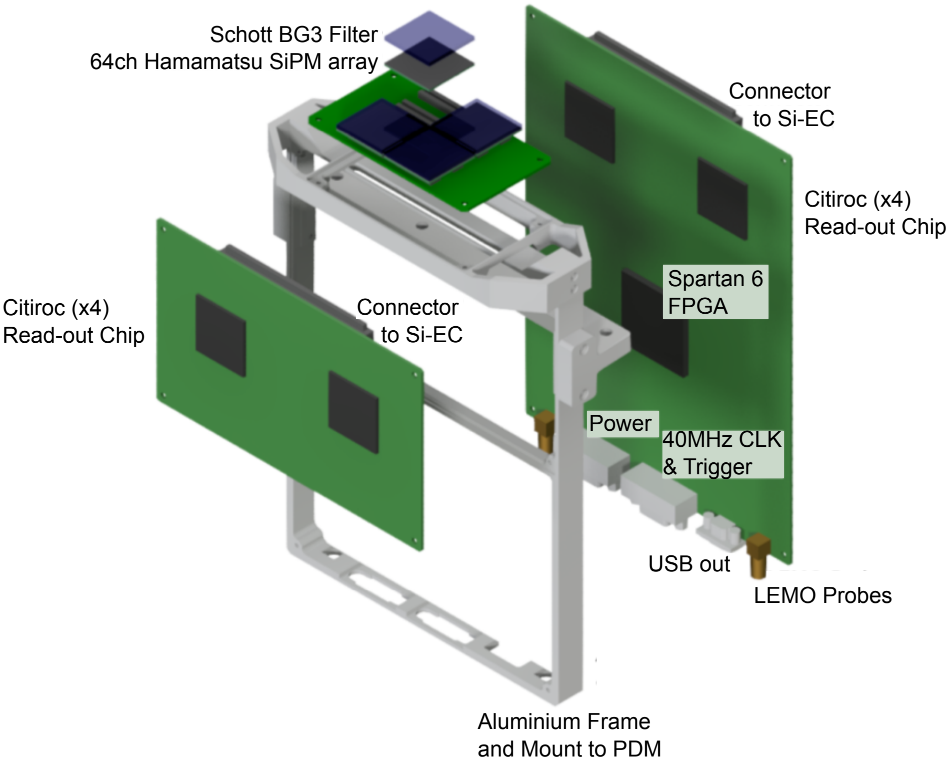

Figure 3.8: Schematic view of the composition of SiECA [37].

The bias voltage of the SiPM is generated by eight Hamamatsu SiPM power supplies *C11204-02* which can produce voltages between $50 - 90\,\text{V}$ and provide a maximal current of $2\,mA$ each [38]. The design of SiECA does not include a cooling system for the SiPM. The temperature dependency of the SiPM properties is handled by regulating the bias voltage of the SiPM in a way that the gain stays constant for all operating temperatures. A function of a temperature dependent bias voltage regulation is implemented in the SiPM power supplies.

Currently, SiECA is under development at the Institute for Nuclear Physics (IKP) at KIT and will be finished in August 2016.

4

SILICON PHOTOMULTIPLIER

Silicon Photomultiplier (SiPM) are a new type of photo detectors, capable of detecting single photons. Comparing to classical Photomultiplier Tubes (PMTs), SiPM have several advantages like a low operating voltage of below 70 V, an insensitivity to magnetic fields [39] and a robust and light construction [40]. Due to their semi-conductive nature, SiPM are highly temperature sensitive and have a temperature dependent high dark-count rate in the MHz region compared to PMTs with kHz noise rates.
In this chapter the working principle of SiPM will be explained and the techniques and methods used for characterising SiPM as used in the frame of this theses will be introduced.

SEMI-CONDUCTOR PHOTO DETECTORS

Silicon avalanche photo diodes

For the photon detection with a semi-conductive device, Silicon Avalanche Photo Diodes (S-APDs) are used. Silicon Photomultiplier consist of several hundreds to thousands of S-APDs connected in parallel. To understand the working principal of a SiPM, a closer look to S-APDs is needed.
An S-APD consists of a pn-junction operated in reverse mode and a quenching resistor. Figure 4.1 shows a schematic view of a pn-junction together with the strength of the electric field along the pn-junction and the photon flux depending on the depth of the pn-junction. The pn-junction of an S-APD is biased in reverse mode with a voltage V_{bias} a few volt above the breakdown voltage V_{break} of the diode. The difference of the breakdown voltage and the bias voltage is called over-voltage V_{ov}:

$$V_{ov} = V_{bias} - V_{break}. \tag{4.1}$$

All characteristics like gain, the photo detection efficiency and the dark-count rate are depending on the value of the over-voltage.
When a photon hits the S-APD surface (see fig. 4.1), it can penetrate into the layers of the S-APD. The penetration depth depends on the photon wavelength and the absorption coefficient of the S-APD material. A photon interacting with the p^+ or p layer of the pn-junction can excite an electron into the conduction band when the photon energy is at least as high as the band gap energy of the p^+ or p layer material. This can be seen as a production of an electron-hole pair. The electron-hole pair is separated before it can recombine again if it is produced in the p layer since the S-APD is biased

with a voltage which generates an electric field. Electron-hole pairs produced in the p^+ layer recombine since the electric field strength is not high enough to separate them before they recombine.
The produced electron move against the direction of the electric field towards the n-doped layer and is accelerated. When the energy of the accelerated electron becomes high enough it can produce more electrons via ionisation. In this way produced secondary electrons are also accelerated by the electric field and can produce further electrons via ionisation. An avalanche starts. Due to this avalanche like multiplication of the primary single electron in the avalanche region of the S-APDs pn-junction, an amplification of about a factor of 10^6 of the first photon-produced electron is reached.

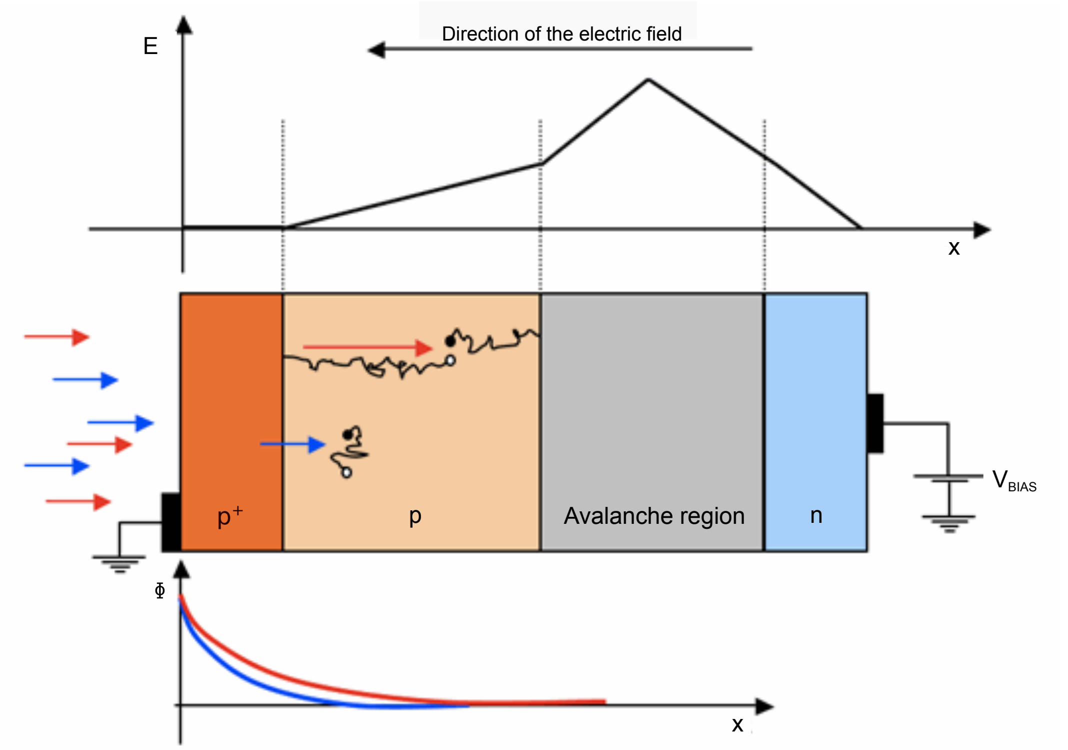

Figure 4.1: Schematic figure of a pn-junction like it is used in Silicon Avalanche Photo Diodes (S-APDs). The upper diagram shows the strength of the electric field through the pn-junction, the scheme in the middle shows the layers of the pn-junction with a sketch of incident photons producing electron-hole pairs. The diagram below shows the photon flux depending on the depth of the pn-junction [41].

In an S-APD the avalanche is stopped with a quenching resistor switched in series with the pn-junction which causes a voltage drop since a current is floating through the pn-junction. The electric field at the pn-junction decreases and produced secondary electrons are no longer accelerated to energies large enough for ionisation which stops the electron avalanche. During the quenching process of the electron avalanche, the

S-APD is not sensitive to incident photons. The maximum of the electron avalanche is reached about $1\,\mathrm{ns}$ after the photon enters the S-APD. The fall-time, in which the S-APD is not sensitive to incident photons, is tens of nanoseconds long [41]. The signal height produced by the electron avalanche is proportional to the over-voltage and the quenching resistor R_Q and follows V_{ov}/R_Q. The signal produced by an S-APD is of a binary nature giving information about whether a photon was detected or not. An information about the number of photons entering a single S-APD and generating the electron avalanche is not available.

The gain G of an S-APD can be defined as the number of electrons produced during the avalanche which started with one electron produced by an incident photon. If Q is the total amount of charge of the electrons generating the S-APD signal, this can be written as

$$G = \frac{Q}{e} \tag{4.2}$$

with the elementary charge e. The pn-junction can be seen as a capacitor with a capacity C storing a charge Q at a bias voltage higher then the breakdown voltage of

$$\begin{aligned} Q &= C \cdot (V_{bias} - V_{break}) && (4.3)\\ &= C \cdot V_{ov}. && (4.4) \end{aligned}$$

Since this charge Q is the charge set free during the avalanche process, the gain G is proportional to the over-voltage

$$G \sim V_{ov}. \tag{4.5}$$

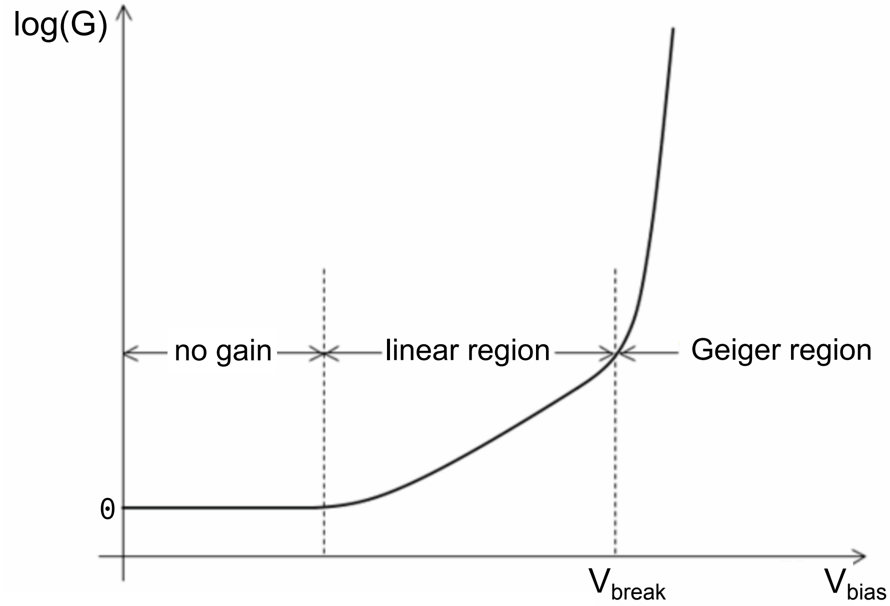

Figure 4.2: Schematic diagram of the gain vs. bias voltage behaviour of an S-APD [41].

Figure 4.2 shows the gain dependency regarding the bias voltage. For voltages below the breakdown voltage, the S-APD acts like a normal diode and amplifies no primary electrons. With increasing bias voltage the gain starts to rise linear. After the breakdown voltage, the gain increases very fast. The voltage region higher then the breakdown voltage is the Geiger region. S-APDs are biased with a voltage higher then the breakdown voltage and operate in the Geiger mode.

Silicon photomultiplier

One S-APD can give information whether there was a photon or not but is not sensitive to the number of incident photons at one time. To obtain information about that, multiple S-APDs are connected together in parallel which is called a Silicon Photomultiplier (SiPM) (see fig. 4.3).

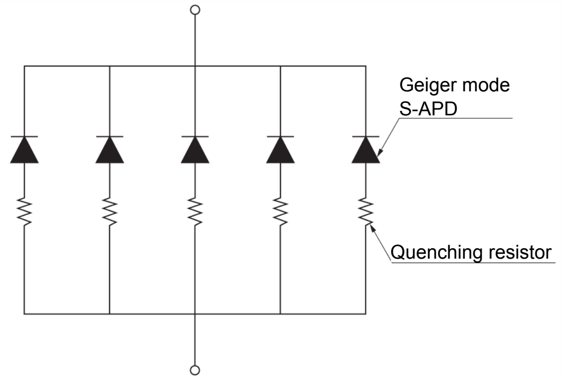

Figure 4.3: Sketch of a SiPM consisting of multiple S-APDs switched in parallel. The S-APDs consist of a pn-junction symbolized with a diode symbol and a quenching resistor. For detecting incident photons the S-APDs are biased in Geiger mode [42].

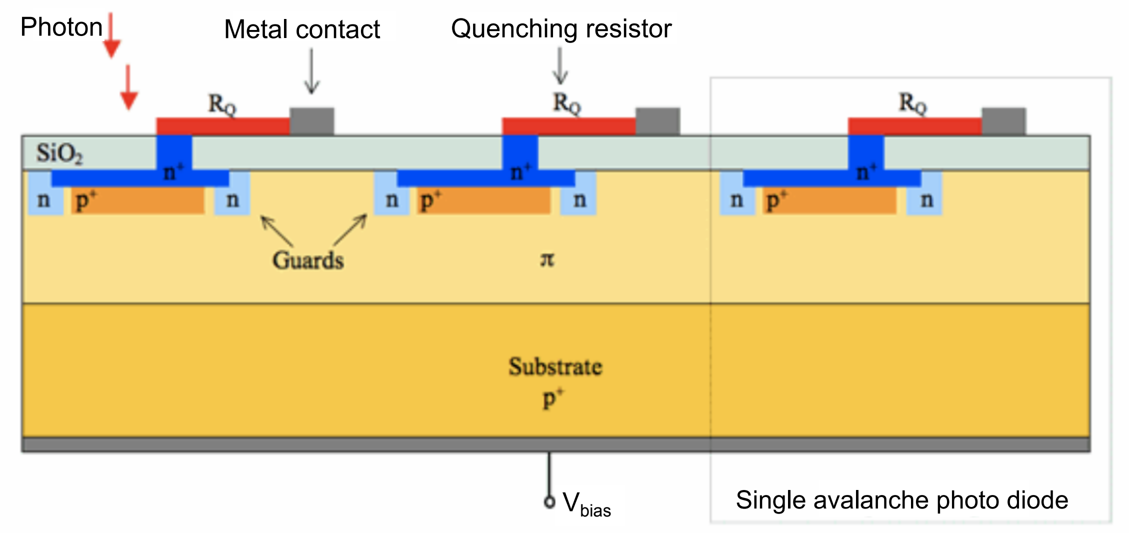

Figure 4.4: Cross section of a SiPM with three S-APDs [41].

Figure 4.4 shows schematically a cross section as an example of a SiPM structure. Three S-APDs are connected in parallel on one waver. Photons enter the SiPM through the anti-reflection SiO_2 coating and can produce an electron-hole pair in the circa 300 µm thick and p-doped π layer. Due to the high electric field in this region, the electron and the hole are separated. The hole moves to the lower, circa 3 µm thick p^+ layer where it recombines. The electron moves to the avalanche region in the area around the junction of the upper p^+ layer and the n^+ layer and initiates an electron avalanche. The width of the avalanche region depends on the bias voltage and is around 1 µm thick. The electrons generated in the avalanche are removed via the upper metal contact through the quenching resistor which stops the avalanche after about $1\,\mathrm{ns}$. The guard layers surrounding the p^+n^+-junction prevent primary electrons reaching the n^+ layer without moving through the avalanche region at the p^+n^+-junction.

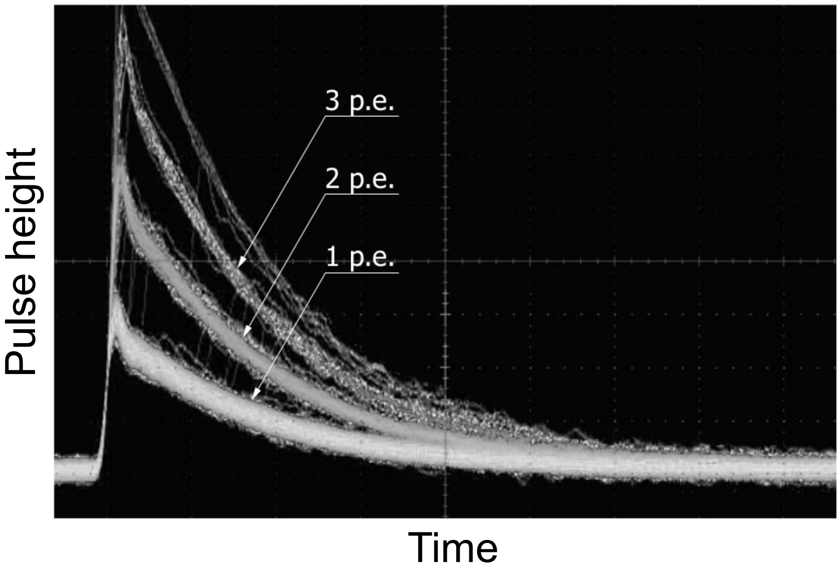

Figure 4.5: Example of SiPM signals generated by different numbers of firing S-APDs [42].

Due to the parallel wiring of many S-APDs, a SiPM device is sensitive to the number of firing S-APDs at the same time and so to the number of photons hitting the SiPM surface. The signal of all firing S-APDs is added, generating a quantized SiPM output signal of multiples of single S-APD signals (fig. 4.5). Since a photo electron is the generator of an electron avalanche in an S-APD and therefore the generator of a single S-APD signal, the height of the SiPM signal is counted in units of detected photo electrons (p.e.).

To increase the sensitive area, single SiPM are combined often to SiPM arrays. A single SiPM in the SiPM array is called channel, the S-APDs in the SiPM are called Pixel. During this thesis, SiPM arrays with 8 x 8 SiPM channels were tested.

NOISE EFFECTS

Due to their semi-conductive nature and the parallel wiring of many S-APDs in a small area, SiPM are highly noise afflicted. The three main phenomena producing noise effects are dark counts, crosstalk and afterpulsing.

DARK COUNTS In an S-APD electrons can not only be excited by incident photons but also by thermal effects. The thermal produced electrons can generate an electron avalanche and an S-APD signal not distinguishable from a signal produced by a photon excited electron. The noise signals produced in this way are called dark counts. The dark-count rate of a typical SiPM is in the MHz region and is one of the disadvantages compared to photomultiplier tubes which have a dark-count rate in the kHz range. Since dark counts are produced by thermal excitation, the dark-count rate of SiPM depends on the SiPM temperature and decreases fast with decreasing temperature.

AFTERPULSES A second noise effect owed by the semi-conductive nature of SiPM are afterpulses. Since the semi-conductor material owns not a perfect crystal lattice but contains impurities, electrons produced in an electron avalanche can be caught by trap states in the depletion zone. The trapped electrons are released time-delayed after the main avalanche was quenched by the quenching resistor. The released electrons can now produce a second avalanche and therefore a delayed second S-APD signal when they are released after the dead time of the S-APD. Since the probability of afterpulses rises with the amount of electrons in the avalanche, the afterpulse probability increases with an increase in over-voltage. Figure 4.6 shows afterpulse signals recorded directly after the main SiPM signals.

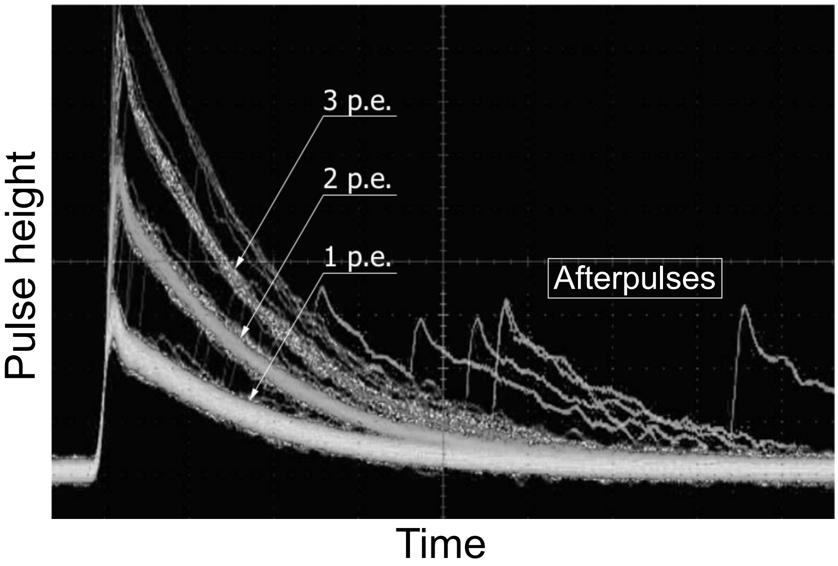

Figure 4.6: Example of afterpulse signals recorded with an oscilloscope [42].

CROSSTALK A third noise phenomena is the crosstalk caused by the small distances between S-APDs in a SiPM of around some hundred μm. During an electron avalanche in an S-APD, photons can be produced by electrons passing the pn-junction. These photons can enter and trigger a neighboured S-APD resulting in a 2 p.e. SiPM signal induced by only one incident photon. In a typical avalanche around 30 photons with an energy sufficient to produce another electron-hole pair are generated. The crosstalk probability depends on the distance to neighboured S-APDs (pitch). The greater the pitch-size, the lower is the crosstalk probability but the lower is also the effective photosensitive area of the SiPM. Since a crosstalk event happens at the same time at which the original photon induced signal is produced and is not distinguishable from that, each of the 2 or 3 p.e. signals in figure 4.5 could contain a fake S-APD signal produced by crosstalk.

TEMPERATURE CHARACTERISTICS OF SIPM

Since SiPM are semi-conductor devices, their characteristic values like breakdown voltage, gain and dark count are highly temperature dependent.
The temperature dependency of the breakdown voltage has its origin in the ionization rate $\alpha(E, T)$. Due to Brownian movement, carriers with higher temperature lose more energy by crystal lattice scattering. Therefore, the electric field strength has to increase with increasing temperature to obtain energies large enough for ionisation. Since the breakdown voltage is defined as the bias voltage at which carriers have enough energy to make ionisation and to start an electron avalanche, the breakdown voltage increases with increasing temperature. Operating the SiPM at a constant bias voltage, an increase in the breakdown voltage equals a decrease in the over-voltage, which affects all characteristic values of a SiPM. Figure 4.7 shows the temperature dependency of the gain and the bias voltage of a typical SiPM.

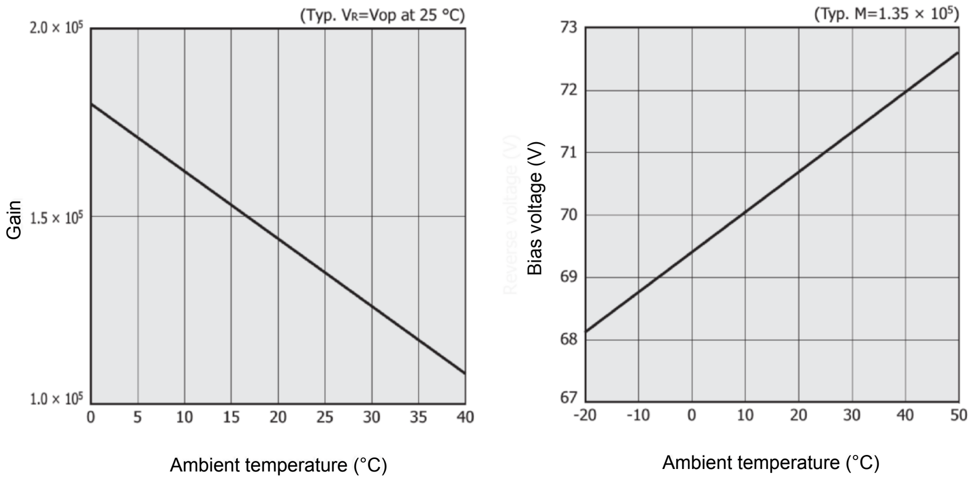

Figure 4.7: Left: Temperature dependency of the gain at a fixed bias voltage. The gain decreases since the over-voltage decreases with increasing temperature. **Right:** Temperature dependency of the bias voltage at a fixed gain of the SiPM [42].

According to G.A. Baraff [43], the ionization rate $\alpha(E, T)$ depends on three parameters:

$$\begin{aligned} \epsilon_i &: \text{ Ionization energy threshold} \\ \epsilon_r &: \text{ Optical phonon energy} \\ \lambda(T) &: \text{ Mean free path length of a carrier in the cristal lattice.} \end{aligned}$$

The ionization rate $\alpha_{(E)}$ can be expressed with two different models regarding the strength of the prevailing electric field [44].
For low electric field strengths carriers have to move through the crystal lattice without scattering to reach the ionization energy threshold ϵ_i. The ionization rate $\alpha(E, T)$ can be written as

$$\alpha(E, T) = \frac{q \cdot E}{\epsilon_r} \cdot e^{\frac{-\epsilon_i}{q \cdot \lambda(T) \cdot E}} \tag{4.6}$$

with the electric field strength E, the temperature T and the elementary charge q.
Is the electric field strength high, the energy which the carriers lose due to crystal lattice scattering is small compared to the energy obtained from the acceleration by the electric field. The ionization rate $\alpha(E, T)$ is in this case

$$\alpha(E, T) \approx exp\left(\frac{-3 \cdot \epsilon_r \cdot \epsilon_i}{(q \cdot \lambda(T) \cdot E)^2}\right). \tag{4.7}$$

Like it can be seen in figure 4.7 (right panel), the behaviour of the breakdown voltage regarding the temperature can be well described as a linear function when the SiPM is operated in a small temperature region of several ten degree Celsius. In this thesis, indeed a linear behaviour of the breakdown voltage regarding the temperature is assumed

$$V_{break} \sim T. \tag{4.8}$$

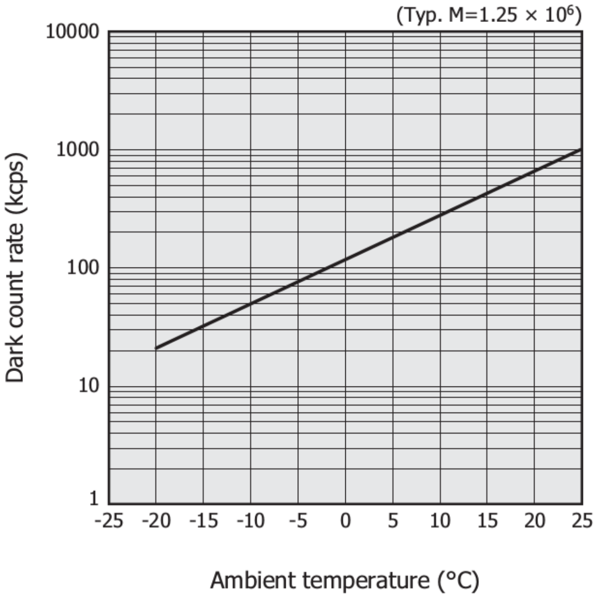

Figure 4.8: Temperature dependency of the dark-count rate regarding the temperature at a fixed gain [42].

Since the dark counts are induced by thermal excited electrons, the dark-count rate is also highly temperature dependent. The dark-count rate $\xi(T)$ can be written as [42]

$$\xi(T) = A \cdot T^{3/2} \cdot e^{\frac{E_g}{2 \cdot k_B \cdot T}} \tag{4.9}$$

with

A : Arbitrary constant
T : Temperature of the SiPM
E_g : Band gap energy
k_b : Boltzmann constant

Figure 4.8 shows the dark-count rate vs. the temperature for a SiPM with a photo sensitive area of 3 mm^2. The dark-count rate rises exponentially with the temperature.

TSV - SILICON PHOTOMULTIPLIER ARRAYS

For the goal of building a large focal surface out of SiPM, an important characteristic of the available SiPM arrays it the photo sensitive area. The best choice for a sensitive area as large as possible are Through Silicon Via (TSV) SiPM. In non-TSV SiPM the cathode of a SiPM is wired out at the SiPM surface. Building an array of SiPM, the cathode wiring has to be arranged around every SiPM channel on the SiPM array surface which increases the dead space. In TSV-SiPM the cathode is etched through the silicon waver in the middle of the SiPM, building an electrical interconnection from the surface to the bottom of the SiPM device. Since no wires have to be arranged around the SiPM channel of a SiPM array, the space between two SiPM channels in an array can be reduced from $\sim 3\,\mathrm{mm}$ to $\sim 0.2\,\mathrm{mm}$. Figure 4.9 shows the surface and the back side of a SiPM array which was studied within this thesis. On the surface the through silicon vias are visible as small white spots in the middle of each SiPM channel. On the back, the SiPM array is equipped with connectors made by Samtec[1] which are providing pins for the cathode and the anode of every SiPM channel of the array.

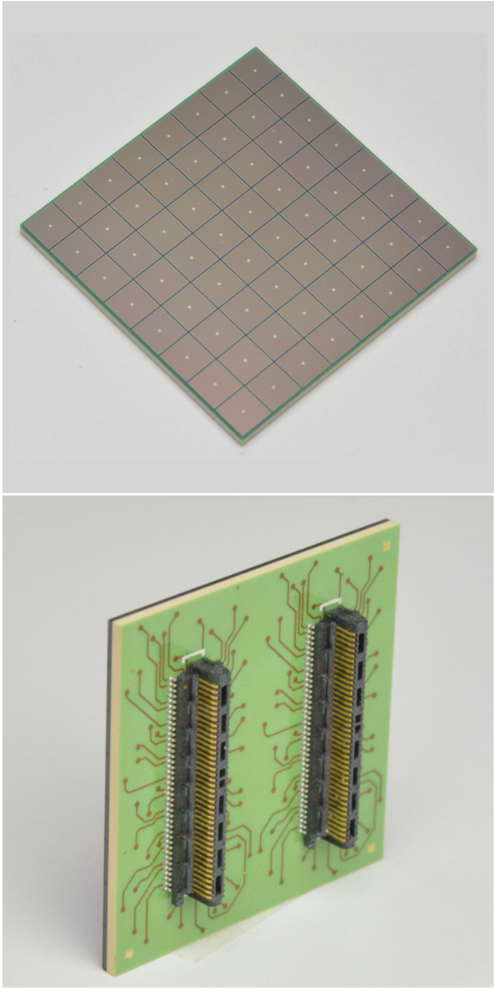

Figure 4.9: Pictures of the surface and the back side of a 64-channel Hamamatsu TSV-SiPM array S13361-3050NE [42]. The total size of the array is $3.2\,\mathrm{x}\,3.2\,\mathrm{cm}^2$.

---

[1] ST4-40-1.00-L-D-P-TR [45]

During this thesis, two different 64 channel TSV-SiPM arrays produced by Hamamatsu have been tested and characterized for the purpose of a use in SiECA and to investigate the advantages of the new SiPM array series. The tested SiPM arrays are *S12642-0808PA-50* (*S12*) and *S13361-3050AS-08* (*S13*). Both have a pitch-size of 50 µm. Further information about the SiPM arrays can be found in the appendix sections 9.2 and 9.3. Beside a predicted better performance of the new series SiPM array *S13* [46], an important difference between the two arrays is the resin of the SiPM surface. The old series SiPM array *S12* has an epoxy resin [47], the new series array *S13* has a silicone resin. The different resins result in a different sensitivity of the SiPM in light in the UV region lower then 400 nm. Figure 4.10 shows the wavelength sensitivities for a Hamamatsu SiPM S13361 and S12642 covered with silicone and epoxy resin. The fluorescence spectrum of nitrogen is plotted for comparisons with a dotted line.

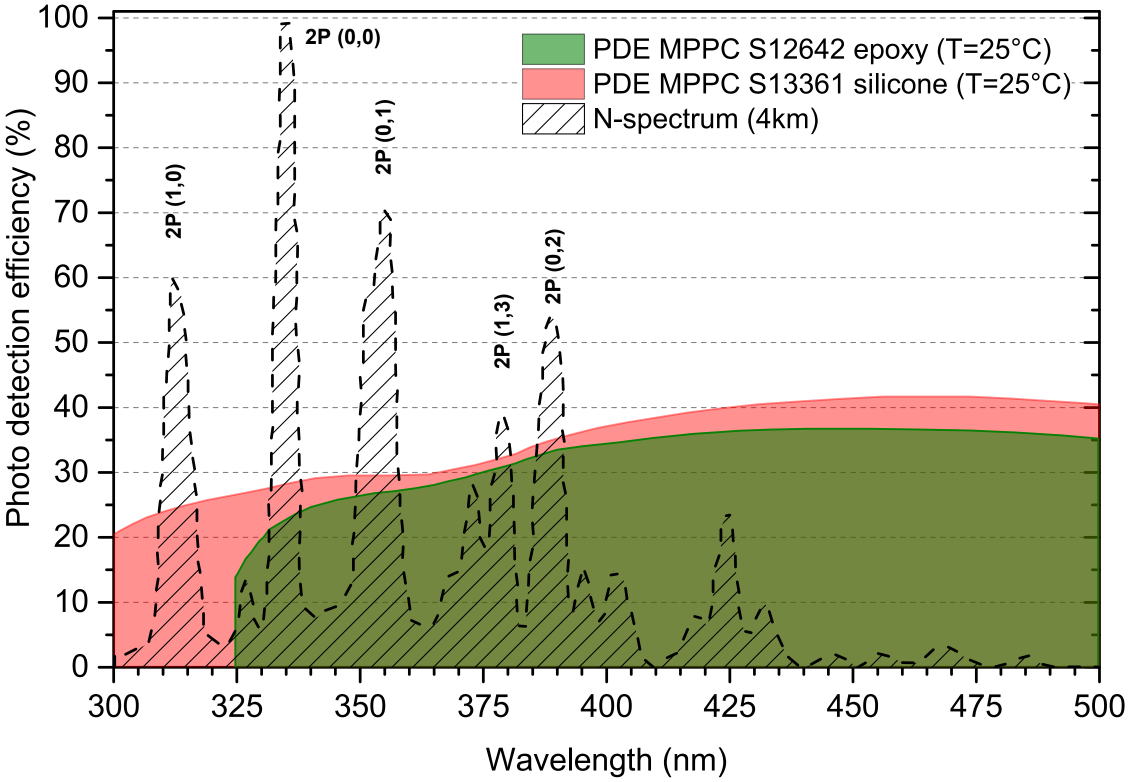

Figure 4.10: Figure of the wavelength sensitivity of a Hamamatsu 64 channel SiPM array S12642 with epoxy resin and a 64 channel SiPM array S13361 with silicone resin. The to the highest peak normalized fluorescence spectrum is shown with dotted lines for comparisons [48].

With an epoxy resin, the sensitivity for light in the UV region goes down to a wavelength of 320 nm while with a silicone resin light with a wavelength down to 270 nm can be detected. Especially for the purpose of measuring fluorescence and Cherencov light of extensive air showers in the UV region, this is an important advantage (see fig. 4.10). Due to the better performance (proved in this thesis, see section 7.4), the new series SiPM array *S13* has been chosen for SiECA.

CHARACTERISATION OF SIPMS

The important characteristics of a SiPM regarding an employment of the SiPM arrays in SiECA are the breakdown voltage, the gain, the Photo Detection Efficiency (PDE), the dark-count rate ξ and the crosstalk probability ϵ. For a better understanding of the SiPM and for the possibility of comparing the former and the actual series SiPM arrays[1] in more detail, information about the wavelength sensitivity in the UV light region and the dynamics of the SiPM response for small numbers of photons hitting the SiPM are of interest.

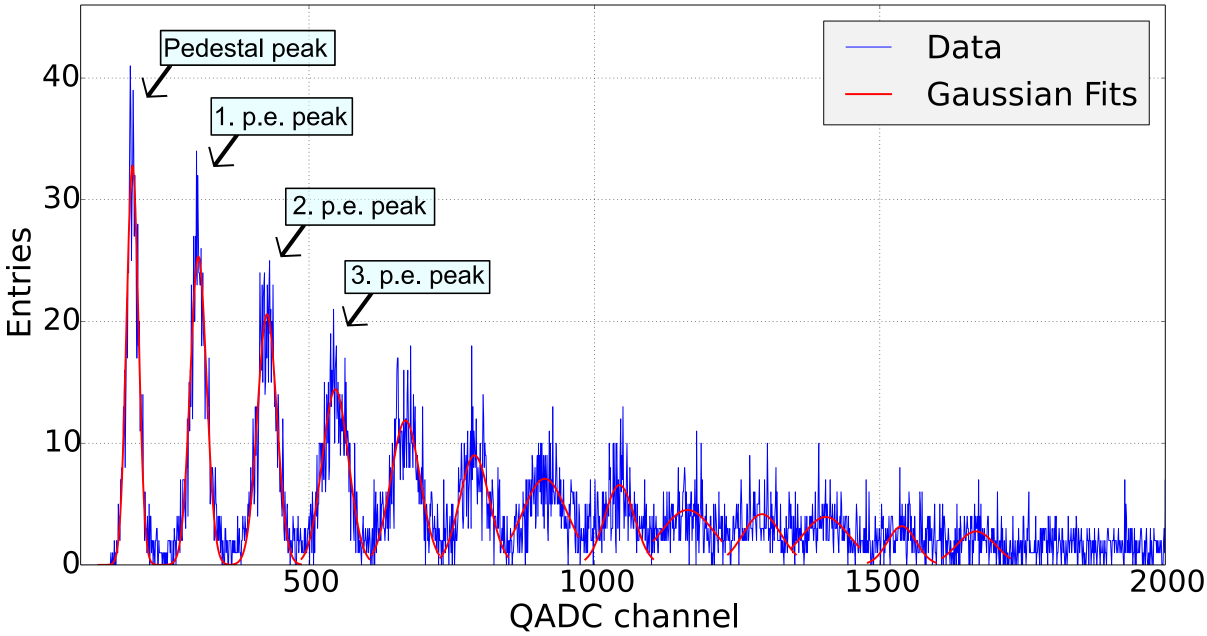

Figure 4.11: Example of a finger spectrum recorded with a single channel Hamamatsu SiPM *S12572-100C*. The finger spectrum contains around 10,000 QADC values. Together with the QADC data, Gaussian fits of the peaks are plotted with solid lines.

The key for obtaining all these information is the so called finger spectrum. In a characterisation measurement setup, the incident light is pulsed and the SiPM signals are feed into a Queued Analog-to-Digital Converter (QADC). The QADC integrates the

---

[1] The former 'old' series SiPM array *S12* was released in the year 2014, the actual 'new' series array was released in the year 2015 [46, 47]

SiPM signal and outputs the integrated signal charge in units of QADC channels. The time interval (gate) in which the QADC integrates the signal is coupled to the pulses of the LED. The QADC starts integrating when the LED starts to produce photons and ends when possible SiPM signals, induced by these photons, vanished. A more detailed description of the measurement setup and procedure is given in chapter 6. The individual integrated signals measured with the QADC are filled into a histogram containing several thousands of QADC data points. The in this way obtained histogram is called finger spectrum because of its characteristic peaks. Figure 4.11 shows an example of a finger spectrum recorded with a single channel Hamamatsu SiPM[1]. Since the SiPM response is quantized in multiples of p.e. signals, the integrated signal is also quantized in units of p.e. peaks. In the histogram different p.e. peaks are visible. The pedestal peak contains all the integrated SiPM signals in which no S-APD fired during the QADC gate. The other peaks contain the integrated SiPM signals which consist of one, two, three or more fired S-APDs. The most S-APDs fire because a photon hit the channel but the finger spectrum also contains dark count and crosstalk events which are not distinguishable from photon induced events.

Figure 4.11 shows Gaussian fits to the different peaks. For further calculation, the peak position x_{peak} and the number of events contributing to the particular peak A_{peak}, which is the area under the peak, are important. These information are obtained by using Gaussian fits of the form

$$f(x) = \frac{A_{peak}}{\sqrt{2 \cdot \pi} \cdot \sigma} \cdot e^{-2 \cdot \left(\frac{x - x_{peak}}{2 \cdot \sigma}\right)^2} \qquad (4.10)$$

with

x : QADC channel
$f(x)$: QADC channel entries
x_{peak} : Finger spectrum peak position
A_{peak} : Events in the Gaussian fit
σ : Standard deviation.

In the following, the methods which have been used during this thesis for obtaining the gain, the breakdown voltage, the PDE, the dark-count rate and the crosstalk probability of a SiPM will be presented. Also the procedure to get information about the response behaviour of an SiPM will be described.

---

[1] Single channel Hamamatsu SiPM *S12572-100C*

Gain

The gain can be derived directly from a recorded finger spectrum. Since the QADC channels represent the charge Q of the measured signal, the distance between consecutive finger spectrum peaks is the charge to which the first electron-hole pair was amplified to (see fig. 4.12).
The gain value $G_{channel}$ obtained with the finger spectrum is in units of QADC channels. To transform the gain in an amplification factor, a QADC-channel-specific transformation factor k is used. With this transformation factor, $G_{channel}$ is transformed into units of Coulomb. The transformation factors have been measured with their statistical and systematic uncertainties in [19, 49]. During this thesis, QADC channel zero was used. The transformation factor k for QADC channel zero is

$$k = (32.08 \pm 1.57_{stat} \pm 1.24_{sys})\,fC. \tag{4.11}$$

The real gain G is then derived according to equation 4.2 to

$$G = \frac{G_{channel} \cdot k}{A \cdot e} \tag{4.12}$$

with

G : Gain in real units
$G_{channel}$: Gain in units of QADC channels
k : QADC transformation factor
A : SiPM signal amplification
e : Elementary charge.

This equation takes into account, that the SiPM signal has to be amplified. The amplification of the SiPM signal leads to a horizontal stretching and makes a finger spectrum peak separation possible. Without amplifying, the peak distances would be to small to see single finger spectrum peaks any more since the resolution of the QADC is not high enough. During this thesis an amplification factor of 10 was used for every measurement.

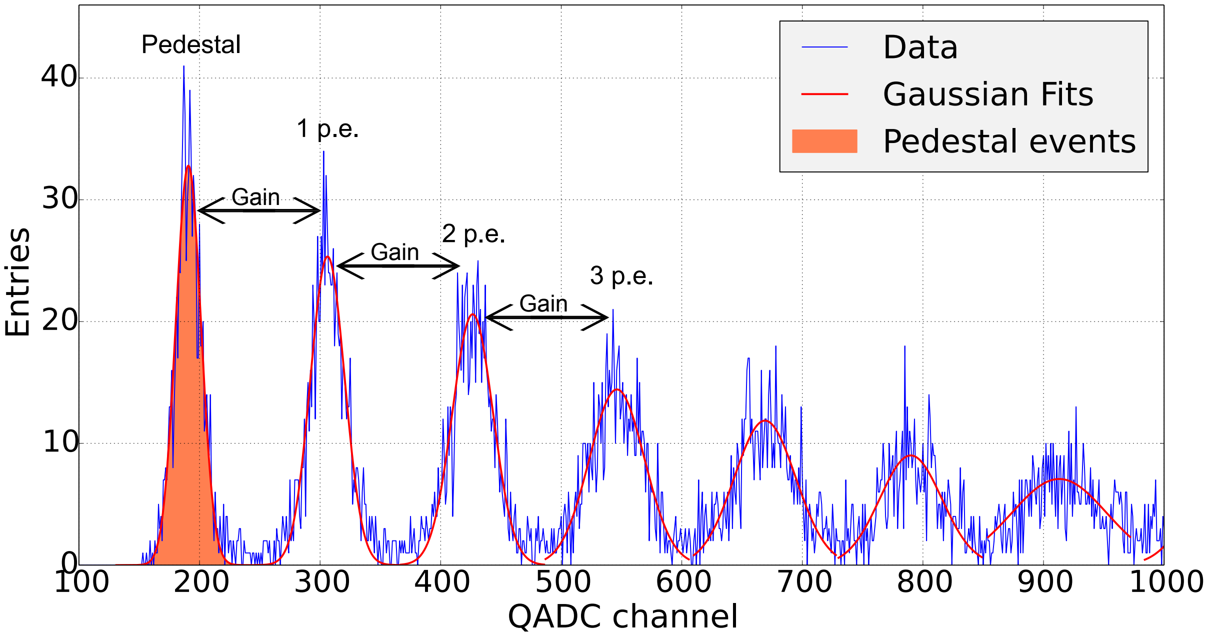

Figure 4.12: Figure of the characteristics of a finger spectrum regarding gain and PDE calculation. The finger spectrum is from a single channel Hamamatsu SiPM *S12572-100C* and is an enlarged version of figure 4.11.

STATISTICAL UNCERTAINTY The statistical uncertainty of the gain σ_G is calculated with the uncertainty of the gain in units of QADC channels $\sigma_{G_{\mathrm{channel}}}$ and the uncertainty of the transformation factor from QADC channel to charge σ_k:

$$\sigma_G^2 = \left(\frac{\partial G}{\partial G_{\mathrm{channel}}} \cdot \sigma_{G_{\mathrm{channel}}}\right)^2 + \left(\frac{\partial G}{\partial k} \cdot \sigma_k\right)^2 \tag{4.13}$$

$$= \left(\frac{k}{A \cdot e} \cdot \sigma_{G_{\mathrm{channel}}}\right)^2 + \left(\frac{G_{\mathrm{channel}}}{A \cdot e} \cdot \sigma_k\right)^2 . \tag{4.14}$$

The uncertainty of G_{channel} is the uncertainty of the peak positions obtained by the Gaussian fits of the finger spectrum peaks. This is evaluated automatically by the QADC peakfinding algorithm used for finding the finger spectrum peaks (see section 5.2). The statistical uncertainty of the transformation factor k is different for every of the 16 QADC channels. During the measurements of this thesis, only QADC channel zero was used which has a statistical uncertainty of $\sigma_k = 1.57\,\mathrm{fC}$ [19]. A statistical uncertainty in the elementary charge e is neglected. The amplification factor of the SiPM signal A has only a systematic uncertainty.

SYSTEMATIC UNCERTAINTY The systematic uncertainty of the gain Δ_G consists of the systematic uncertainty of the gain in units of QADC channels $\Delta_{G_{\mathrm{channel}}}$, the uncertainty of the transformation factor Δ_k and the systematic uncertainty of the signal amplification factor Δ_A:

$$\Delta_G^2 = \left(\frac{\partial G}{\partial G_{channel}} \cdot \Delta_{G_{channel}}\right)^2 + \left(\frac{\partial G}{\partial k} \cdot \Delta_k\right)^2 + \left(\frac{\partial G}{\partial k} \cdot \Delta_A\right)^2 \tag{4.15}$$

$$= \left(\frac{k}{A \cdot e} \cdot \sigma_{G_{channel}}\right)^2 + \left(\frac{G_{channel}}{A \cdot e} \cdot \sigma_k\right)^2 + \left(\frac{G_{channel} \cdot k}{A^2 \cdot e} \cdot \sigma_A\right)^2 . \tag{4.16}$$

The systematic uncertainty of the gain in units of QADC channels is made up of the systematic uncertainties of the finger spectrum peak positions and is $\Delta_{G_{channel}} = \sqrt{2} \cdot 0.1\% \cdot G_{channel}$ which results from the QADC non-linearity [19]. The systematic uncertainty of the transformation factor of QADC channel zero is $\Delta_k = 1.24\,fC$. The systematic uncertainty of the signal amplification is estimated to 3% which gives an uncertainty of $\Delta_A = 0.3$ for an amplification factor of 10.

Breakdown voltage

The breakdown voltage of a SiPM can be derived in two different ways. One method uses the voltage-current curve (U-I curve) to obtain information at which voltage the breakdown of the channel occurred. The breakdown voltage gained with this method is an overestimation of the real breakdown voltage and is seen as an approximation. A more precise result can be obtained by looking at gain values at different over-voltages. Both methods have been used during this thesis and are presented in the following.
A fast, but approximate result of the breakdown voltage can be derived by analysing the U-I curve of a SiPM. Since SiPM are diodes driven in reverse direction, the current through the diode should stay low for voltages below the breakdown voltage and should rise for voltages higher then the breakdown voltage. Figure 4.13 shows a measured U-I curve of a SiPM channel of a 64-channel Hamamatsu SiPM array[1].
Linear fits are made of the slopes of the U-I curve before and after the breakdown occurred. The region around 1.5 V around the starting inclination of the U-I curve is excluded in the fits. The approximate breakdown voltage is the crosspoint of the two linear fits. The resulting breakdown voltage is an overestimation of the real breakdown voltage since the crosspoint of the two linear fits is at higher voltages then the starting point of the slope (see fig. 4.13). Also the measured current though the SiPM is dependent of the light intensity which is emitted on to the SiPM. A lower light intensity will lead to a higher result of the breakdown voltage and therefore to a higher overestimation regarding the real value. Since this is an approximation made for preparing the exact breakdown voltage measurement, a precise error calculation is neglected here.

---

[1] 64 channel Hamamatsu SiPM array*S13361-3050AS-08*

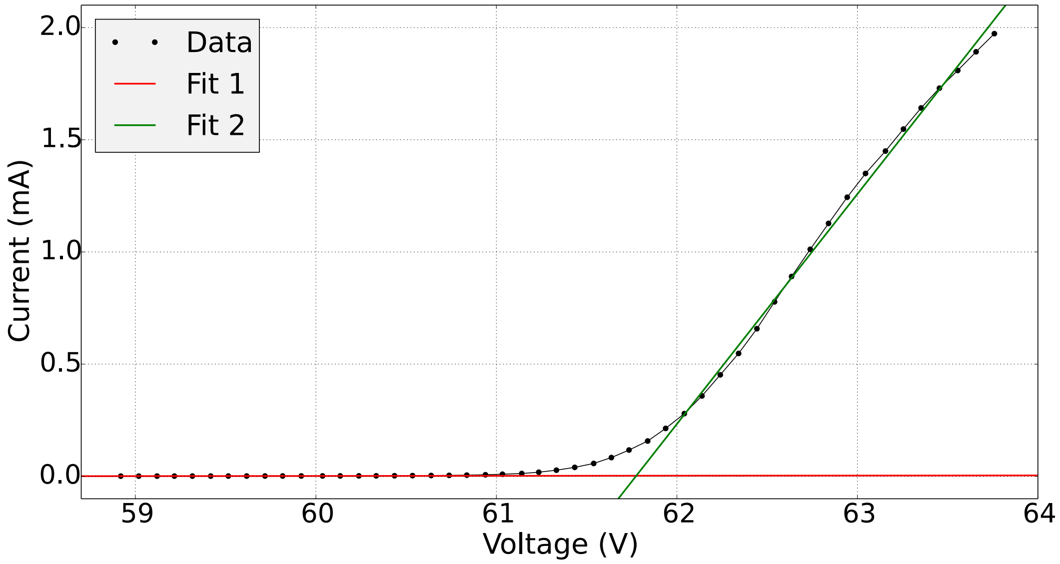

Figure 4.13: Example of a breakdown voltage measurement with the U-I curve of a SiPM.

A more precise result for the breakdown voltage can be derived by analysing the gain of the SiPM at different over-voltages. According to figure 4.2, the breakdown voltage is the voltage for which the SiPM starts to amplify excited electrons. The gain increases linearly with increasing over-voltage and becomes zero at the breakdown voltage point. The breakdown voltage can now be determined by measuring the gain at different bias voltages V higher then the breakdown voltage, making a linear fit $G(V)$ of the form

$$G(V) = a \cdot V + b \tag{4.17}$$

of the gain values and extrapolate the linear fit to a gain of zero. The voltage for which the gain becomes zero is the breakdown voltage of the SiPM (see fig. 4.14).

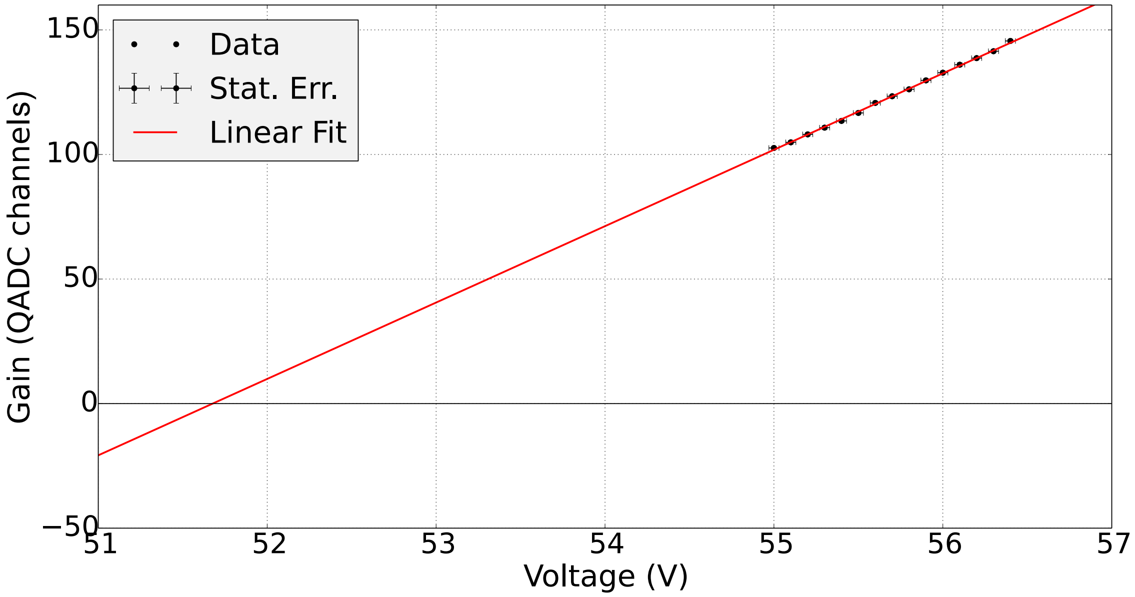

Figure 4.14: Example of the determination of the breakdown voltage by measuring the gain of the SiPM at different over-voltages and extrapolating the gain to the value at zero.

For the breakdown voltage determination, the gain can be kept in units of QADC channels. The breakdown voltage is the voltage for which equation 4.17 becomes zero:

$$V_{\mathrm{break}} = -\frac{b}{a}. \tag{4.18}$$

STATISTICAL UNCERTAINTY The statistical uncertainty of the breakdown voltage $\sigma_{V_{\mathrm{break}}}$ results from the statistical uncertainties of the linear fit of the recorded gain-voltage values. By using a linear fit $G(V)$ according to 4.17, the statistical uncertainty of the breakdown voltage is

$$\sigma^2_{V_{\mathrm{break}}} = \left(\frac{\partial G(V)}{\partial a} \cdot \sigma_a\right)^2 + \left(\frac{\partial G(V)}{\partial b} \cdot \sigma_b\right)^2 \tag{4.19}$$

$$= \left(\frac{b}{a^2} \cdot \sigma_a\right)^2 + \left(\frac{1}{a} \cdot \sigma_b\right)^2 . \tag{4.20}$$

The statistical uncertainties σ_a and σ_b are results of the linear fit $G(V)$.

SYSTEMATIC UNCERTAINTY The systematic uncertainty of the result for the breakdown voltage can be estimated in the following way. During the measurements made in this thesis, the bias voltage for the SiPM was generated with a set of two combined power supplies[1]. The systematic uncertainty of the bias voltage is assumed as 1% [50–

---

[1] SiPM array *S13361*: *TTi El302P* and *Tektronix PWS2326*, SiPM array *S12642*: *TTi El302P* and *Agilent E3612A*

52]. The gain vlaues are not transformed into real amplification factors. The systematic uncertainty of a measured gain value is 3%.
The systematic uncertainty of the breakdown voltage is assumed to be the sum of these two uncertainties and is estimated to 4%.

Photo Detection Efficiency (PDE)

The PDE is the probability that an incident photon is detected by the SiPM when it hits the SiPM surface. In general, the PDE is defined as

$$\mathrm{PDE} = \nu \cdot F_{geo} \cdot P_{avalanche} \tag{4.21}$$

where ν is the quantum efficiency which is the probability for an incident photon to produce an electron-hole pair, F_{geo} the geometric fill factor and $P_{avalanche}$ the probability of the produced electron-hole pair to generate an avalanche.
The PDE can also be written as the fraction of the number of detected photons per pulse N_{pe} and the number of incident photons per pulse N

$$\mathrm{PDE} = \frac{N_{pe}}{N}. \tag{4.22}$$

The number of incident photons depends on the optical power P emitted to the SiPM divided by the energy of one photon times the pulsed light frequency:

$$N = \frac{P \cdot R \cdot R_{geom}}{E_{photon} \cdot f_{pulse}} = \frac{P \cdot R \cdot R_{geom} \cdot \lambda}{h \cdot c \cdot f_{pulse}} \tag{4.23}$$

with

$$P : \text{Optical power measured with a photo diode} \tag{4.24}$$
$$R : \text{Collimator ratio} \tag{4.25}$$
$$R_{geom} : \text{Geometric correction factor} \tag{4.26}$$
$$h : \text{Planck constant} \tag{4.27}$$
$$c : \text{Speed of light} \tag{4.28}$$
$$\lambda : \text{Wavelength of the photons} \tag{4.29}$$
$$f_{pulse} : \text{Frequency of the pulsed light} \tag{4.30}$$

The geometric correction factor considers that the SiPM might be smaller then the cone of light coming from the integrating sphere. Since during all measurements a collimator was used with the collimator exit near the SiPM surface, it is assumed that every photon exiting the collimator hits the SiPM. The geometric correction factor is set to $R_{geom} = 1$.
The number of photons detected by the SiPM can be derived with Poisson statistics

from the number of events in the pedestal peak N_{ped} in spectra recorded with and without light (figure 4.12). For an ideal SiPM the finger spectrum has the form of a Poisson distribution with a mean value of the number of photons detected by the SiPM per pulse. Crosstalk, afterpulsing and dark-counts modulate this behaviour for peaks after the pedestal. The pedestal itself is not influenced by these noise effects. Since the number of dark-counts can be found with a dark spectrum, the finger spectrum pedestal can be corrected in respect to dark-counts and the mean value of detected photons per pulse N_{pe} can be determined.
The Poisson distribution follows equation

$$P(n, x) = \frac{n^x \cdot e^{-n}}{x!}. \tag{4.31}$$

In a SiPM spectrum n is the mean value of detected photons per pulse N_{pe} and x is the actual number of detected photons per pulse which equals the pedestal peak $(x = 0)$ and the p.e. peaks $(x = 1, 2, ..)$. Looking at the pedestal peak, equation 4.31 can be written as

$$P(n, 0) = e^{-n}. \tag{4.32}$$

The probability of a pedestal event $P(n, 0)$ can also be described by

$$P(n, 0) = \frac{N_{ped} \cdot R_{\xi}}{N_{tot}} \tag{4.33}$$

where N_{ped} is the number of pedestal events in the finger spectrum, N_{tot} is the total number of events and R_{ξ} is a correction factor regarding dark-count events.
The dark-count correction factor can be derived from a SiPM dark spectrum

$$R_{\xi} = \frac{N_{tot}^{dark}}{N_{ped}^{dark}} \tag{4.34}$$

since every event missing in the pedestal of a dark spectrum has to be a dark-count event. With this, the probability of a pedestal event $P(n, 0)$ can be written as

$$P(n, 0) = \frac{N_{ped}}{N_{tot}} \cdot \frac{N_{tot}^{dark}}{N_{ped}^{dark}} \tag{4.35}$$

only depending on the number of pedestal events in the light and dark measurement N_{ped} and N_{ped}^{dark} and the total number of events in the light and dark measurement N_{tot} and N_{tot}^{dark}.
Using equations 4.32, 4.35 and solving for the mean value of detected photons per pulse n results in

$$n = \ln\left(\frac{N_{ped}^{dark}}{N_{tot}^{dark}}\right) - \ln\left(\frac{N_{ped}}{N_{tot}}\right). \tag{4.36}$$

Since n equals the number of detected photons per pulse N_{pe}, the PDE can be calculated by using equations 4.23 and 4.36.

STATISTICAL UNCERTAINTY The statistical uncertainty of the photo detection efficiency σ_{PDE} consists of the statistical uncertainties of the number of incident photons σ_N and of the number of detected photons $\sigma_{N_{pe}}$:

$$\sigma_{PDE}^2 = \left(\frac{\partial PDE}{\partial N} \cdot \sigma_N\right)^2 + \left(\frac{\partial PDE}{\partial N_{pe}} \cdot \sigma_{N_{pe}}\right)^2 \tag{4.37}$$

$$= \left(\frac{N_{pe}}{N^2} \cdot \sigma_N\right)^2 + \left(\frac{1}{N} \cdot \sigma_{N_{pe}}\right)^2 . \tag{4.38}$$

To the statistical uncertainty of the number of incident photons σ_N contribute the uncertainties of the light intensity σ_I and of the collimator ratio σ_R

$$\sigma_N^2 = \left(\frac{R \cdot \lambda}{h \cdot c \cdot f} \cdot \sigma_I\right)^2 + \left(\frac{I \cdot \lambda}{h \cdot c \cdot f} \cdot \sigma_R\right)^2 . \tag{4.39}$$

The light intensity and its standard deviation are monitored and recorded during every measurement. The uncertainty of the collimator ratio comes from the calculation of the average collimator ratio over multiple measured collimator ratios.
The statistical uncertainty of the number of detected photons $\sigma_{N_{pe}}$ is made up of the uncertainties of the number of events in the pedestal peaks in the finger and the dark spectrum $\sigma_{N_{ped}}$ and $\sigma_{N_{ped}^{dark}}$.

$$\sigma_{N_{pe}}^2 = \left(\frac{1}{N_{ped}} \cdot \sigma_{N_{ped}}\right)^2 + \left(\frac{1}{N_{ped}^{dark}} \cdot \sigma_{N_{ped}^{dark}}\right)^2 . \tag{4.40}$$

The statistical uncertainties of the number of pedestal events with and without light are results of the Gaussian fits of the pedestal peak. The total number of measurements in the light and dark measurements N_{tot} is assumed to be constant with no uncertainties.

SYSTEMATIC UNCERTAINTY The systematic uncertainty of the photo detection efficiency Δ_{PDE} is made up of the systematic uncertainties of the number of incident and detected photons per pulse:

$$\Delta_{PDE} = \left(\frac{N_{pe}}{N^2} \cdot \Delta_N\right)^2 + \left(\frac{1}{N} \cdot \Delta_{N_{pe}}\right)^2 . \tag{4.41}$$

The systematic uncertainty of the number of incident photons Δ_N comes from the uncertainty of the optical power of the incident light Δ_P, the uncertainty of the average collimator ratio Δ_R, the uncertainty of the wavelength Δ_λ and the uncertainty of the pulsed light frequency Δ_f

$$\Delta_N = \left(\frac{R \cdot \lambda}{h \cdot c \cdot f} \cdot \Delta_P\right)^2 + \left(\frac{P \cdot \lambda}{h \cdot c \cdot f} \cdot \Delta_R\right)^2 \tag{4.42}$$

$$+ \left(\frac{P \cdot R}{h \cdot c \cdot f} \cdot \Delta_\lambda\right)^2 + \left(\frac{P \cdot R \cdot \lambda}{h \cdot c \cdot f^2} \cdot \Delta_f\right)^2 . \tag{4.43}$$

The systematic uncertainty of the optical power measured with a photo diode at an exit of the integrating sphere is $\Delta_P = 1.6\% \cdot P$. One collimator ratio measured with two photo diodes has the systematic uncertainty $\Delta_{R_{single}} = \sqrt{2} \cdot 1.6\% \cdot R_{single}$. In the further calculations of the PDE, an average collimator ratio of several single collimator ratio measurements is used. As an approximation, the systematic uncertainty of this average collimator ratio Δ_R is assumed as large as in the single collimator ratio measurement, so $\Delta_R = \sqrt{2} \cdot 1.6\% \cdot R$. The systematic uncertainty of the wavelength Δ_λ depends on the used LED and can be found in section 6.1 for each LED. The uncertainty of the pulsed light frequency results from the uncertainty of the frequency measurement with the oscilloscope *LeCroy WaveJet 324A* and is $\Delta_f = 10^{-5} \cdot f$ [19].
The systematic uncertainty of the number of detected photons $\Delta_{N_{pe}}$ is just made up of the systematic uncertainties of the number of events in the pedestal peak in the light and dark measurement $\Delta_{N_{ped}}$ and $\Delta_{N_{ped}^{dark}}$:

$$\Delta^2_{N_{pe}} = \left(\frac{1}{N_{ped}} \cdot \Delta_{N_{ped}} \right)^2 + \left(\frac{1}{N^{dark}_{ped}} \cdot \Delta_{N^{dark}_{ped}} \right)^2 . \tag{4.44}$$

The systematic uncertainty of the number of events in the pedestal peak has its origin in the QADC non-linearity and is for both cases with and without light assumed as $\Delta_N = \sqrt{2} \cdot 1.6\% \cdot N$.

Dark-count rate

The dark-count rate ξ can be investigated in two different ways. A first way is to record samples of the SiPM dark signal with an oscilloscope and count the number of dark-count events. To get the dark-count rate, the number of dark-count events $\#\xi$ has to be divided by the total measuring time of the oscilloscope t_{meas} which is recorded with the samples:

$$\xi = \frac{\#\xi}{t_{meas}} . \tag{4.45}$$

For counting the dark-count events, a SiPM peak finding algorithm written by Thomas Huber was used. A detailed description of the working principle of the algorithm can be found in [48]. The result for $\#\xi$ obtained with the peak finding algorithm depends on starting arguments describing the shape and height of the SiPM signal. The starting arguments are investigated by plotting several samples, counting the number of events manually and adjusting the starting arguments of the algorithm so that the number of events counted by the algorithm is identical to number of events counted manually. A clear investigation of the starting arguments was not always possible. A set of starting arguments might give good results for several samples but has deviations from the manually counted number of peaks in other samples. The result for the dark-count rate obtained with this method is seen as approximative.

Another way is to investigate the number of dark-count events with the dark spectrum of a SiPM combined with the knowledge of the gain. An ideal SiPM dark spectrum would consist only of the Gaussian distributed pedestal peak. Dark counts add events in the region of the first p.e. peak and because of crosstalk also in the region of the second p.e. peak to the spectrum. Per definition all events in the region of the first and second p.e. peak plus and minus half of the gain are assumed as dark-counts. Figure 4.15 shows this area in an example of a dark spectrum.

From the number of dark-count events the dark-count rate is calculated by dividing the number of dark-count events by the total measurement time

$$\xi = \frac{\#\xi}{N_{tot} \cdot (t_{gate} - 15\text{ns})} \tag{4.46}$$

where N_{tot} is the total number of events in the spectrum and t_{gate} is the gate length in which the QADC is working. Due to an activation time of 15 ns, the QADC starts measuring after the first flank of the gate with a delay which is subtracted from the gate time.

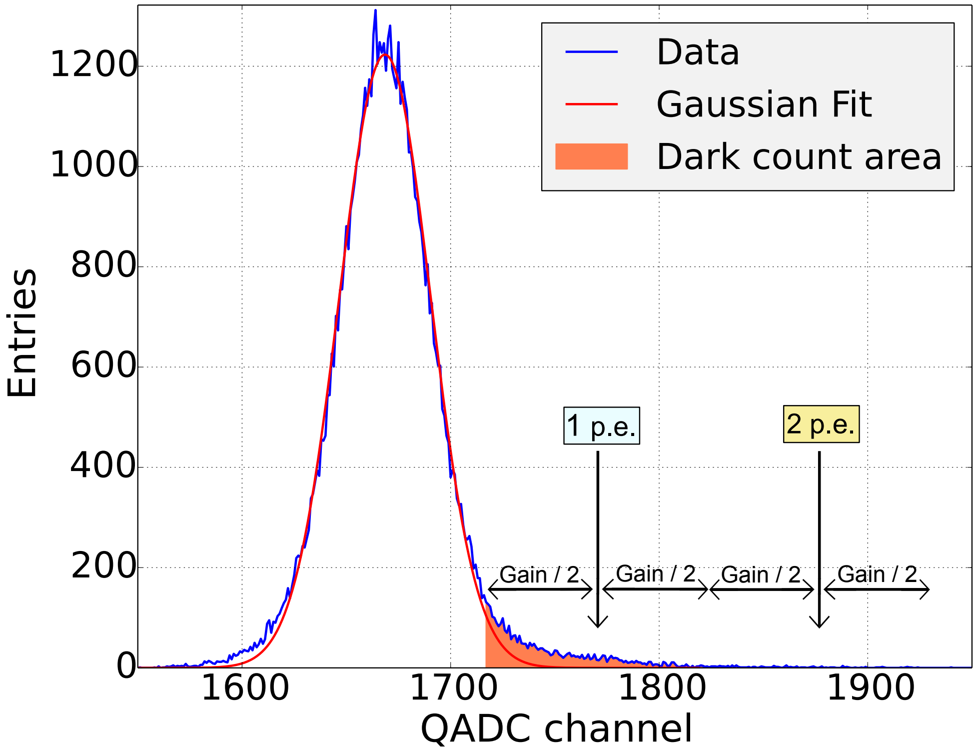

Figure 4.15: Example of the determination of the dark-count events in a SiPM dark spectrum. As definition, all events around the first and second p.e. peak plus and minus of half the gain are assumed as dark counts. The region is shaded in the figure.

STATISTICAL UNCERTAINTY The statistical uncertainty of the dark-count rate is obtained only by the number of events in the dark-count region $\sigma_{\#\xi}$.

$$\sigma_{\xi} = \frac{1}{N_{tot} \cdot (t_{gate} - 15ns)} \cdot \sigma_{\#\xi}. \tag{4.47}$$

The area in which all events are assumed as dark-counts depends on the position of the pedestal peak in the dark measurement and the gain obtained by analysing the finger spectrum. For estimating the statistical error in the numbers of dark-counts, the two worst cases which are the most minimal and most maximal result for the number of dark-counts are calculated. The larger deviation from the mean value of the minimal and maximal number of dark-counts is seen as statistical uncertainty. For obtaining the maximal number of dark-count events, the lowest possible pedestal peak position and the highest possible gain are used. For the most minimal number of dark-counts it is reversed.

SYSTEMATIC UNCERTAINTY The systematic uncertainty of the dark-count rate is made up of the systematic uncertainty of the number of dark-count events $\Delta_{\#\xi}$ and the systematic uncertainty of the gate length $\Delta_{t_{gate}}$

$$\Delta_{\xi}^2 = \left(\frac{1}{N_{tot} \cdot (t_{gate} - 15ns)} \cdot \Delta_{\#\xi} \right)^2 + \left(\frac{\#\xi}{N_{tot} \cdot (t_{gate} - 15ns)^2} \cdot \Delta_{t_{gate}} \right)^2 . \tag{4.48}$$

Due to the non-linearity of the QADC a systematic uncertainty of $\Delta_{\#\xi} = \sqrt{2} \cdot 0.1\% \cdot \#\xi$ is assumed. The gate length was in all measurements fixed to $73\,ns$. The statistical uncertainty of the gate length is estimated as $\Delta_{t_{gate}} = 3\,ns$ since the flanks of the gate signal have a finite inclination.

Crosstalk probability

During an electron avalanche in an S-APD, photons can be produced which have energies high enough to start a second electron avalanche in a neighboured S-APD [41]. The events induced by these photons are called crosstalk. The crosstalk probability ϵ of a SiPM can be determined by examine the dark spectrum. Every dark-count event can produce an additional crosstalk event. Instead of an one p.e. signal of the dark-count event, a two p.e. signal is recorded. The crosstalk probability is calculated as the probability with which a crosstalk event is produced by a dark-count event. The number of crosstalk events $\#\epsilon$ is the number of events around the second p.e. peak within a range of half of the gain (see fig. 4.16).
The number of dark-count events $\#\xi$ is calculated like it has been described in section 4.5. The crosstalk probability ϵ is

$$\epsilon = \frac{\#\epsilon}{\#\xi}. \tag{4.49}$$

STATISTICAL UNCERTAINTY The statistical uncertainty of the crosstalk probability σ_ϵ consists of the uncertainties in the number of crosstalk events $\sigma_{\#\epsilon}$ and in the number of dark-count events $\sigma_{\#\xi}$:

$$\sigma_\epsilon^2 = \frac{1}{\#\xi} \cdot \sigma_{\#\epsilon} + \frac{\#\epsilon}{\#\xi^2} \cdot \sigma_{\#\xi}. \tag{4.50}$$

The statistical uncertainties in the number of crosstalk and dark-count events are determined by searching the minimal and maximal numbers within the uncertainty range of the respective areas like it is described in section 4.5. The larger deviation from the mean value is seen as the statistical uncertainty.

SYSTEMATIC UNCERTAINTY The systematic uncertainty of the crosstalk probability $\Delta\epsilon$ consists of the systematic uncertainty in the number of dark-count events $\Delta_{\#\xi}$ and the systematic uncertainty in the number of crosstalk events $\Delta_{\#\epsilon}$:

$$\Delta_\epsilon^2 = \frac{1}{\#\xi} \cdot \Delta_{\#\epsilon} + \frac{\#\epsilon}{\#\xi^2} \cdot \Delta_{\#\xi}. \tag{4.51}$$

Due to the QADC non-linearity the systematic uncertainties in the number of dark-count and crosstalk events is $\Delta_{\#\xi} = \sqrt{2} \cdot 0.1\% \cdot \#\xi$ and $\Delta_{\#\epsilon} = \sqrt{2} \cdot 0.1\% \cdot \#\epsilon$.

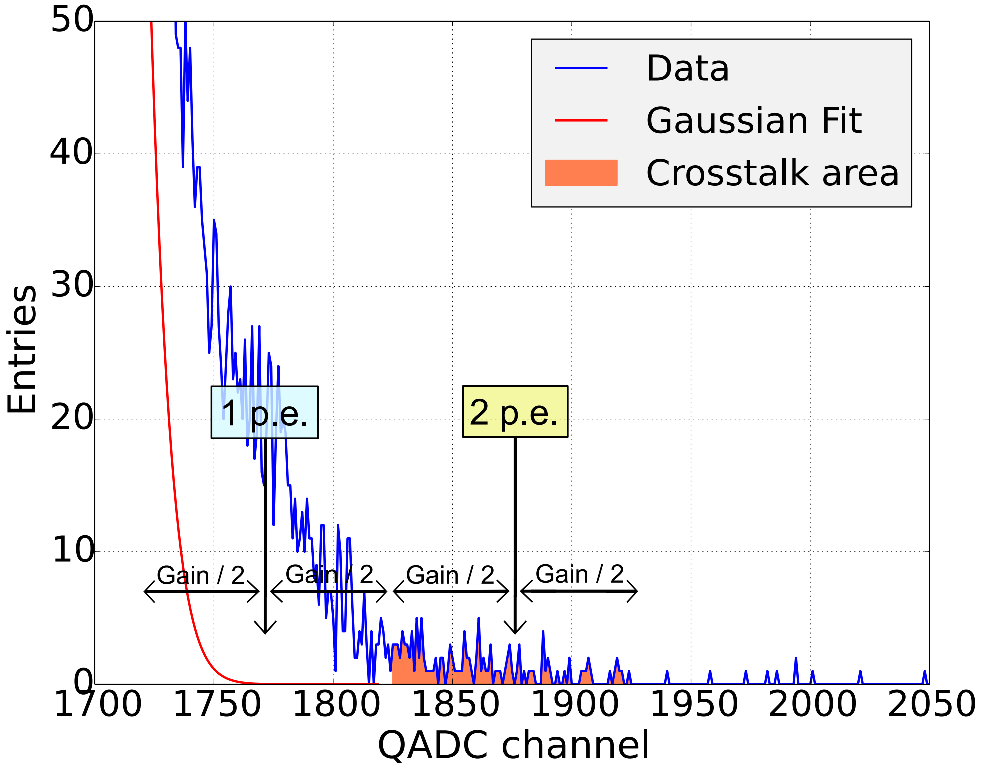

Figure 4.16: Example of the determination of the crosstalk events in a dark SiPM spectrum. All events around the second p.e. peak plus and minus of half the gain are assumed as crosstalk events. The corresponding region is shaded. The figure is an enlarged version of fig. 4.15.

Response behaviour

The response behaviour of a SiPM is investigated by measuring the number of firing S-APDs when a specific amount of photons hit the SiPM surface. For an ideal SiPM one APD would fire per one incident photon. But since the SiPM has no 100 % PDE, not every photon is detected by the SiPM and the fraction of firing S-APDs per incident photons decreases. Plotting the number of firing S-APDs over the number of incident photons, a linear behaviour is expected [42]. The linear behaviour of an ideal SiPM would have an inclination of 1, the real linear behaviour will therefore have a lower inclination.

The number of firing S-APDs is calculated with the median x_{med} of a finger spectrum. The median divides the measured QADC channels in two parts of equal numbers. To obtain the mean number of fired S-APDs, the median is divided by the gain $G_{channel}$ of the SiPM

$$\#\mathrm{APD}_{fired} = \frac{x_{med}}{G_{channel}}. \tag{4.52}$$

Since the median and the gain are both in units of QADC channels, a transformation into real charges is not necessary since the QADC has a sufficient linear behaviour. For obtaining information about the behaviour of the SiPM response, the firing S-APDs are plotted over the number of incident photons N which is calculated with equation 4.23.

STATISTICAL UNCERTAINTY The statistical uncertainty of the number of firing S-APDs $\sigma_{\#\mathrm{APD}_{\mathrm{firing}}}$ consists of the uncertainty of the median $\sigma_{x_{\mathrm{med}}}$ and the uncertainty of the gain in units of QADC channels $\sigma_{G_{\mathrm{channel}}}$

$$\begin{aligned}\sigma^2_{\#\mathrm{APD}_{\mathrm{firing}}} &= \left(\frac{\partial \#\mathrm{APD}_{\mathrm{firing}}}{\partial x_{\mathrm{med}}} \cdot \sigma_{x_{\mathrm{med}}}\right)^2 + \left(\frac{\partial \#\mathrm{APD}_{\mathrm{firing}}}{\partial G_{\mathrm{channel}}} \cdot \sigma_{G_{\mathrm{channel}}}\right)^2 \qquad (4.53)\\ &= \left(\frac{1}{G_{\mathrm{channel}}} \cdot \sigma_{x_{\mathrm{med}}}\right)^2 + \left(\frac{x_{\mathrm{med}}}{G^2_{\mathrm{channel}}} \cdot \sigma_{G_{\mathrm{channel}}}\right)^2 . \qquad (4.54)\end{aligned}$$

The position of the median depends on the position of the pedestal peak. An uncertainty of the calculation of the median is not assumed so the only statistical uncertainty is the uncertainty of the pedestal peak position which is a result of the Gaussian fit. Since the gain is kept in units of QADC channels, the statistical uncertainty is the uncertainty of the finger spectrum peak positions which is automatically calculated with the QADC peakfinding algorithm (see section 5.2).

SYSTEMATIC UNCERTAINTY The systematic uncertainty of the number of firing S-APDs $\Delta_{\#\mathrm{APD}_{\mathrm{firing}}}$ consists of the systematic uncertainties of the median $\Delta_{x_{\mathrm{med}}}$ and of the gain in units of QADC channels $\Delta_{G_{\mathrm{channel}}}$

$$\Delta^2_{\#\mathrm{APD}_{\mathrm{firing}}} = \left(\frac{1}{G_{\mathrm{channel}}} \cdot \Delta_{x_{\mathrm{med}}}\right)^2 + \left(\frac{x_{\mathrm{med}}}{G^2_{\mathrm{channel}}} \cdot \Delta_{G_{\mathrm{channel}}}\right)^2 . \qquad (4.55)$$

The calculation of the median is assumed to be precise so only the statistical uncertainty of the pedestal peak position coming from the QADC non-linearity contributes to the systematic uncertainty of the median which is then $\Delta_{x_{\mathrm{med}}} = 0.1\% \cdot x_{\mathrm{med}}$. The systematic uncertainty of the gain in QADC channels was already mentioned and is $\Delta_{G_{\mathrm{channel}}} = \sqrt{2} \cdot 0.1\% \cdot G_{\mathrm{channel}}$.

5

MEASUREMENT PREPARATION

For the purpose of the characterisation of SiPM arrays within the frame of this thesis, Printed Curuit Boards (PCBs) have been designed, measurement controlling software has been developed and a QADC peakfinding algorithm has been programmed. These measurement preparations will be presented in the following sections.

SIPM ARRAY READ-OUT BOARDS

To read out 64 channel SiPM arrays equipped with Samtec connectors, several printed circuit boards have been designed. The read-out circuits of all PCBs is in a general way shown in figure 5.1 [53].

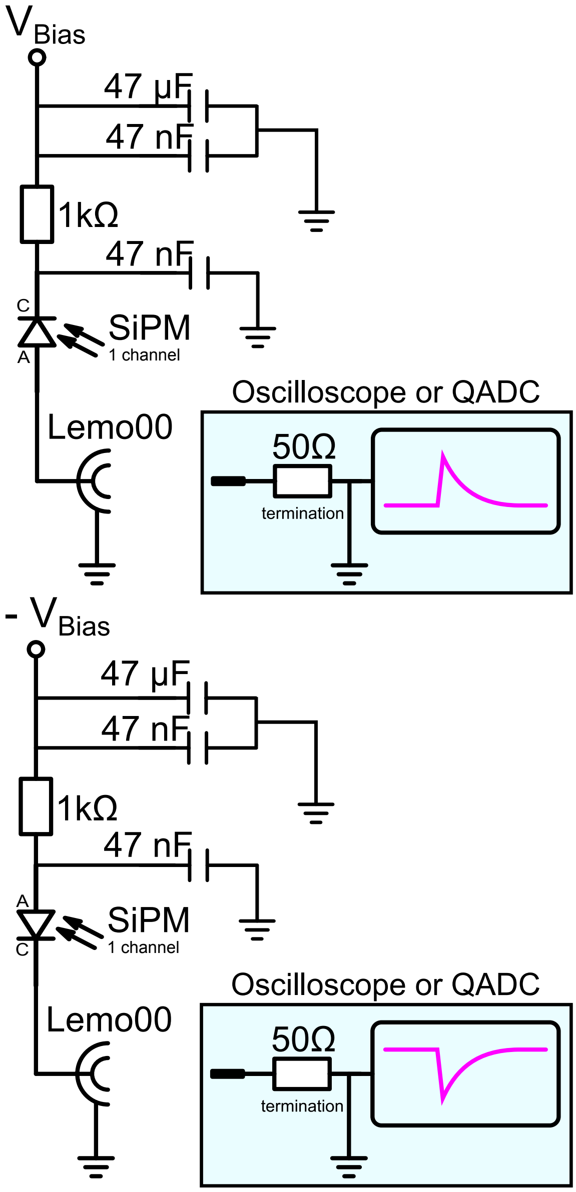

Figure 5.1: General read-out circuit for one SiPM channel. **Left:** Read-out circuit for positive signals with a positive bias voltage. **Right:** Read-out circuit for negative signals with a negative bias voltage [53].

The bias voltage is passed through a 1 kΩ resistor to the SiPM. The signal is guided out to a Lemo connection from which it can be fed into an oscilloscope or an Data Acquisition System (DAQ)[1]. Before of the 1 kΩ resistor, two capacitors with 47 nF and 47 µF flatten the incoming bias voltage. The 47 nF capacitor between the resistor and

---

[1] During this thesis, a Queued Analog-to-Digital Converter (QADC) was used.

the SiPM causes a fast voltage drop after the SiPM has fired and is directly influencing the signal length of the SiPM. Positive and negative signals can be produced by biasing the SiPM with positive or negative voltage respectively. Switching the bias voltage polarity, the wiring of the SiPM has to be modified like it is shown in figure 5.1. Boards with a negative bias voltage and a negative output signal were made since the used QADC can only process negative signals. Due to time reasons, the measurement within this thesis were made with a first version read-out board outputting positive SiPM signals which has been inverted before it was passed to the QADC (see sec. 6.2).

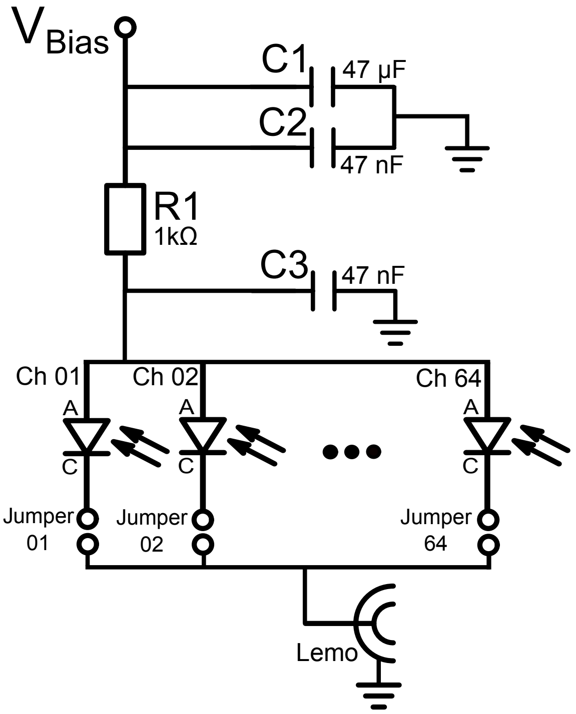

Figure 5.2: Sketch of the electronic circuit of the SiPM read-out board version 1.

One challenge during the design of a 64 channel SiPM read-out board is to find a way to select the signal from one defined channel which is then fed into the DAQ since every channel has to be characterized individually. Also, every signal has to be amplified before it can be processed by the QADC, which gives further complications, especially regarding the goal to automate the characterizing process for all the 64 channels. The selection of one out of the 64 SiPM channels and the amplification of the signal was handled in different ways within three versions of read-out boards designed in the frame of this thesis. The three versions of the SiPM array read-out board will be presented in the following.

Beside of the presented solutions of read-out and amplify the SiPM signals, Application-Specific Integrated Circuits (ASICs) can be used to handle this task. An ASIC made for SiPM array read-out purposes is the *Citiroc* ASIC manufactured by *Weeroc*. *Citiroc* ASICs are for example successfully used in the 'Astrofisica con Specchi a Tecnologia Replicante Italiana' (ASTRI) telescope experiment which is a prototype of the proposed Chrenkov Telescope Array (CTA) [54]. Also the SiECA SiPM read-out is based on *Citiroc* ASICs. *Citiroc*s have 32 SiPM input channels. Every channel is amplified by adjustable low gain and high gain amplifiers simultaneously. A signal-to-charge conversation is integrated in the ASIC with an adjustable time interval for signal integration [55]. These functionalities make the ASIC a considerable alternative to the presented read-out solutions in this thesis. However, due to the high ASIC costs and the limited time of this thesis, a characterising setup based on ASICs was not taken into account.

SiPM array read-out board version 1

In a first version of a 64 channel SiPM array read-out board the selection of one defined channel was solved with mechanical jumpers which connect the SiPM exit and the Lemo entrance of always only one channel at each time.

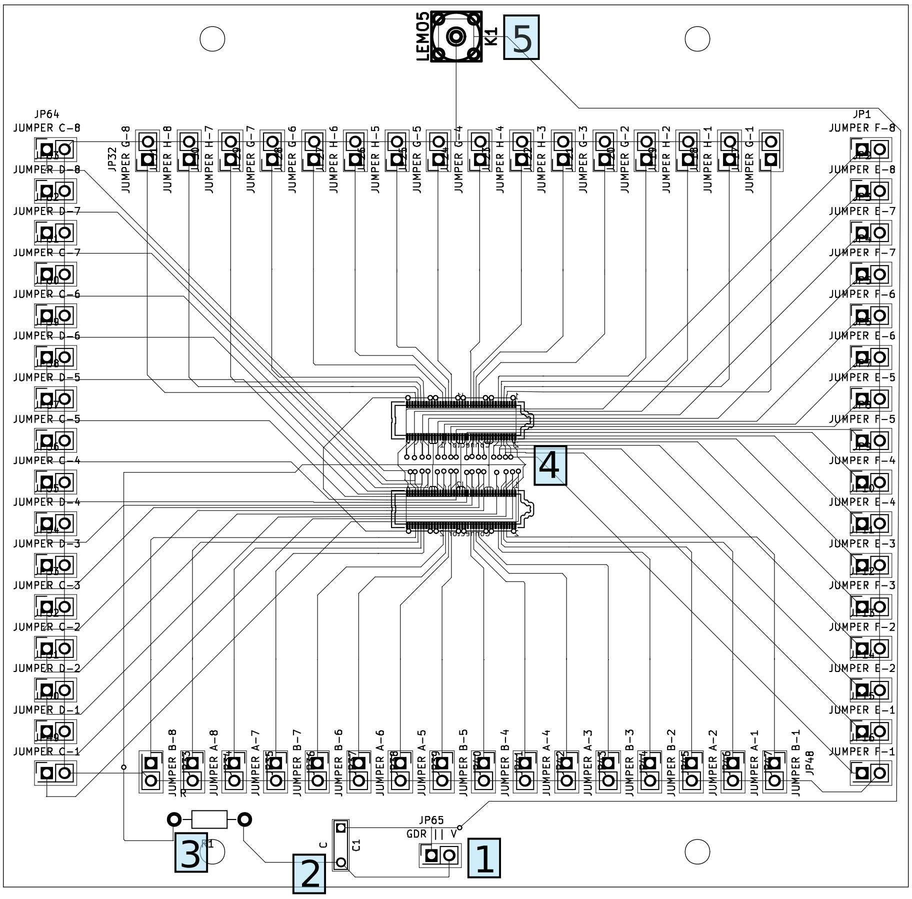

Figure 5.3: Scheme of the SiPM array read-out board version 1. **1:** Pins for V_{bias} and ground. **2:** 47 µF and 47 nF capacitors. **3:** 1 kΩ resistor. **4:** Samtec sockets. **5:** Lemo connection for signal out.

Figures 5.2, 5.3 and 5.4 show the electronic circuit of the SiPM read-out board ver. 1. For every channel of the SiPM array, the circuit can be closed between the Samtec socket and the Lemo entrance by setting a jumper (figure 5.2). In this way the wanted channel can be chosen.

As seen in figure 5.3, the jumpers are placed around the two Samtec sockets (**4**) in which the SiPM array is plugged in. The jumpers are named after the channel to which they belong. The bias voltage and the ground come in via two pins (**1**). At position **2** the 47 µF (C1) and 47 nF (C2) capacitors are placed. The 1 kΩ (R1) resistor is at position **3**. The 47 nF (C3) capacitor in the SiPM signal path was soldered by hand to the board and is not shown in the scheme.

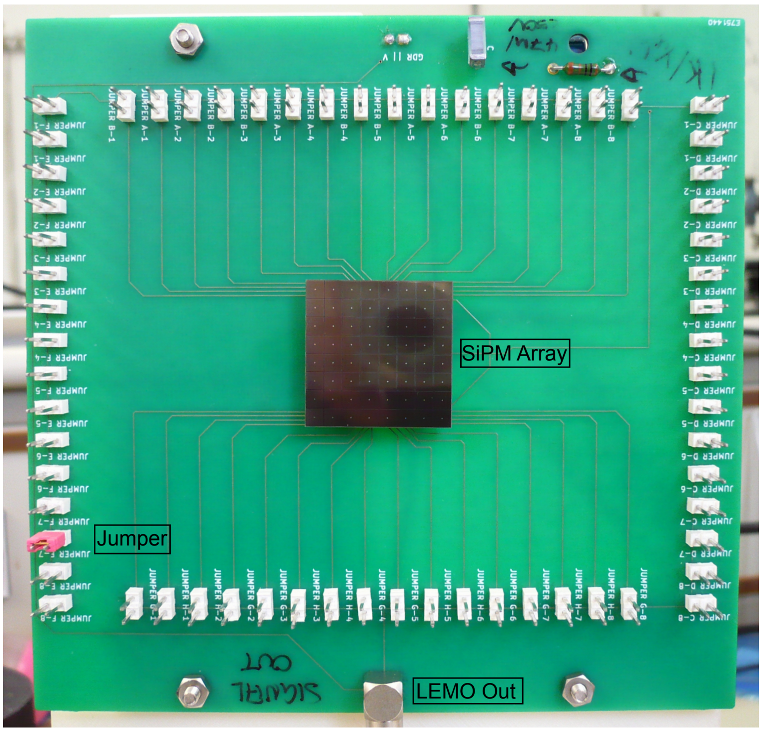

Figure 5.4: Picture of the front of the SiPM read-out board version 1 equipped with a 64 channel SiPM array.

This first version of the SiPM read-out board consists of two copper layers. The board is designed for positive bias voltages and positive output signals. Since there is only one resistor R1 and only one capacitor C3 for all channels of the SiPM array, only one single channel can be read out at each time. The amplification of the signal is not implemented on the board but has to be made externally. Due to time reasons, this first version board was used for the measurements within this thesis. For more information about the used amplification device and the signal processing it is referred to section 6.2. Figure 5.4 shows a photo of the manufactured read-out board equipped with a SiPM array.

SiPM array read-out board version 2

In the next version of the SiPM read-out board, the selection of a specific SiPM array channel is realized by using the multiplexer system already available at the Single Photon Calibration Stand at Kit (SPOCK, section 6.1). The signal lines of all 64 SiPM channels are connected to a 2 x 32 pin header on the board from which the signals of each channel goes via Lemo connection to two Multiplexer. The Multiplexer reduce the 64 incoming channels to 16 which are passed to the 16-channel QADC. A sketch of the electronic circuit of the PCB is shown in figure 5.5.

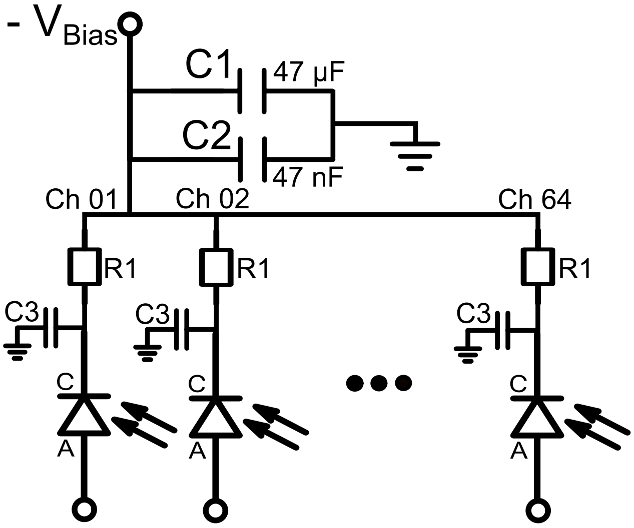

Figure 5.5: Sketch of the electronic circuit of the SiPM read-out board version 2. The capacitors C3 have a capacitance of 47 nF. The resistors R1 have a resistance of 1 kΩ.

Due to the board design, every SiPM channel needs a 1 kΩ resistor R1 and a 47 nF capacitor C3[1]. Electronic parts with a SMD soldering surface have been chosen for the R1 resistors and C3 capacitors. The board is designed to operate with a negative bias voltage and to output negative signals since the QADC only processes negative signals. A positive version can be designed easily on the basis of this board. To reduce noise coupling into the board wires, the board consists of four layers. The top layer on which the Samtec connector sockets are placed and the bottom layer which contains the SMD resistors and capacitors are filled with a grounded copper area everywhere it is possible. The voltage supply and signal wires are guided in the two layers between the bottom and the top layer.

Figure 5.6 shows a schematic view of the SiPM read-out board version 2. The two Samtec sockets are located on the top layer of the board (**6**), the SMD resistors and capacitors R1 and C3 are placed on the bottom layer of the board (**2** and **1**). The capacities C1 and C2 (**3** and **5**), which flatten the incoming bias voltage, stay as pinhole devices. The bias voltage and the ground are connected via two pins at position **4**.

---

[1] Based on the experience of the work in this thesis, currently a Bachelor thesis is ongoing to optimize the resistors and capacitors for the use of Hamamatsu SiPM [56]

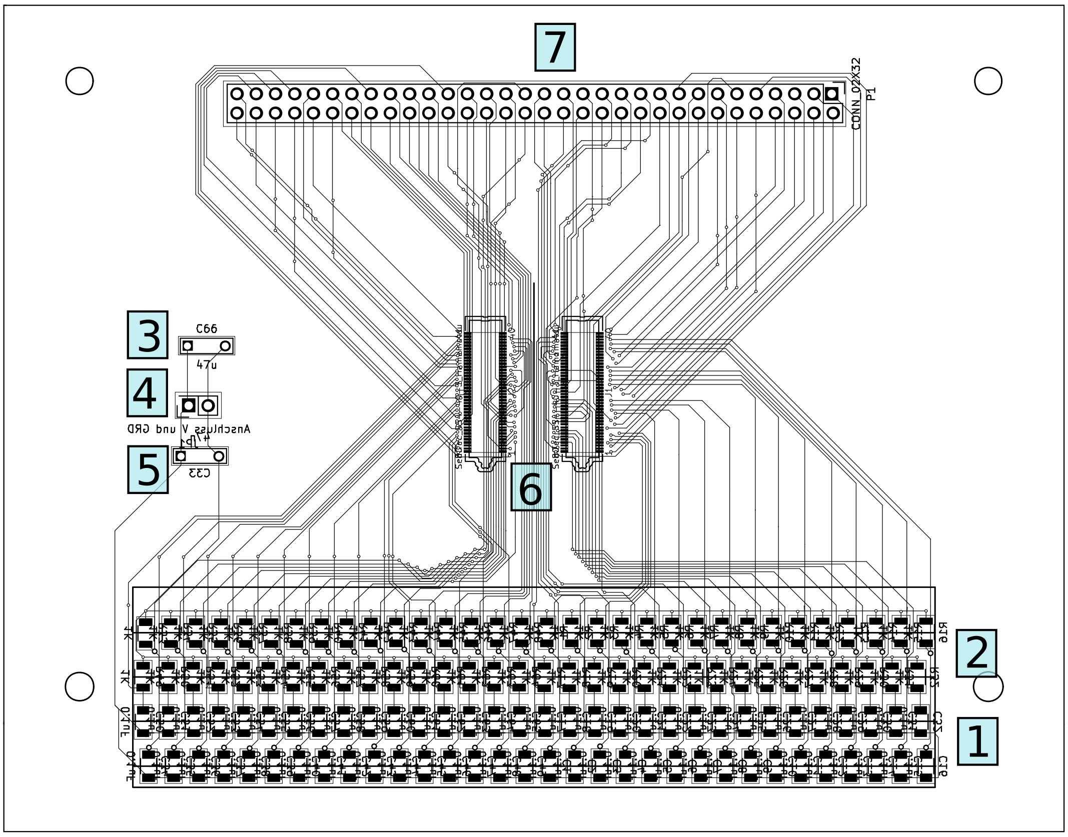

Figure 5.6: Scheme of the SiPM array read-out board version 2. **1:** 64 1 kΩ resistors R1 on the bottom layer. **2:** 64 47 nF capacitors C3 on the bottom layer. **3:** 47 nF capacitor C2. **4:** Bias voltage and ground pins **5:** 47 µF capacitor C2. **6:** Samtec sockets on the top layer. **7:** 2x32 pin header.

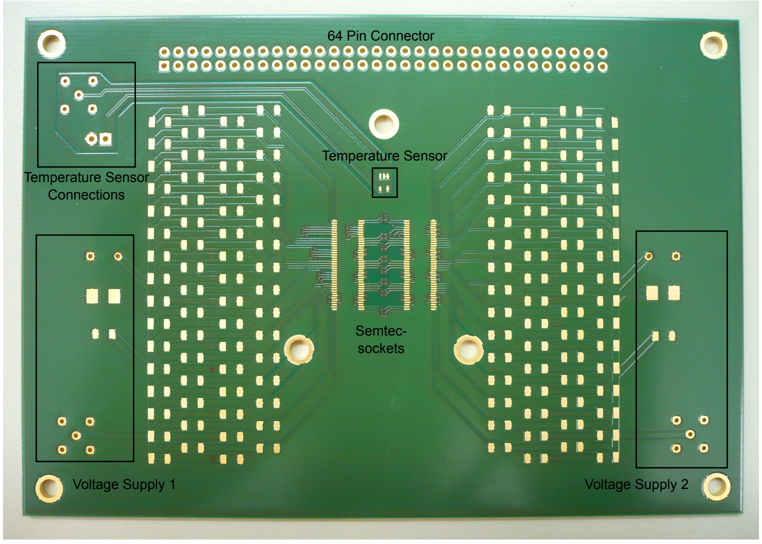

Figure 5.7: Modified version of the read-out board version 2. In this version an additional temperature sensor can be attached to the board and the bias voltage is passed to the board via two Lemo connections. The modifications have been designed by William Painter [37].

A modified version of the read-out board was made by William Painter at the Institute for Nuclear Physics, KIT, including a temperature sensor and two bias voltage inputs (fig. 5.7).
In order to characterise SiPM, the signal has to be amplified. To work with the second version of the SiPM read-out board an additional amplification stage which amplifies the signal of all 64 SiPM channels has to be implemented. An amplification board working together with the second version read-out board was designed by William Painter and was finished at the end of this thesis [37]. A detailed test of the read-out board and the amplification stage was no more possible during this thesis.

SiPM read-out system

Since the use of an amplification stage with the SiPM read-out board version 2 was not possible during this thesis, a stand alone system was designed which includes amplification, multiplexer for switching through the SiPM array channels and a SiPM power supply. The SiPM read-out system consists of an Arduino with an self designed Arduino shield and a SiPM read-out board version 3. An Arduino is an I/O board equipped with a micro-controller and multiple analogue and digital inputs and outputs. An Arduino shield is a PCB that can be plugged on the I/O pins of the Arduino. Figure 5.8 shows a sketch of the read-out system.

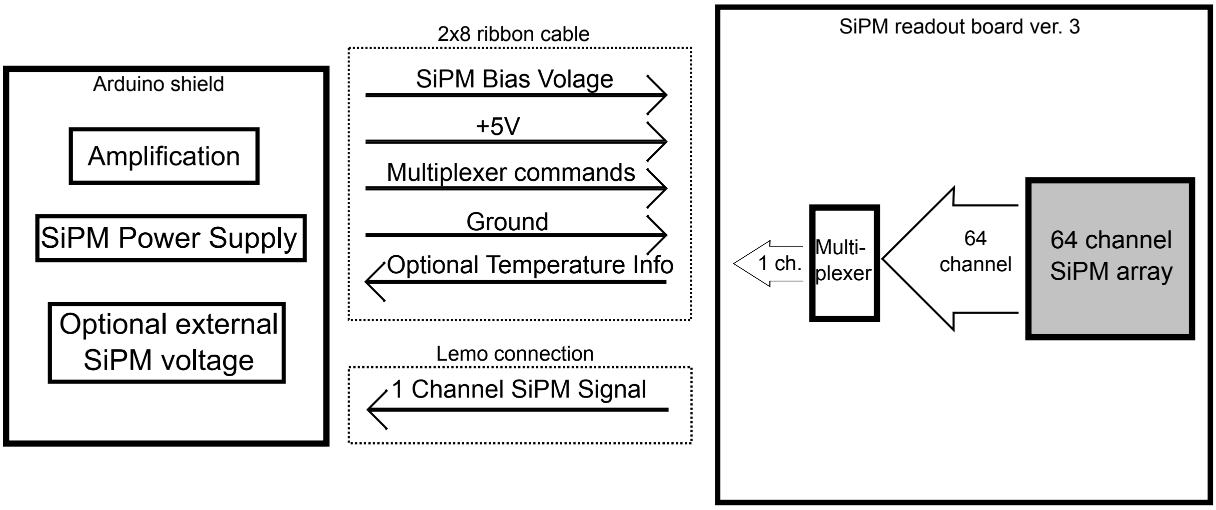

Figure 5.8: Sketch of the SiPM read-out system.

The Arduino shield houses the amplifier, the SiPM power supply and two pins to supply the SiPM with an additional external voltage. The read-out board version 3 consists of the two Samtec sockets and the same capacitors and resistors like the read-out board version 2. Instead of the 2 x 32 pin header, five Mutiplexer ICs, placed on the

PCB, switch to the wanted channel. The signal of the selected channel is passed back to the Arduino shield via a Lemo connection. The Multiplexer ICs are controlled via the Arduino. The Arduino shield and the read-out board are connected with a 2 x 8 lane ribbon cable with which the bias voltage for the SiPM, the voltage for the multiplexer ICs, the multiplexer controlling commands and a possible temperature information are transferred.

Figure 5.9 shows the scheme of the Arduino shield. As SiPM power supply the Hamamatsu power supplies *C11204-01* and *C11204-02* can be plugged on the Arduino shield at position **2**. In addition, an external power supply to operate the SiPM can be used. This external power supply can be connected with pins to the Arduino shield at position **5**. To switch between the internal Hamamatsu power supply and the external power supply, a jumper has to be set (**4**). The ribbon cable which connects the Arduino shield and the SiPM read-out board version 3 can be plugged to the Arduino shield at position **6**. The SiPM signal from the read-out board enters the shield at **7** via a Lemo connection. The SiPM signal is amplified by a factor of 10 with the amplifier IC *LMC6084* which needs supply voltages of +5 V and −5 V. The Arduino provides a voltage of +5 V and ground. To generate a voltage of −5 V for the amplifier IC, the voltage inverter *LM2664* (**3**) is used. The amplified SiPM signal exits the shield at position **8** via a Lemo connection and can be fed into an oscilloscope or a QADC.

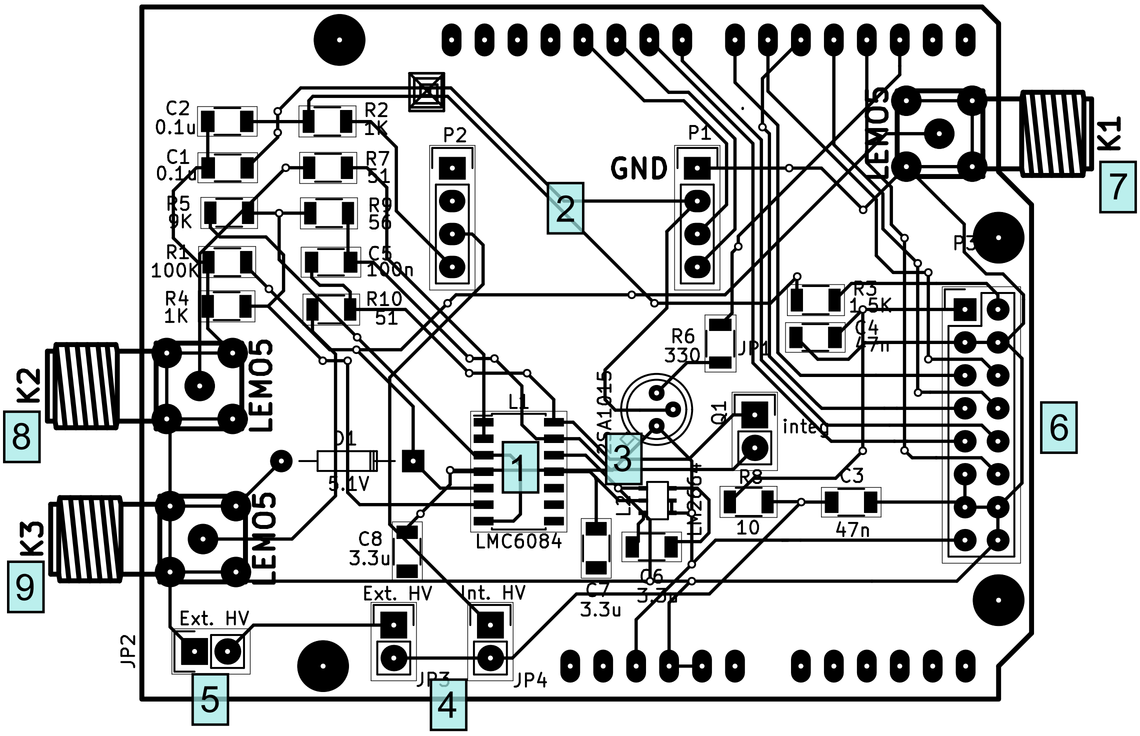

Figure 5.9: Scheme of the Arduino shield. **1:** Amplifier IC *LMC6084*. **2:** Adapter for the Hamamatsu SiPM power supply. **3:** Voltage inverter *LM2664*. **4:** Jumper to switch between the internal Hamamatsu power supply and an external power supply. **5:** Connection for an external SiPM power supply. **6:** 2 x 8 pin header for the connection to the SiPM read-out board version 3. **7:** Lemo connection for the incoming SiPM signal from the SiPM read-out board version 3. **8:** Output of the amplified SiPM signal. **9:** Output of the integrated SiPM signal.

Figure 5.10 shows the SiPM array read-out board version 3 belonging to the Arduino shield. The SiPM read-out circuit stayed the same as in the former version 2 shown in figure 5.8.

The signal of every SiPM channel goes into one of four 16:1 multiplexer ICs *ADG1606* (**8**). Each of these multiplexer chose one channel out of 16 possible. The outputs of the four 16:1 multiplexer go into a next 4:1 multiplexer IC *ADG704* which selects the wanted channel in the end. To select one out of 16 channels with the 16:1 multiplexer IC *ADG1606*, 4 pins of the multiplexer have to be set to high (+5 V) or low (0 V) in a specific combination [57]. To select the final channel out of four with the 4:1 multiplexer IC *ADG704*, two pins have to be set to high or low [58]. All multiplexer ICs have an additional pin to enable (high) or disable (low) them.

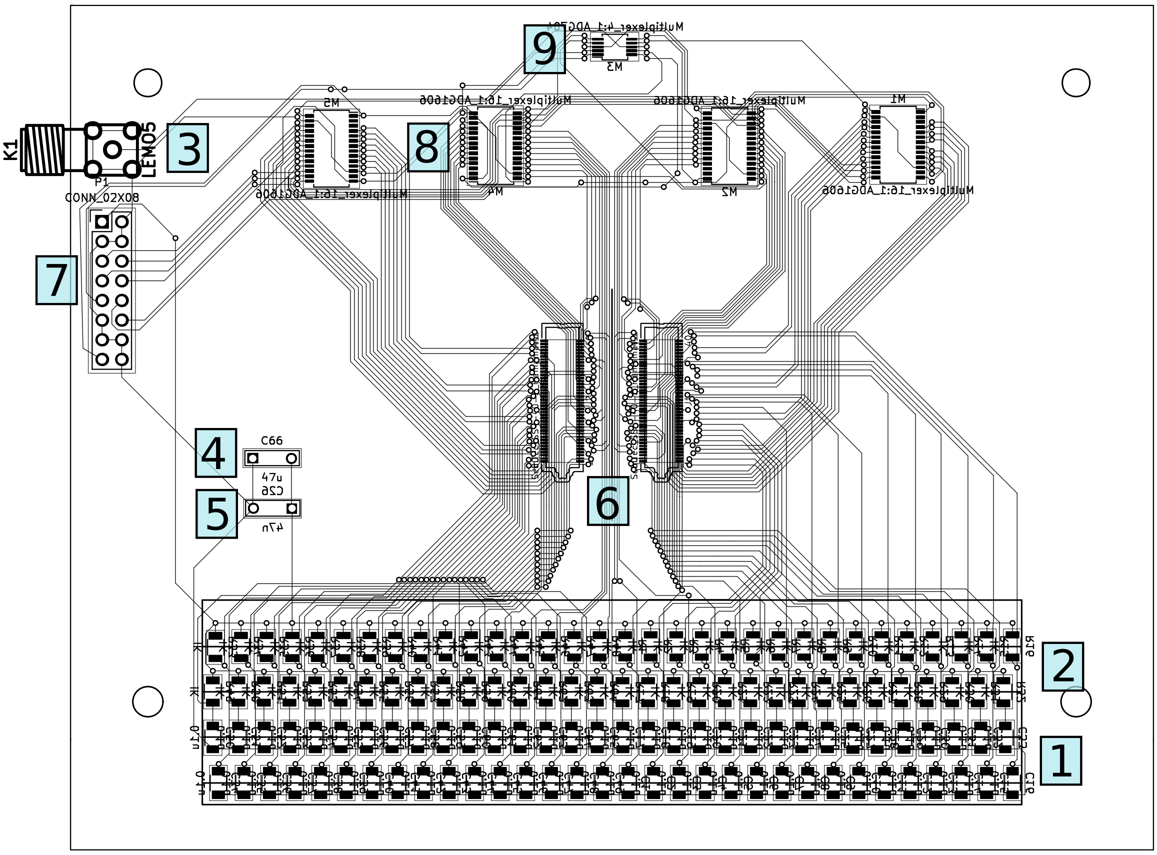

Figure 5.10: Scheme of the SiPM array read-out board version 3 belonging to the SiPM read-out system. **1:** 47 nF Capacitors C3. **2:** 1 kΩ resistors R1. **3:** Lemo SiPM signal exit. **4, 5** : 47 μF and 47 nF capacitors for bias voltage flattening. **6:** Samtec sockets. **7:** 2 x 8 pin header. **8:** Four 16:1 multiplexer ICs *ADG1606*. **9:** 4:1 multiplexer IC *ADG704*.

The commands for the multiplexer are transferred to the read-out board via a 2 x 8 ribbon cable connection from the Arduino shield (7). All of the 16:1 multiplexer receive the same command, the exact channel is chosen with the 4:1 multiplexer. Beside of the multiplexer commands, the bias voltage for the SiPM array, a voltage of +5 V for the multiplexer and ground are transferred via the ribbon cable to the PCB. The SiPM signal leaves the board via a Lemo connection (3) towards the Arduino shield.

The Arduino software and a Python script was written during this thesis to control the multiplexer with the Arduino. To control the Hamamatsu power supply (*C11204-01*) with an Arduino, an electronic circuit, the Arduino software and a Python script was made by Gregor Vollmer at the Institute for Nuclear Physics (IKP) at KIT. This work was improved for the functionality of controlling a new series of the Hamamatsu power supply (*C11204-02*).

During this thesis, the SiPM read-out system could not be tested. At the end of this thesis, tests of the read-out system were ongoing by Tobias Jammer at the University of Tübingen with which we collaborate in the development of SiECA.

SOFTWARE

To characterize SiPM arrays, a Labview measurement control software and a finger spectrum analysing software in Python was written during this thesis. Both of them will be described in the following section.

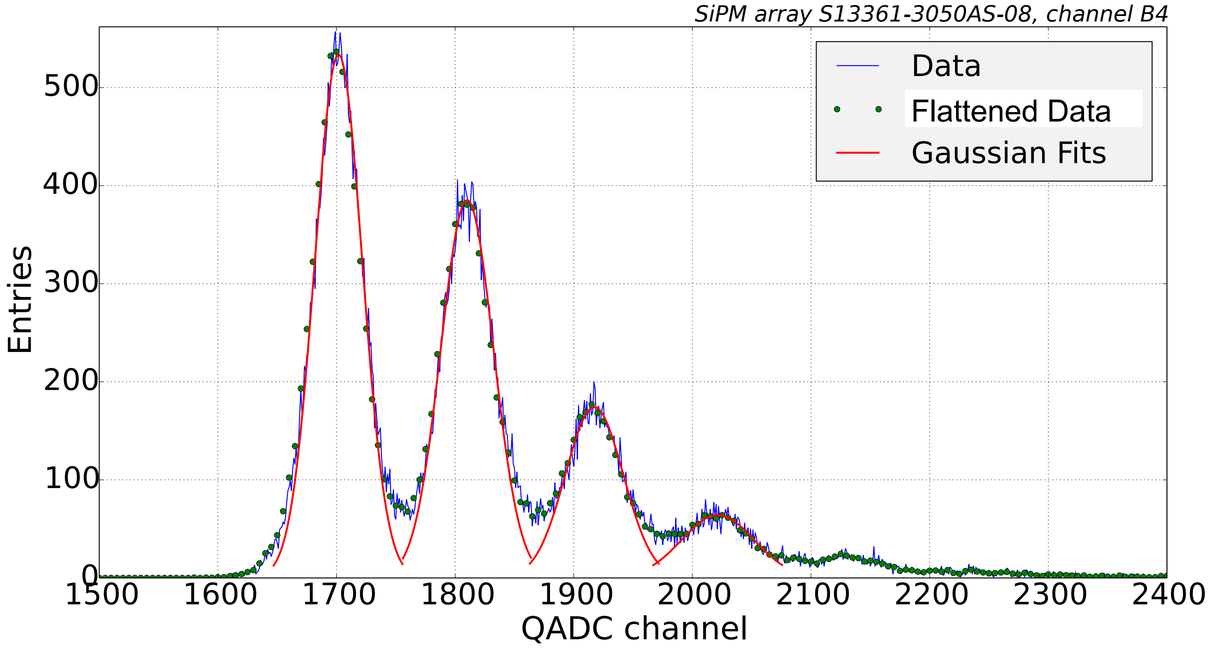

Figure 5.11: Example of a recorded finger spectrum. The QADC channels are on the x-axis and the QADC entries are on the y-axis. The measured data points are connected with lines for better visibility. The flattened histogram, summing up 5 data points to the mean value, is shown as single points. Gaussian fits are included as solid lines. An enhanced view of the second p.e. peak is shown in figure 5.12.

QADC peakfinding algorithm

The QADC integrates the incoming signal during the gate time interval. The result of the integration is saved in units of QADC channels in a text file for a low range ($0\,\mathrm{pC}$ - $100\,\mathrm{pC}$) and a high range ($0\,\mathrm{pC}$ - $900\,\mathrm{pC}$) band. For example, is the QADC set to record 70,000 QADC values, the resulting text file contains 70,000 measured channel entries for the low range and 70,000 measured channel entries for the high range.

The QADC peakfinding algorithm reads the data of one QADC text file and fills the measured entries into histogram bins. A second flattened histogram is made by summing up five consecutive entries and calculating the mean value of them. Figure 5.11 shows an example of a recorded finger spectrum which was analysed with the QADC peakfinding algorithm.

To analyse finger spectra that are highly afflicted with noise, the spectrum peaks are searched in two steps. First, the flattened finger spectrum, shown with points in figure 5.11, is analysed to prepare the scan for peaks in the real data set. Since the flattening reduces fluctuations coming from noise signals and the finite number of recorded QADC values, a first approximation of the finger spectrum peak positions with the flattened data can be made faster and with less effort than with the real data points (see fig. 5.12). The flattened data finger spectrum peaks and the approximate gain, as the distance between consecutive peaks, are calculated.

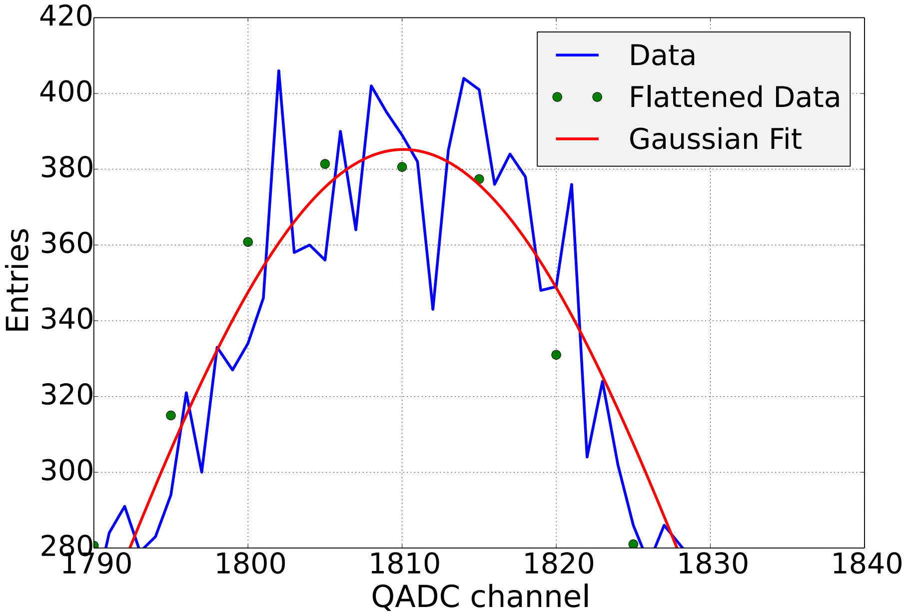

Figure 5.12: Enhanced view of the second p.e. peak of the finger spectrum shown in fig. 5.11.

Following this, the real data is analysed. The algorithm searches spectrum peaks in the area where peaks in the flattened data were found. If a peak is found in the data but is not in the range of the approximate $\pm gain/2$ around a flattened spectrum peak, it is disregarded. If several peaks are found in the data which have the same height in a small distance, like it can be seen at the 2. p.e. peak in figures 5.11 and 5.12, the algorithm takes the first one as real peak and disregards the following. Also peaks which are lower then a tenth of the highest peak are neglected to avoid too many peaks just from random fluctuations at the start and at the end of the finger spectrum.

When the peaks are found in the data, a more precise gain value is calculated with the peaks found in the real data. Gaussian fits of the form

$$f(x) = \frac{A_{peak}}{\sqrt{2 \cdot \pi} \cdot \sigma} \cdot e^{-2 \cdot \left(\frac{x - x_{peak}}{2 \cdot \sigma}\right)^2} \tag{5.1}$$

are adapted to the data in the range of $\pm gain/4$ around a peak. This range is set to avoid that data is included in the fit which does not belong to the peak but to the background noise of the spectrum. In figure 5.11, the Gaussian fits are shown as solid lines. If a fit of a single peak can not be made successfully, the peak is not taken into account for the further calculations.

With the successfully performed fits, the gain in units of QADC channels and the statistical uncertainty of the gain is calculated. The gain is the distance between two consecutive peaks (section 4.5). For the gain calculation only the first three peaks are considered. Is the peak position of the pedestal peak at x_0, for the first p.e. peak at x_1 and for the second p.e. peak at x_2 with statistical uncertainties σ_{x_i}, the gain $G_{channel}$ in units of QADC channels and the statistical uncertainty $\sigma_{G_{channel}}$ of the gain are calculated as

$$G_{channel} = \frac{(x_1 - x_0) + (x_2 - x_1)}{2} \tag{5.2}$$

$$\sigma_{G_{channel}} = \frac{2\sigma_{x_1} + \sigma_{x_2} + \sigma_{x_0}}{2}. \tag{5.3}$$

The median of the finger spectrum is investigated to obtain information about the number of firing APDs. Since the position of the finger spectrum in QADC channels can change during different measurements, the median x_{med} in units of QADC channels is calculated relative to the pedestal peak position. The median is calculated with the raw median $x_{med,raw}$ to

$$x_{med} = x_{med,raw} - x_0 \tag{5.4}$$

$$\sigma_{x_{med}} = \sigma_{x_{med,raw}} + \sigma_{x_0} \tag{5.5}$$

with the pedestal peak position x_0.

The peakfinding algorithm takes the QADC file that has to be analysed as argument. As output, the peakfinding algorithm gives the results of the fits of the found peaks, the gain, the median and the number of events in the pedestal peak with the statistical uncertainty of each value. In addition, the QADC peakfinding algorithm was adapted to search only for the first pedestal peak in order to analyse the dark spectrum.

Labview measurement program

To control the measurements, the Labview program of SPOCK with which the measurements were made (see section 6.1) was adapted to measure SiPM arrays during this thesis. *RS-232* interfaces to multimeter and power supplies were written in Python and embedded in the Labview program. Figure 5.13 shows the measurement control interface.

Several measurement specific parameters can be adjusted before the measurement. The number of measured QADC values for the finger and dark spectra for obtaining gain, PDE and the dark count rate and the number of QADC values for the finger spectra with which the breakdown voltage is calculated can be changed at **1**. As standard values, the QADC measures 70,000 values for the gain, PDE and dark count rate measurement and 15,000 values for each finger spectrum in the breakdown voltage measurement.

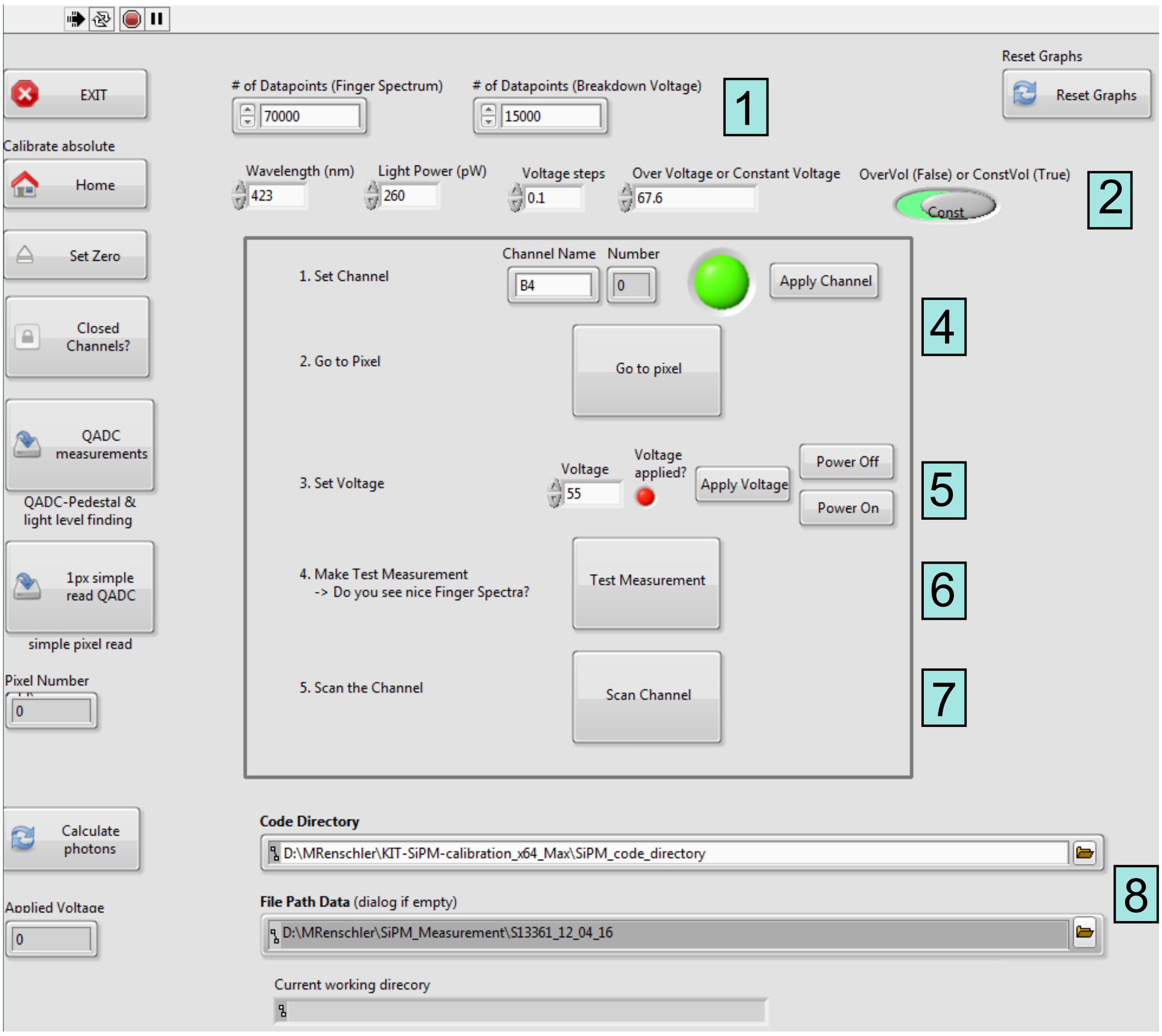

# of Datapoints (Finger Spectrum): 70000
# of Datapoints (Breakdown Voltage): 15000
Wavelength (nm): 423
Light Power (pW): 260
Voltage steps: 0.1
Over Voltage or Constant Voltage: 67.6
OverVol (False) or ConstVol (True): Const
Channel Name: B4
Number: 0
Voltage: 55
Voltage applied?
Pixel Number: 0
Applied Voltage: 0
Code Directory: D:\MRenschler\KIT-SiPM-calibration_x64_Max\SiPM_code_directory
File Path Data (dialog if empty): D:\MRenschler\SiPM_Measurement\S13361_12_04_16
Current working direcory

Figure 5.13: Interface of the measurement control Labview program.

At **2**, the voltage steps in the breakdown voltage measurement can be chosen. The standard are voltage steps of 0.1 V length. It can be chosen whether the gain, PDE and dark count measurement should be made at a constant bias voltage or at a constant over-voltage based on the breakdown voltage measurement made before by using the switch at position 2. The bias voltage or the constant over-voltage for these measurements can be set.
In **3** and **4** the wanted channel can be selected by type in the channel name and press 'Apply Pixel'. If the channel name is wrong, the program shows an error message. With 'Go to Pixel' the integrating sphere moves to the chosen pixel. The starting voltage for the breakdown voltage measurement can be set at **5**. Also, the voltage can be switched on and off. The voltage is controlled by an *RS-232* interface to the power supply *TTi El302P* which was written in Python and embedded in Labview during this thesis. A first test measurement can be made at **6** to see if the chosen voltage is sufficient to see a finger spectrum. With 'Scan Channel' (**7**), the measurement of the chosen channel starts. The actual working directory can be chosen at **8**. The Labview program will create a new folder for every measured channel in the chosen work directory.
The Labview program automatically uses the QADC peakfinding algorithm described above to perform fits to every finger spectrum or dark spectrum recorded. If the fits of a finger or dark spectrum can not be made successfully, the program stops and outputs an error message. This routine was implemented to prevent the user of loosing measurement time because bias voltage or light intensity were not set properly. The breakdown voltage is calculated using the method of extrapolating the gain vs. bias voltage behaviour to a gain of zero within the Labview program (see section 4.5). The fit results and the result for the breakdown voltage are saved in text files in the channel folder which is created.

6

MEASUREMENT SETUP

The measurements in this thesis were made with the Single PhOton Calibration Stand at Kit (SPOCK). In this chapter, the components of SPOCK will be presented and the measurement setup will be described. Also, information about the observed SiPM waveform and the noise phenomena, which influenced the measurements, will be given.

SINGLE PHOTON CALIBRATION STAND AT KIT (SPOCK)

SPOCK was build to characterize PMTs and a wide range of other photo sensors like SiPM with the highest precision possible. It consists of a reference light source, photon shielding and the read-out electronics.
The photon shielding is a wooden box covered on the inside with black flock paper. Figure 6.1 shows a photograph of SPOCK with opened lid.

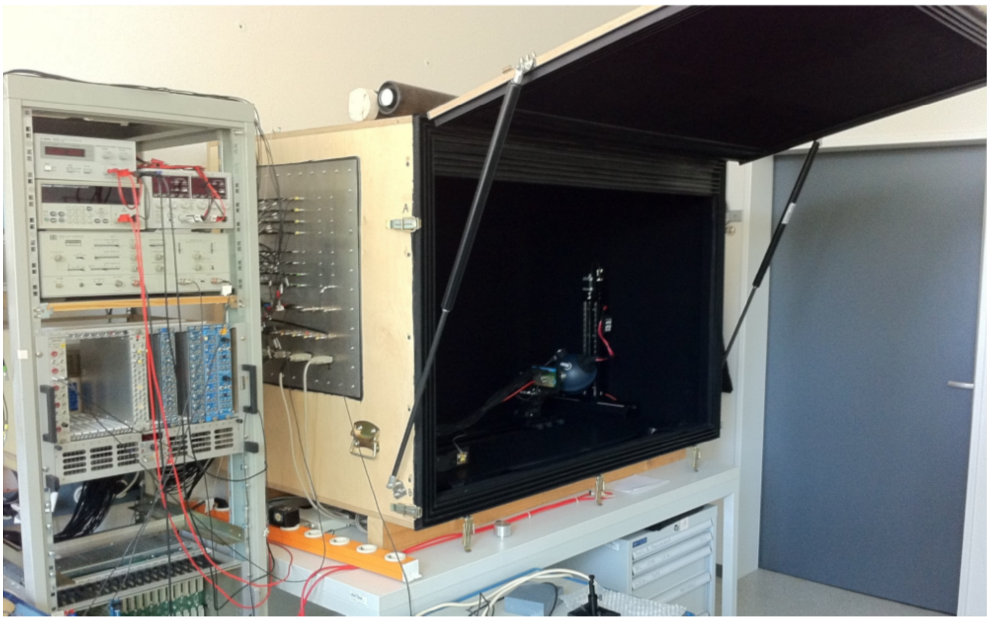

Figure 6.1: Outside view on the calibration stand SPOCK [19].

The lid of the photon shielding box can be lifted and kept open with two pneumatic springs. The lid and the edges of the box close light-tide with three shifted profiles which intertwine when the lid is closed. At the left side of the photon shielding box, a light-tide aluminium panel is mounted. Connectors for the voltage supply of the detector, the LEDs and several electronic devices as well as the detector output signals enter and leave the shielding box via the panel.

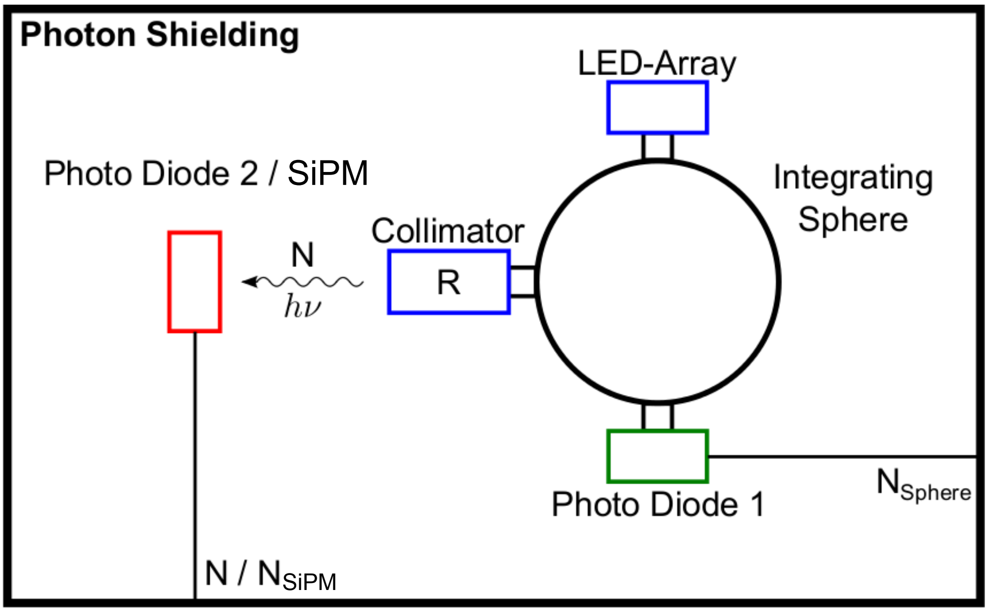

Figure 6.2: Schematic view of the calibration principle of SPOCK [59].

Figure 6.2 shows a schematic view of the calibration principle of SPOCK. Inside the photon shielding box, the reference light source is located which consists of an integrating sphere, an LED-array, a NIST[1]-calibrated photo diode and a collimator.
The integrating sphere is a *Labsphere 3P-GPS-053-SL* with a diameter of 13.5 cm. It has two 2.54 cm diameter exit ports and one 6.35 cm diameter entrance port which is used for the LED-arrays. The inside of the sphere is covered with *Spectralon SRM-99O*[2] which reflects 95% - 99% of the UV light in the range of 250 nm to 400 nm [60]. Due to the integrating spheres functioning as a splitter and diffuser for the emitted photons by the LED-array as well as due to the equal size of the two exit ports, the photon flux through the two exit ports should be the same. A slight difference in the fluxes through the two exit ports was measured in [19, 48]. This discrepancy in the fluxes is taken into account by measuring the collimator ratio.
The number of photons leaving one exit port N_{sphere} is measured with the NIST-calibrated photo diode *OSI Opto-electronics UV-100* (Photo Diode 1 in figure 6.2). To evaluate the collimator ratio R, the number of photons through the second exit port N_R equipped with the collimator can be measured with a second photo diode by

---

[1] National Institution of Standards and Technology

[2] PFTE (Polytetrafluorethylen)

placing it in front of the collimator exit (Photo Diode 2 in figure 6.2). The collimator ratio R can then be calculated as

$$R = \frac{N_R}{N_{\text{sphere}}}. \tag{6.1}$$

Typical collimator ratios are in the region of $R = 10^{-6}$ providing a low enough light intensity for a single photon calibration. Figure 6.3 shows the available PVC[1]-collimators in SPOCK. During this thesis the collimator *ColE* with an entrance hole diameter of 5.0 mm and an exit hole diameter of 0.5 mm was used.

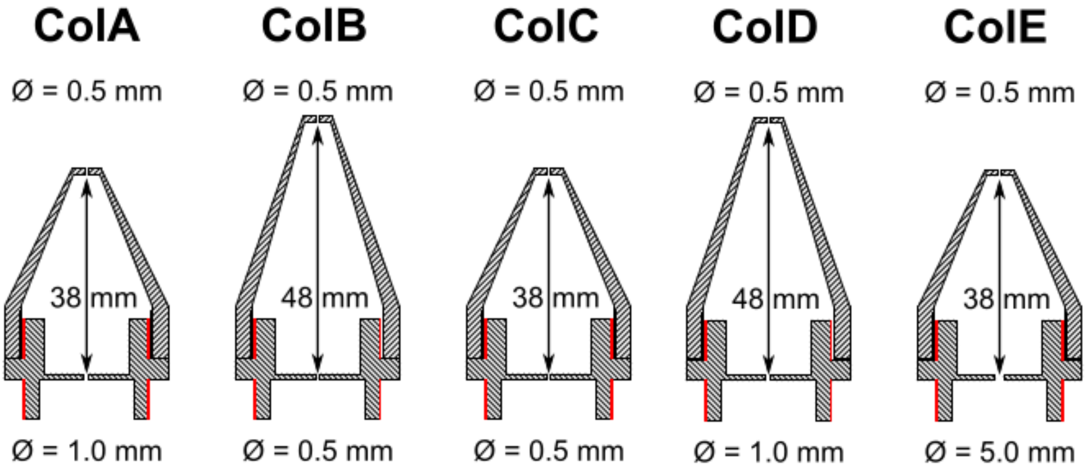

Figure 6.3: Available PVC-collimators for SPOCK. For each collimator the diameter of the entrance and exit hole as well as the length of the collimator sphere is given [19].

LED-arrays

During this thesis, four LED-arrays were available to be mounted to the integrating sphere. Each LED-array consists of multiple LEDs of the same type (fig. 6.4). The LED in the middle of the array can be operated in pulsed mode, the other LEDs are for the use in continuous mode. Regarding the collimator ratio measurement, the optical power has to be large since the collimator reduces the light intensity by a factor of 10^6 but the exiting optical power has still to be high enough to be measurable with the second photo diode. Due to this, the multiple LEDs of each LED-array emitting light in continuous mode are used for the collimator ratio measurement. For the actual SiPM characterizing measurements, a pulsed light source is needed and the single pulsed LED in the middle of each array is chosen.

---

[1] Polyvinylchlorid

LED-array	LED	Number of LEDs	Wavelength (nm)
Array 1	*UVLED365-110E*	42+1	371 ± 6
Array 2	*XSL-375-3E*	20+1	376 ± 5
Array 3	*VL390-5-15*	42+1	395 ± 7
Array 3	*VL425-5-15*	12+1	423 ± 8

Table 6.1: Overview of the four available LED-arrays [19]. Shown are the used LEDs, the number of LEDs and the wavelength of the LEDs together with the statistical uncertainty for each LED array.

Table 6.1 gives information about the LED types, the number of LEDs and the wavelength of the LEDs for each of the four arrays. For the required measurements in this thesis, mainly LED-array 4 with LEDs with a wavelength of 423 nm was used. To investigate the wavelength sensitivity of the SiPM arrays, measurements with all of the four LED-arrays have been performed.

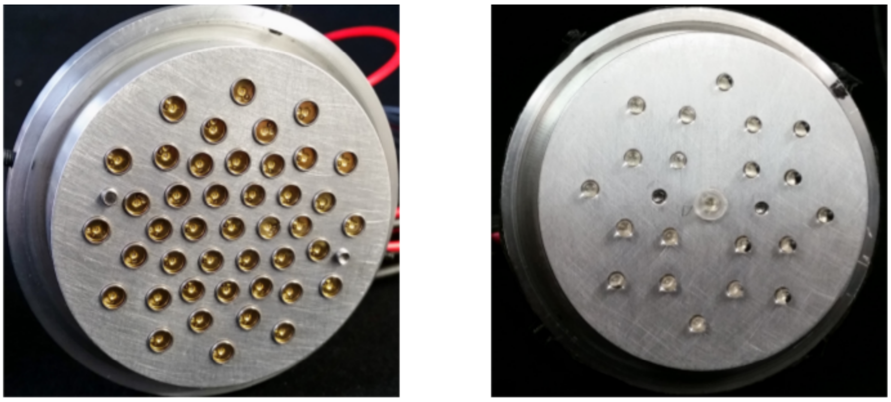

(a) LED-array AR1. **(b)** LED-array AR2.

(c) LED-array AR3. **(d)** LED-array AR4.

Figure 6.4: Available LED-arrays in SPOCK [19]. All arrays are made out of aluminium. Each array has a different type of LED. An overview of the used LEDs and their wavelengths can be found in table 6.1.

MEASUREMENT SETUP

Figure 6.5 shows a flowchart of the measurement setup. The pulsar *HP8082A* generates a NIM-pulse and an inverted NIM-pulse. Following the left hand side of the flowchart, the inverted NIM-pulse is passed to the Light Diode Driver (LDD) *Cern-NP N4168*. The LDD generates the signal for the pulsed single LED in the LED-array. With the LDD, the optical power emitted to the detector is adjustable.

At the same time, the non-inverted NIM-pulse of the pulsar is passed to a gate generator (right hand side of flowchart 6.5) which generates the gate for the QADC. The gate length is adjustable at the gate generator. For the measurements in this thesis, a gate length of 73 ns was chosen with which the largest part of the SiPM signal is covered and possible after-pulses are avoided (see fig. 6.6). Due to the Lemo connections from the LDD to the LED and from the SiPM back to the QADC, the SiPM signal and the

gate are not synchronous. To compensate the belated SiPM signal, the gate is delayed before entering the QADC. The QADC starts to integrate the incoming SiPM signal 15 ns after the gate signal was detected.
To be able to process the SiPM signal with the QADC, the signal has to be amplified and inverted. To amplify the signal, the SiPM driver circuit board *C12332* from Hamamatsu was used. Originally, this board is made to operate one channel SiPM with an integrated SiPM power supply and an amplification circuit. Modifications to the board were made by Bernd Hoffmann from the Institute for Experimental Nuclear Physics (IEKP) at KIT to pass external signals with a Lemo connection to the amplifier circuit of the *C12332*-board. To amplify the signal on the board, the amplifier IC *OPA864* from Texas Instruments is used which amplifies the signal with a factor of 10 [61, 62].
To invert the amplified SiPM signal, a fan-in/fan-out model *428F* made by LeCroy was chosen.

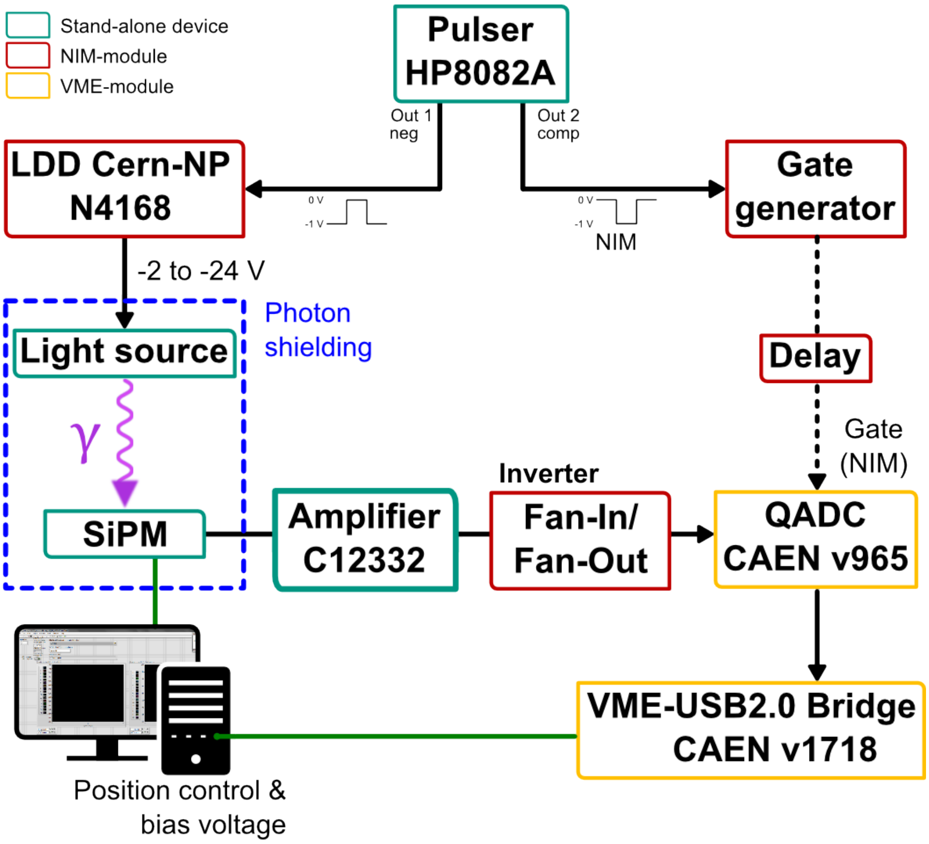

Figure 6.5: Flowchart of the measurement setup (Modification of a figure made by Michael Karus in [19]).

The amplified and inverted SiPM signal is passed to the Queued Analogue-to-Digital Converter (QADC) *CAEN v965*. During the gate interval, the QADC first converts the incoming charge into a voltage level (Charge-to-Amplitude Converter (QAC)). The voltage level is digitalized by an ADC which outputs the result in units of QADC channels. With this result, the real charge generated by the signal can be calculated. The QADC *CAEN v965* has 16 input channels and two measurement bands from $0\,\mathrm{pC} - 100\,\mathrm{pC}$ (LR) and $0\,\mathrm{pC} - 900\,\mathrm{pC}$ (HR) [63]. The digitalized QADC results are send to a *CAEN v1718* controller which works as an interface to the measurement PC. Information about the calibration of the QADC can be found in [19]. During this thesis, only channel zero was used and all measurements were performed within the LR band. The transformation factor k from QADC channels to charge for channel zero is [19, 49]

$$k = (32.08 \pm 1.57_{stat} \pm 1.24_{sys})\,\mathrm{pC}. \tag{6.2}$$

The measurement is controlled with the measurement Labview program as presented in section 5.2.

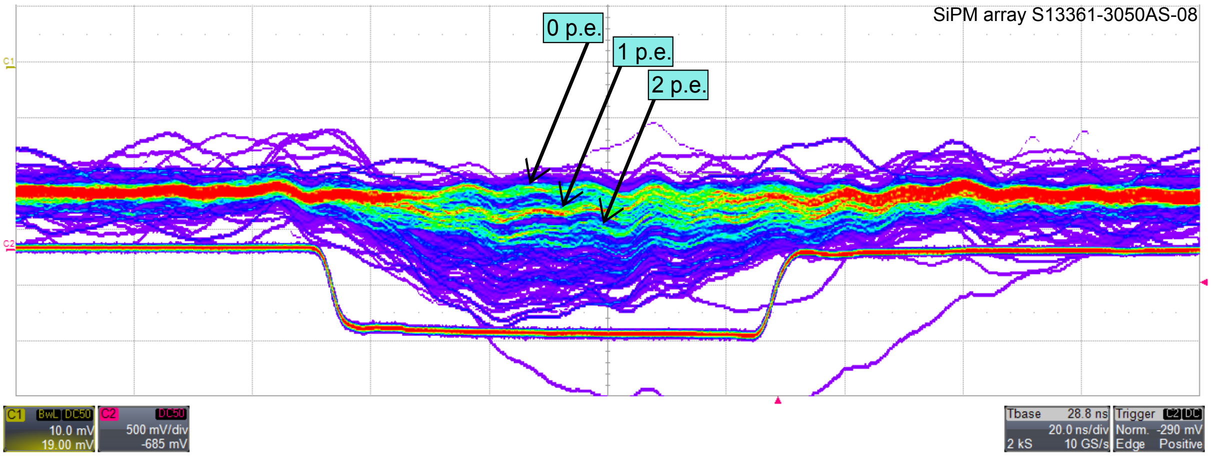

Figure 6.6: Figure of a persistence measurement consisting of several thousand single measurements of one channel of the SiPM array *S13361-0305AS-08*. The gate interval in which the QADC integrates the SiPM signal is shown underneath the SiPM signals. The time division of the plot is $20\,\mathrm{ns/div}$. The voltage division for the SiPM signals is $10\,\mathrm{mV/div}$.

MEASUREMENT PROCEDURE

Before calibration measurements of a SiPM array can start, the integrated sphere has to be aligned. To be able to drive the integrated sphere to the precise position of every channel of the array, the position of the collimator exit has to be set as a reference point. Also attention has to be paid that the light exiting the collimator hits only one channel and is not partially emitted to a neighboured channel or to the gap between two channels. This was done by moving the integrated sphere with the collimator exit over the approximate position of channel 01 and then finding the exact position by

analysing the SiPM signals. To find the precise position, light was emitted to the SiPM and the position of the integrated sphere was slightly changed until the SiPM signal had a maximal amplitude.
At the beginning and at the end of every measurement day, collimator ratio measurements have been performed. This was made to consider changes of the collimator ratio because of temperature variations and slight changes of the collimator ratio because of variations in the distance of the collimator exit and photo diode due to measurement uncertainties. Collimator ratio measurements were done by positioning photo diode 2 in front of the collimator exit in the same distance to the collimator exit like the SiPM surface. The collimator ratio was measured according to equation 6.1 by measuring the optical power in the integrated sphere and the optical power after the collimator exit and calculating the fraction of these two values.

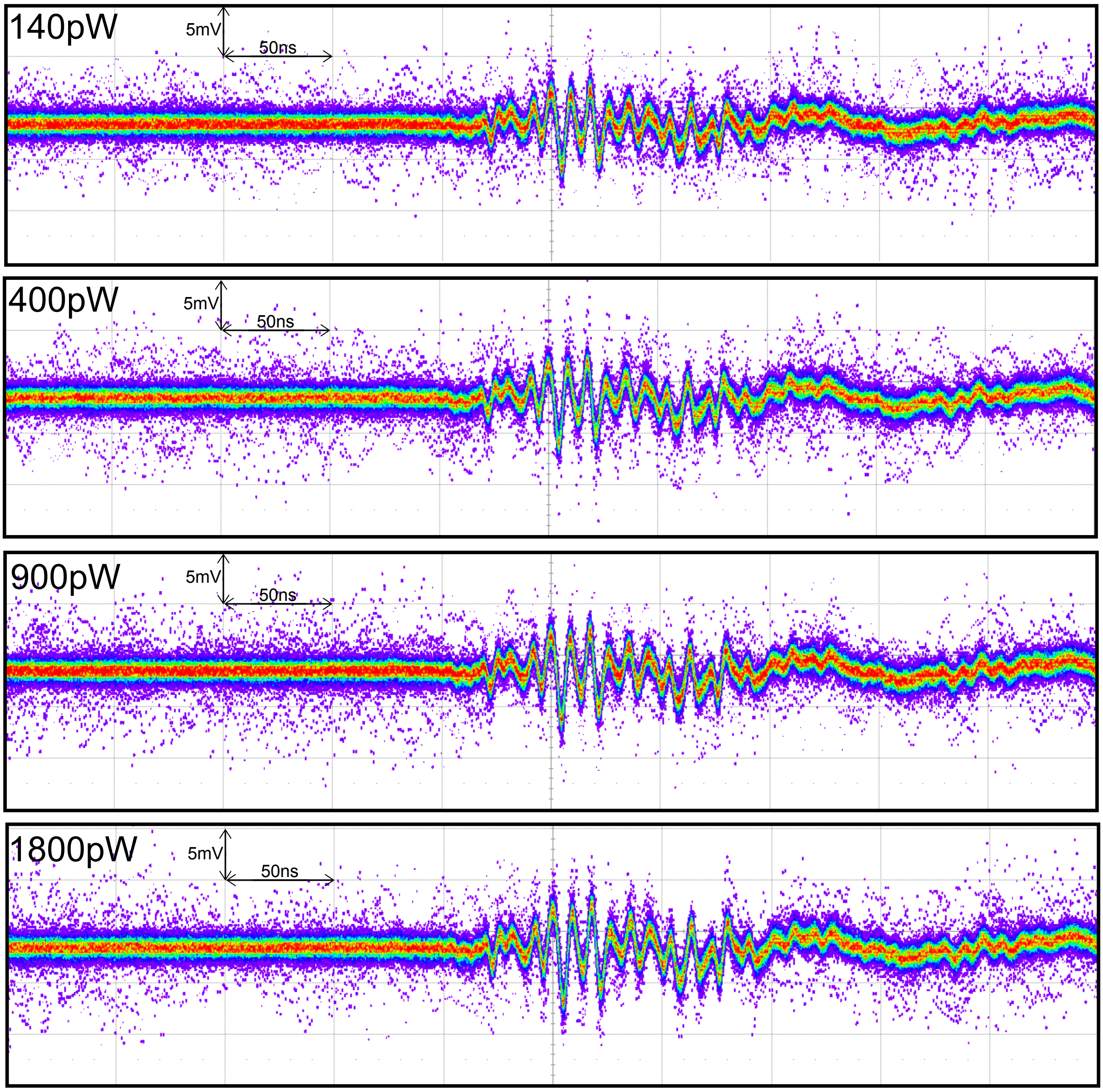

Figure 6.7: Noise signals of the pulsed LED in LED-array 4 for different optical power levels. The signals have been recorded with the SiPM array read-out board version 1 but with a not-powered SiPM. The noise amplitude increases with increasing optical power which is visible for example by looking at the amplitude of the signal around $t = 0s$.

Starting the measurement with the Labview measurement control software, the measurement for the breakdown voltage is performed first. For this, 15 finger spectra at different voltages are recorded. Each of the finger spectra contains 15,000 QADC values. To evaluate the PDE and the gain, a finger spectrum with 70,000 QADC values at a constant bias voltage is measured after this. At the end, a dark measurement is performed at the same bias voltage like the former light measurement and again with a number of 70,000 recorded QADC values. To switch off the light source for the dark measurement, the Lemo connection to the pulsed LED in the LED-array is interrupted. During the measurement with an active light source, the optical power in the integrating sphere is monitored and recorded.

The recorded finger spectra were analysed with the QADC peakfinding algorithm (section 5.2). The calculation of the breakdown voltage, the gain, the PDE, the dark count rate and the crosstalk probability was made according to the methods presented in section 4.5 with several Python scripts developed during this thesis.

SIPM WAVEFORM AND NOISE PHENOMENA

Due to the unshielded two copper layers of the SiPM array read-out board (version 1) which was used for performing the measurements, the characterizing measurements of the SiPM arrays were very noise afflicted. Figure 6.6 shows a persistence measurement consisting of several thousand single measurements of a channel of the latest series SiPM array[1] from Hamamatsu which was charaterized during this thesis. SiPM signals consisting of zero, one and two firing S-APDs are visible. The gate interval in which the QADC integrates the SiPM signal is shown in figure 6.6 underneath the SiPM signal waveform.

A random noise was detected during the measurements which had its origin in the surrounding laboratories. An actual source of these noise signals could not be identified during this thesis. The effect of this noise is a clearly visible 'wash-out' of the signal line. A second constant noise source was the pulsed LED. Beside of the photon emission, LEDs emit also electromagnetic waves in the radio band. These radio signals couple into the wires of the read-out board and change the waveform of the signal. This constant noise produced by the LED is visible in figure 6.6 as a deformation of the baseline. The amplitude of the LED noise signal increases with increasing optical power produced by the LED (see fig. 6.7). Since the waveform of the LED noise signal is constant for every LED pulse, a characterizing measurement with the QADC is still possible. The optical power of the LED, and with this the strength of the noise signal, was reduced as much as possible in the measurements made during this thesis.

---

[1] SiPM array Hamamatsu *S13361-0305AS-08*

7

MEASUREMENTS AND RESULTS

FUNCTIONALITY TESTS OF THE SIPM ARRAYS AND THE READ-OUT BOARD

As a first test of the read-out-board version 1 as well as of the SiPM arrays *S13361-3050AS-08* (*S13*) and *S12642-0808PA-50* (*S12*) to be characterized, the approximate breakdown voltage and the approximate dark-count rate have been measured with the methods introduced in section 4.5. The purpose of these first approximate measurements was to roughly check the manufacturers predictions of the breakdown voltage and the dark-count rate and to proof the general functionality of the read-out board and the SiPM arrays. A scheme of the channel names and numbers can be found in the Appendix section 9.1.

APPROXIMATE BREAKDOWN VOLTAGE A first approximation of the breakdown voltage of the SiPM arrays *S12* and *S13* was estimated by recording a voltage-current curve for every channel of the arrays, fitting two linear functions to the baseline and the slope and searching for the crosspoint of these two linear functions like it is explained in section 4.5.

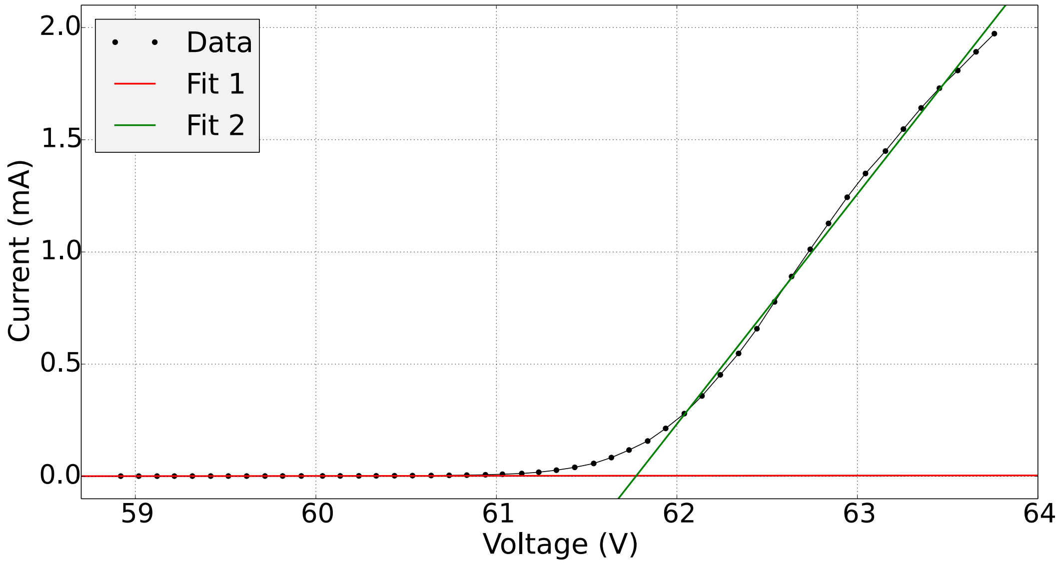

Figure 7.1: Example of a measurement of the approximate breakdown voltage of a SiPM channel. The breakdown voltage is defined as the crosspoint of the two linear fits. This is a measurement of channel B3 of array *S13*.

Figure 7.1 shows an example measurement of the breakdown voltage determination. The recorded voltage-current values for channel B3 of array *S13* are plotted together with the linear fits of the data points 1.5 V before and after the obvious breakdown voltage. In this example the results for the fits are

$$f1 = -0.034\frac{mA}{V} + x \cdot 0.0005\frac{mA}{V} \tag{7.1}$$

$$f2 = -63.32\frac{mA}{V} + x \cdot 1.025\frac{mA}{V}. \tag{7.2}$$

The breakdown voltage calculated by the crosspoint of the lines is $(61.77 \pm 0.02)\,V$. The measurements were done with SPOCK without shining light on the SiPM arrays. The temperature during the measurements was about 21.3°C. The figures 7.2 and 7.3 show the measurement results for all channels.

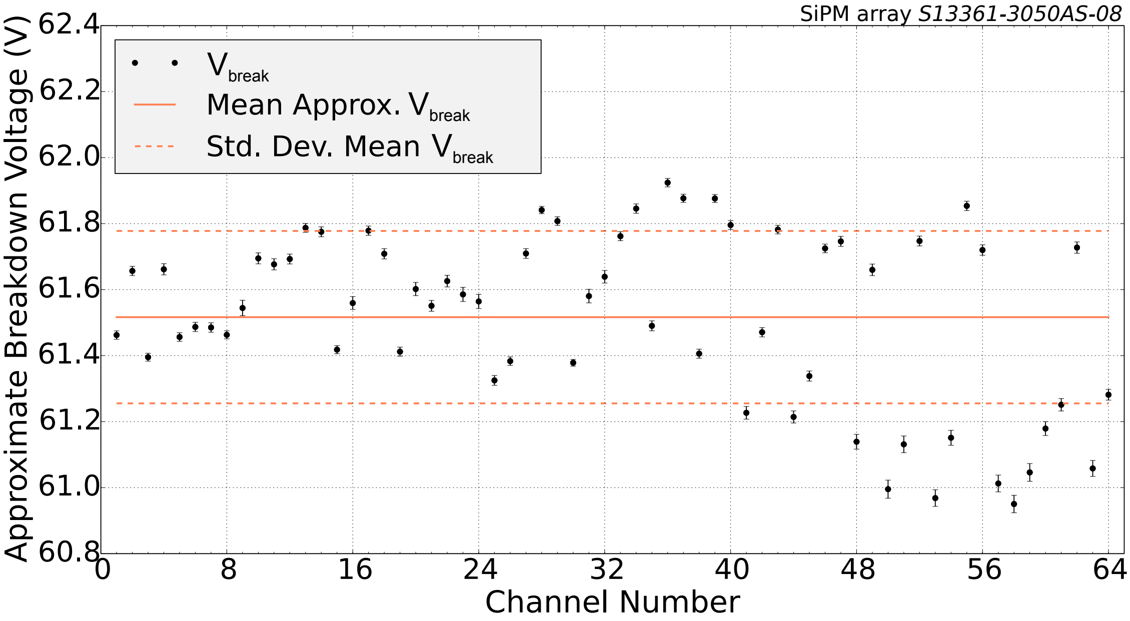

Figure 7.2: Approximate breakdown voltage for SiPM array *S13* at a temperature of approximately 21.3°C. The statistical uncertainty is shown by black error bars.

The average breakdown voltage over all the 64 channels of the arrays results to

$$V_{\text{break, approx}} = (61.52 \pm 0.26)\,\text{V} \qquad \text{for array } S13 \tag{7.3}$$

$$V_{\text{break, approx}} = (69.91 \pm 0.09)\,\text{V} \qquad \text{for array } S12. \tag{7.4}$$

Because this is just a first approximation of the breakdown voltage, the only error shown in fig. 7.2 and 7.3 is the error of the crosspoint calculation of the two linear fits resulting from the error of the linear fits. A more detailed uncertainty analysis will be done for the exact measurement of the breakdown voltage later. The figures 7.6 and 7.8 show the distribution of the breakdown voltages over the whole arrays with 64 channels each. The wide distribution of the single breakdown voltage values of the channels has its origins in the approximate method of finding the breakdown voltage and the fact, that the breakdown voltages are not perfectly uniform over the whole arrays due to constructional reasons. A deviation from a mean value over all the channels is expected.

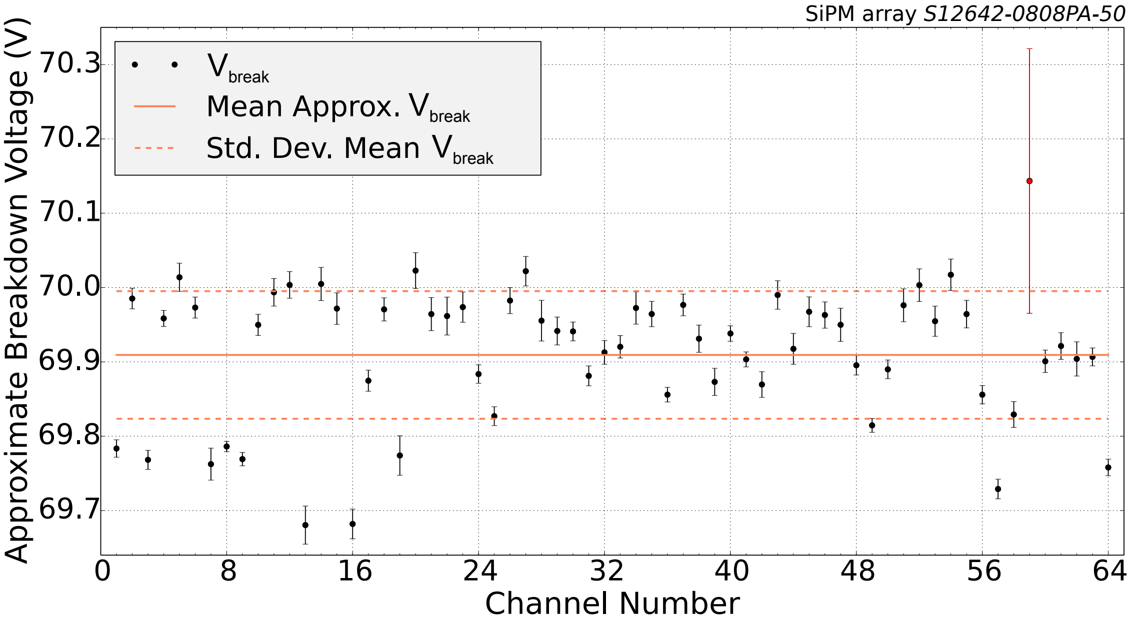

Figure 7.3: Approximate breakdown voltage measurement for SiPM array *S12* at a temperature of 21.3°C. The statistical uncertainty is shown with black error bars. For channel H3 (channel number 59) the crosspoint calculation failed.

APPROXIMATE DARK-COUNT RATE A first approximation of the dark-count rate ξ for both SiPM arrays was done by taking around 300 samples of a time length of $50\,\mathrm{ns}$ with the oscilloscope for every channel and searching for signal peaks with a peakfinding algorithm like it is described in section 4.5. Again, the SiPM arrays have been placed inside SPOCK. For every channel of both arrays, the dark-count rate measurement took place right after the recording of the voltage-current curve for calculating the approximate breakdown voltage. The temperature during theses measurements was 21.3°C.

Because this is a first approximation of the dark-count rate, the error analysis stays on a basic level regarding only the statistical error of the peakfinding algorithm given in [48] of $18 \cdot 10^3 \frac{1}{\mathrm{s}}$. The figures 7.4 and 7.5 show the results of the approximate dark-count measurements. The dark-count rate was measured at a bias voltage of 61.5 V for array *S13* and 71.5 V for array *S12*. These voltage were chosen according to the approximate breakdown voltage measurements. For this voltage, the average approximate dark-count rates of both array are

$$\xi_{\mathrm{approx.}} = (0.31 \pm 0.22) \cdot 10^6\,\mathrm{Hz} \qquad \text{for array } S13 \tag{7.5}$$

$$\xi_{\mathrm{approx.}} = (4.54 \pm 0.41) \cdot 10^6\mathrm{Hz} \qquad \text{for array } S12. \tag{7.6}$$

The figures 7.7 and 7.9 show the distribution of the dark-count rates over all the 64 channels of the arrays.

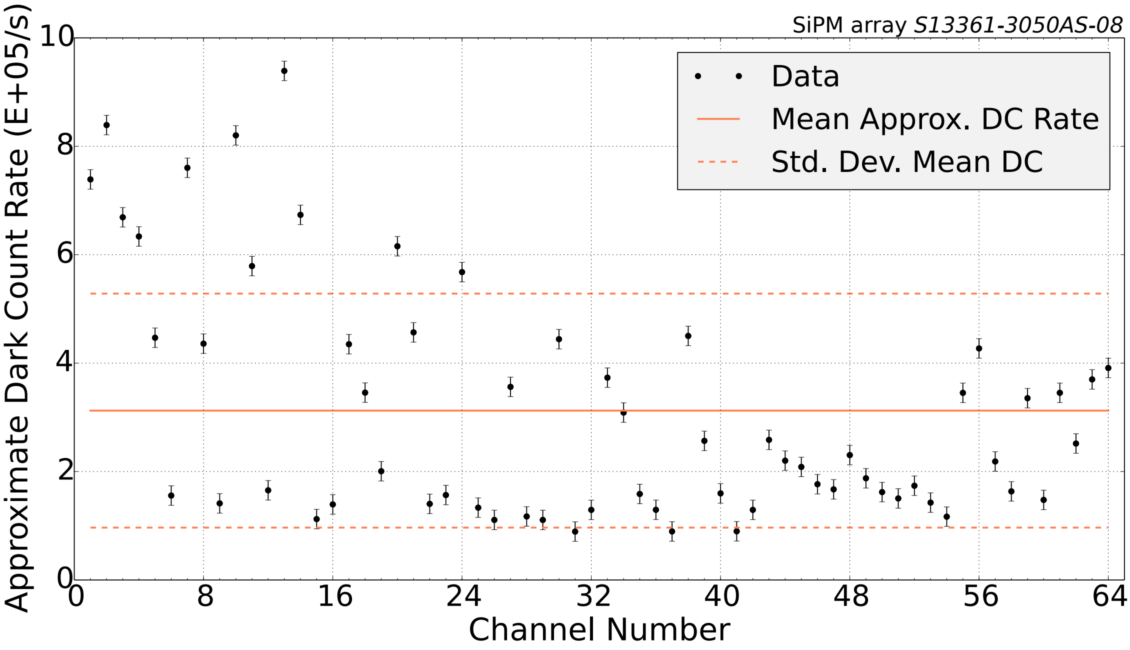

Figure 7.4: Approximate dark-count rate measurement for *S13* at a temperature of around 21.3°C and a bias voltage of 61.5 V. The statistical uncertainty is shown with black error bars.

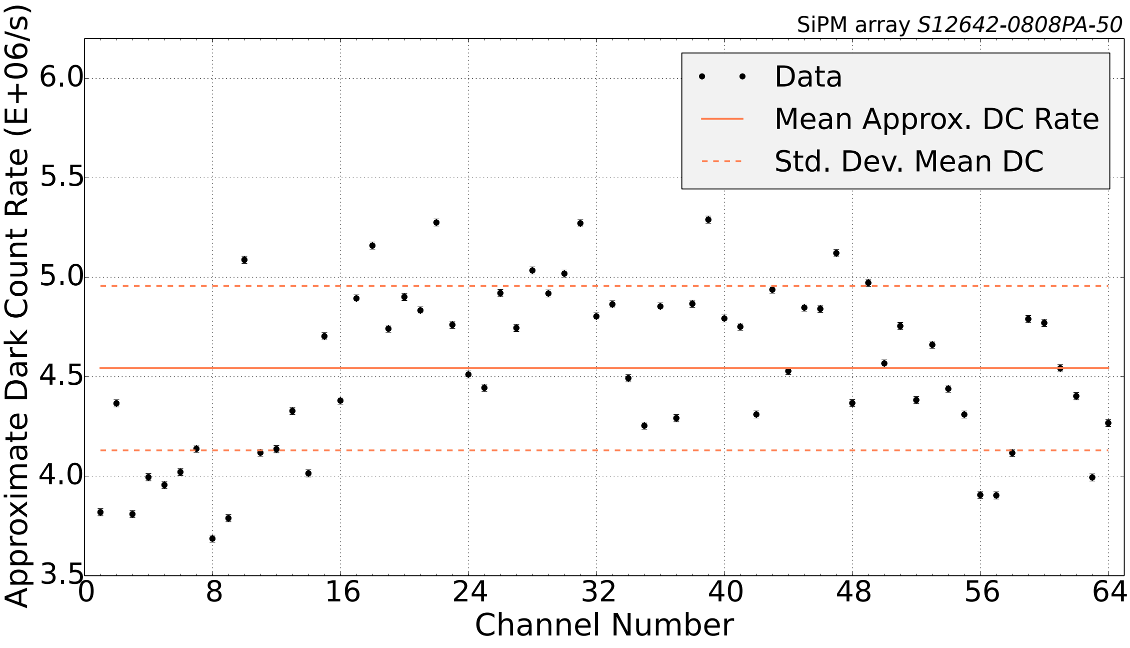

Figure 7.5: Approximate dark-count rate measurement for the SiPM array *S12* at a bias voltage of 71.5 V and temperature of 21.3°C. The statistical uncertainty is shown with black error bars.

Comparing the heatmaps of the breakdown voltage and the dark-count rates of array *S13*, a correlation between the breakdown voltage and the dark-count rate is visible as expected: Channels with a lower breakdown voltage have a higher dark-count rate than channels with a higher breakdown voltage as it is expected since every channel was biased with the same voltage so that the over-voltage is higher for a lower breakdown voltage.
Regarding the heatmaps of array *S12*, no correlation of the breakdown voltage and the dark-count rate is visible. The missing correlation might come from a too high bias voltage of 71.5 V in the dark-count rate measurement. With 71.5 V the bias voltage is 1.5 V over the measured average approximate breakdown voltage which itself is an overestimation of the real breakdown voltage. For the precise measurements of array *S12* with the QADC, a bias voltage of 67.6 V was chosen.

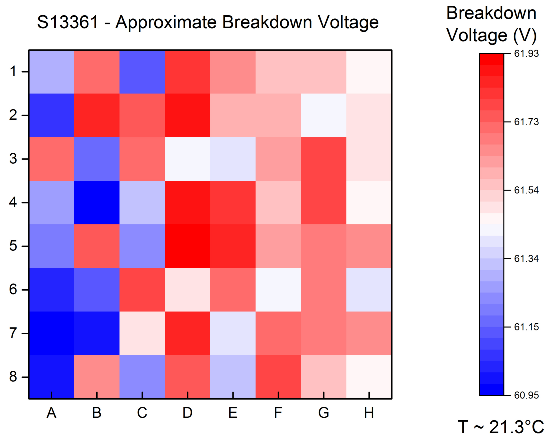

Figure 7.6: Heatmap of the approximate breakdown voltage of array *S13* at a temperature of around 21.3°C.

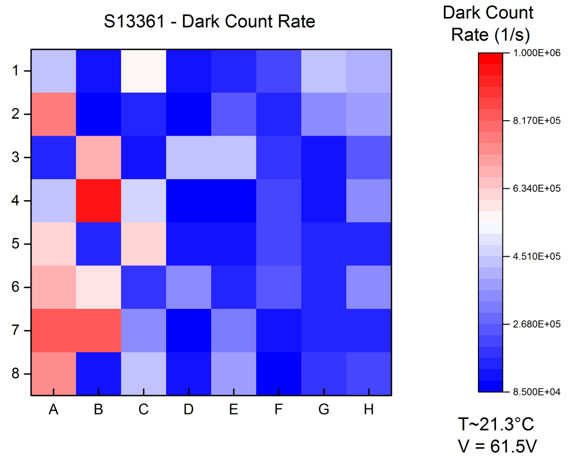

Figure 7.7: Heatmap of the approximate dark-count rate of array *S13* at a temperature of around 21.3°C and a bias voltage of 61.5 V.

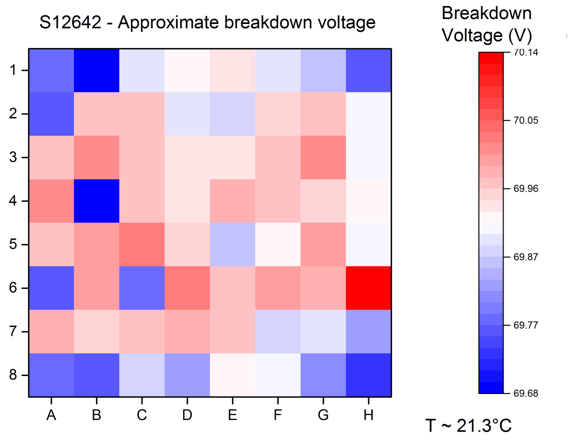

Figure 7.8: Heatmap of the approximate breakdown voltage of array *S12* at a measuring temperature of 21.3°C.

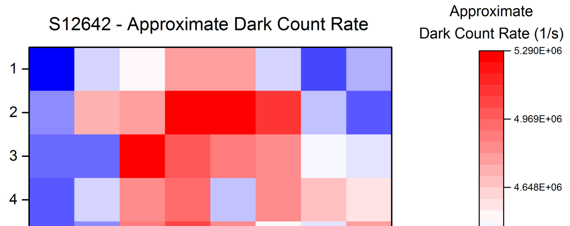

SILICONE RESIN SIPM ARRAY

Compared to the first initial functionality tests of the SiPM arrays and the read-out board above, measurements with the Queued Analog-to-Digital Converter (QADC) give more precise information about the breakdown voltage and the dark-count rate. Furthermore, information about the gain, the Photo Detection Efficiency (PDE), the wavelength sensitivity and the dynamic of the response of a SiPM channel are accessible. During all the following measurements pulsed light with a frequency of 1 kHz and a pulse width of 50 ns was used. Except the wavelength sensitivity measurement, all measurements were made with the LED array 4 ($\lambda = (423 \pm 8)\,\mathrm{nm}$) which is presented in section 6.1. For information about the calibration of the QADC it is referred to [19, 49].

Measurement day	Measurement time	R $(\cdot 10^{-6})$	Std. Dev. $(\cdot 10^{-8})$
12.04.	10:06	4.55	25
12.04.	14:16	4.48	50
12.04.	18:14	4.56	37
13.04.	14:54	4.40	30
13.04.	18:20	4.55	36
14.04.	09:15	4.58	27
14.04.	13:13	4.56	34
15.04.	09:19	4.61	26
15.04.	12:27	4.60	25
18.04.	08:46	4.59	21
18.04.	13:11	4.59	31
18.04.	17:17	4.62	24
19.04.	09:17	4.63	0
19.04.	14:02	4.62	21
19.04.	17:49	4.58	34
20.04.	08:35	4.60	25

Table 7.1: Collimator ratio measurements during the *S13* array measurement with the QADC. Shown are the measurement day, the time of the collimator ratio measurement, the measured collimator rate and the standard deviation of the particular collimator ratio measurement.

Breakdown voltage, gain, PDE, dark-count rate and crosstalk probability

A measurement cycle to obtain information about the breakdown voltage, the gain, the PDE, the dark-count rate and the crosstalk probability for one channel of a SiPM array lasts about 23 minutes. The measurement of the whole array with 64 channels took about 38 hours. The collimator ratio R, which is needed to calculate the incoming photons on the SiPM, was measured in the beginning and in the end of every measurement day. The results for the collimator ratio measurements are shown in table 7.1. The collimator ratio is expected to be stable during the measurement because the used wavelength stayed identical and the temperature fluctuations were small with respect to changes of the shape of the collimator because of heating up or cooling down. For this reason, the average collimator ratio was used for the calculation of the incoming photons. Two measured collimator ratios ($4.40 \cdot 10^{-6}$ and $4.48 \cdot 10^{-6}$) are to small compared to the mean value. In this measurement the second photo diode after the collimator maybe was positioned too far away from the collimator exit. These two measurements were neglected for the calculation of the average collimator ratio. The average collimator ratio is $4.587 \cdot 10^{-6}$ with a deviation of $\pm 0.025 \cdot 10^{-6}$ which is a sufficient result. Figure 7.10 shows the measured collimator ratios and the calculated average collimator ratio.

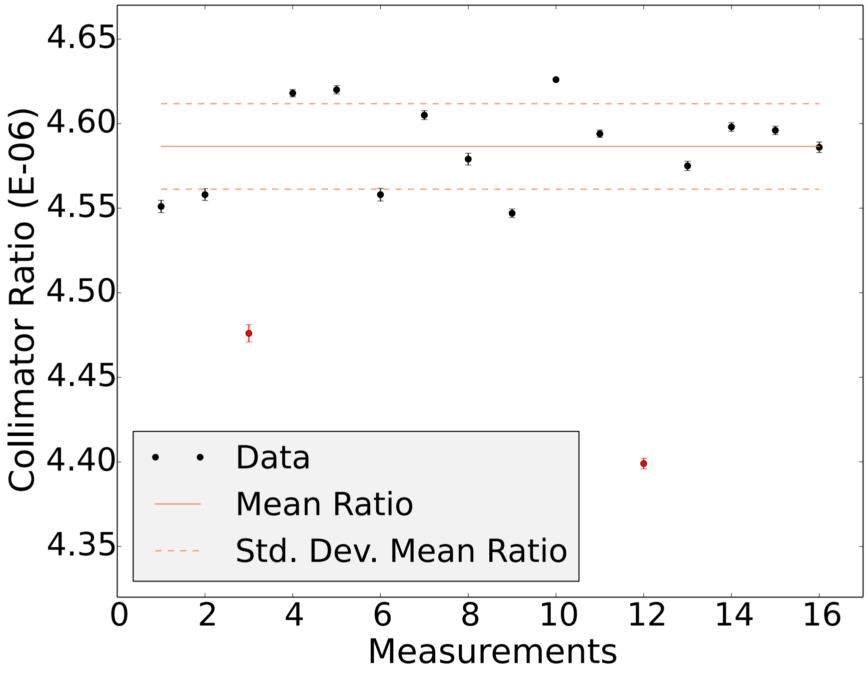

Figure 7.10: Collimator ratio measurements during the *S13* array QADC measurement. The measurements 3 and 12 were not taken into account for the average collimator ratio calculation.

The temperature in SPOCK changed during the day from 18.5°C at measurement begin to around 20.5°C at the usual measurement end. For the following results the temperature is assumed to $(19.5 \pm 1)°\text{C}$. Within this temperature range of 2°C, an influence of the variable temperature on the measurement results can not be excluded but is expected to be small compared to the uncertainties of the measurements. The optical power of the LED was monitored and recorded during the measurement for every channel. The optical power was not changed during the measurement of the array and moved in a region of $180\,\text{p}W$ to $250\,\text{p}W$ due to changes of the output power of the LDD[1] during operation. This equals around 2 photons per puls. The calculations were made with the exact optical power recorded during the measurement.
During the measurement, the SiPM channel D1 (channel number 25) , G5 (channel number 53) and H2 (channel number 58) could not be read out. A reason for this might be the Samtec connector sockets on the SiPM read-out board Rev. 1 which maybe wore out after many plug in and outs of different SiPM arrays. A second improved read-out board could not be assembled during this thesis.

BREAKDOWN VOLTAGE The breakdown voltage for one channel was investigated in more details by taking finger spectra at different bias voltages V_{bias}, calculating the gain $G_{channel}$ of each finger spectrum and extrapolating the linear gain vs. voltage behaviour to a gain factor of zero as explained in section 4.5. The voltage at which the SiPM just starts to be able to amplify generated photo electrons is the breakdown voltage of the SiPM. The gain is kept in units of QADC channels and is not transferred to the real amplification factor to avoid additional errors coming from this transformation. The bias voltage of the SiPM array started at $55.0\,\text{V}$ and was increased in $0.1\,\text{V}$ steps for 14 times. One finger spectrum was recorded for every bias voltage. Every finger spectrum contains 15,000 QADC values. The chosen set of 15 finger spectra at different bias voltages and 15,000 QADC values per finger spectrum is a compromise between an exact result and measurement time. As an example, figure 7.11 shows a breakdown voltage measurement of channel B4.

---

[1] Light Diode Driver

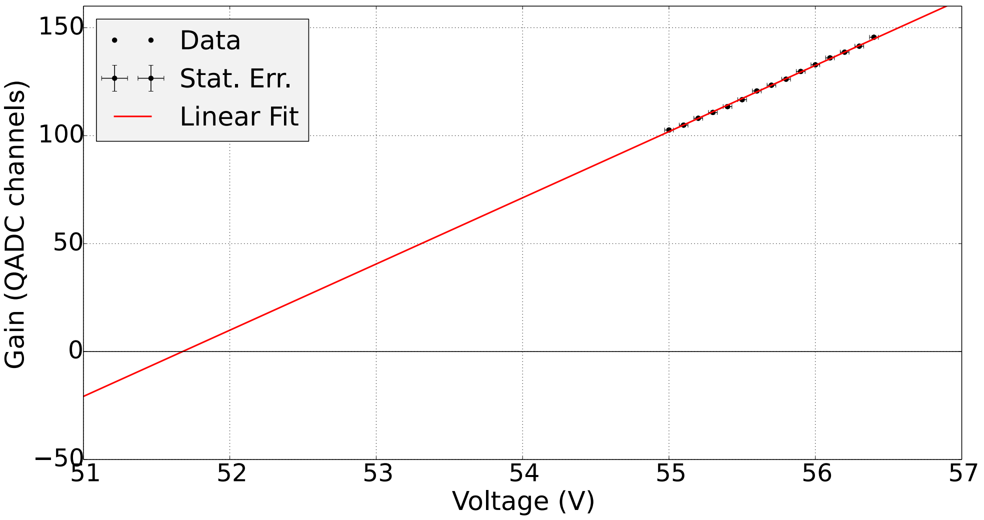

Figure 7.11: Example of a breakdown voltage measurement. The breakdown voltage is defined as the crosspoint of the linear fit with the zero line. This measurement was made with channel B4 of the SiPM array *S13*.

The breakdown voltage of the channel is the voltage for which the gain becomes zero. Graphically, the breakdown voltage is the voltage for which the linear fit of the voltage vs. gain values, shown as a solid line in fig. 7.11, hits the zero line. Figure 7.12 shows the results of the breakdown voltage measurement for every channel.
The average breakdown voltage is

$$(51.65 \pm 0.12\,)V \tag{7.7}$$

at a mean measurement temperature of $19.5°C$. This result is in accordance with the breakdown voltage value of $(53 \pm 5)V$ at $25°C$ the manufacturer claims in the data sheet of the SiPM array *S13*. A comparison of the datasheet values and the results of this measurements will be given in more detail in section 7.4.1.

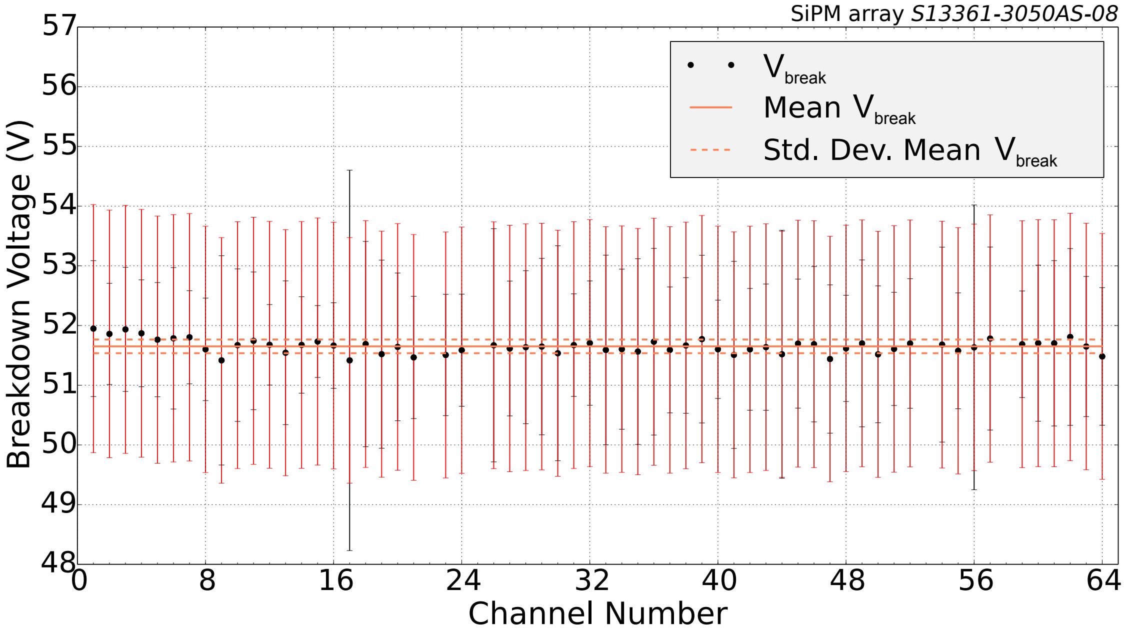

Figure 7.12: Breakdown voltage of the SiPM array *S13* at a temperature of $(19.5 \pm 1)^{\circ}$C. The systematic and statistical uncertainties are shown with red and black error bars, respectively.

Compared to the first approximation of the breakdown voltage with an average value of 61.52 V shown in figure 7.2, the exact results for the breakdown voltage with an average value of (51.65 ± 0.12) V is significantly smaller. This is not surprising, since the method to evaluate the approximate breakdown voltage leads systematically to an overestimation of the breakdown voltage (see section 4.5).

GAIN The gain of every channel was measured by recording a finger spectrum containing 70,029 QADC values at a fixed bias voltage and measuring the distance of the pedestal, the first p.e. peak and the second p.e. peak to each other like it is explained in section 4.5.
In figure 7.13 a recorded finger spectrum is shown as an example. The presented finger spectrum belongs to the gain and PDE measurement of channel B4. The measured data is plotted as a blue line. Also the smoothed data, summing up 5 recorded data points and taking the mean value as well as the Gaussian fits are included in the plot. Peaks till to the third p.e. peak are clearly visible. One more finger spectrum peak is guessable but is not sufficiently build to work with.

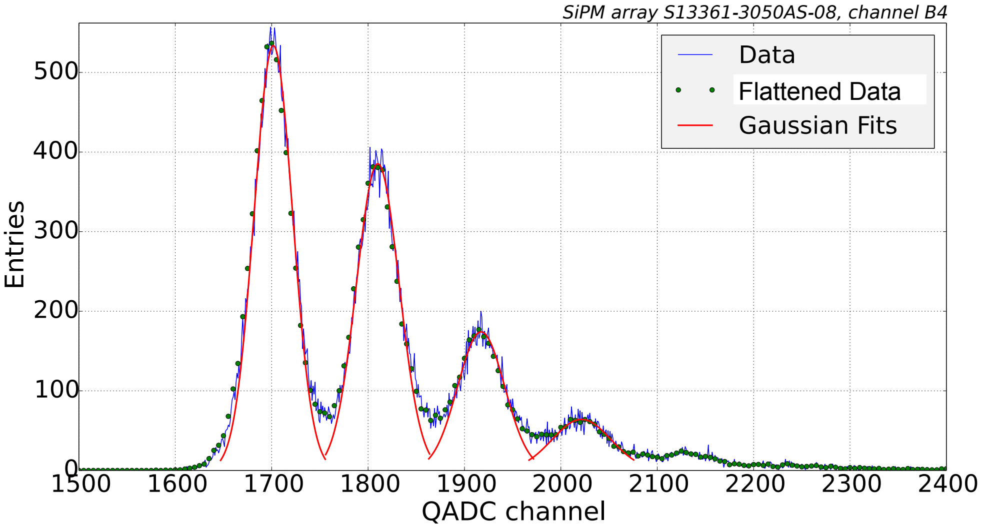

Figure 7.13: Example of a measured finger spectrum of channel B4 of the SiPM array *S13*.

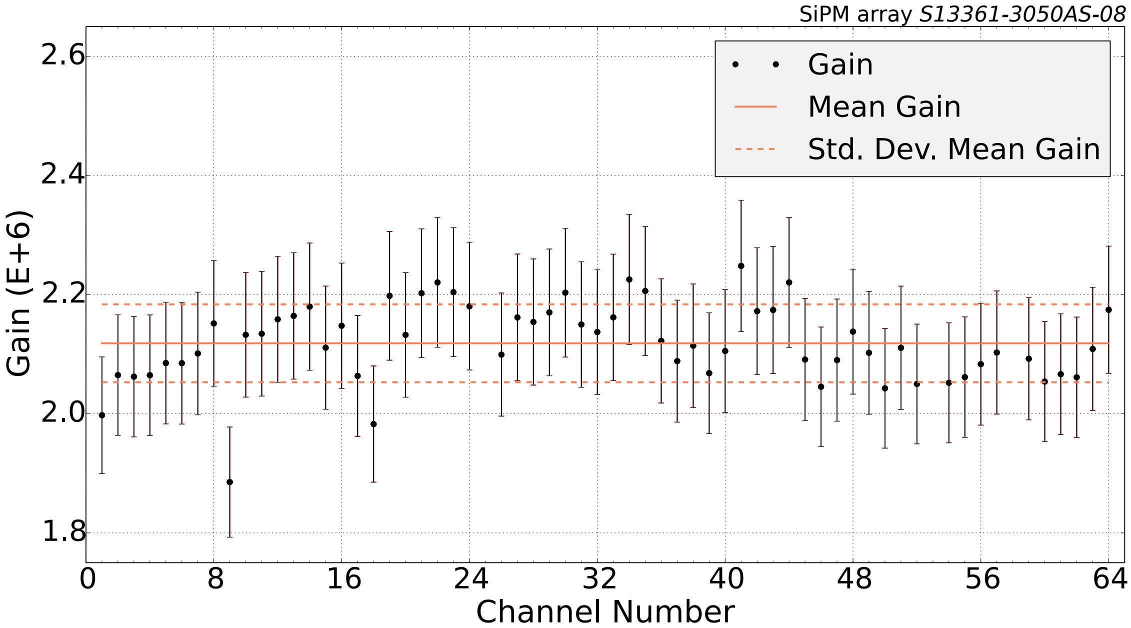

Figure 7.14: Gain of SiPM array *S13* at a temperature of 19.5°C and a bias voltage of 55.2 V. The incident light had a wavelength of 423 nm. The systematic and statistical uncertainties are shown with red and black error bars, respectively.

The obtained gain value $G_{channel}$ is given in units of QADC channels and has to be transformed to the real amplification factor G by using equation 4.12

$$G = \frac{G_{channel} \cdot k}{A \cdot e}$$

where G and $G_{channel}$ are the amplification factors in QADC channels and real units respectively, k is the transformation factor for transforming QADC channel into charge, A is the amplification factor of the SiPM signal and e the elementary charge.
The gain was measured at a voltage of 55.2 V for every channel. A constant voltage instead of an individual voltage for every channel was chosen to be able to compare the channels and make statements about the uniformity over the whole array. In figure 7.14 the results of the gain measurement are shown. The gain is presented in units of 10^6 for each measured channel. The gain varies between $1.8 \cdot 10^6$ and $2.3 \cdot 10^6$ with an average value of

$$G = (2.12 \pm 0.07) \cdot 10^6. \tag{7.8}$$

This measured average gain value is slightly higher than the gain value stated by the manufacturer of $1.70 \cdot 10^6$. Due to a higher over-voltage used in the measurements than recommended by Hamamatsu, an increase of the gain is expected. For a more detailed comparison of the measurement results and the manufacturers information it is referred to section 7.4.1.

PHOTO DETECTION EFFICIENCY (PDE) For calculating the PDE a finger spectrum and a dark spectrum is needed as explained in section 4.5. The PDE is the ratio of detected photons N_{pe} and incoming photons N:

$$PDE = \frac{N_{pe}}{N}. \tag{7.9}$$

The number of incoming photons is evaluated with equation 4.23

$$N = \frac{P \cdot R \cdot \lambda}{h \cdot e \cdot f} \tag{7.10}$$

where P is the optical power monitored during the measurement, R is the collimator ratio already mentioned, λ is the used wavelength, f is the pulsed light frequency of 1 kHz and h and e are the Planck constant and the elementary charge. The number of detected photons is calculated according to equation 4.36 just with the pedestal events of the two measurements with and without light N_{ped} and N_{ped}^{dark} and the total number of events N_{tot}, meaning the total number of QADC measurements, which were 70,029 events for every finger spectrum:

$$N_{pe} = \ln\left(\frac{N_{ped}^{dark}}{N_{tot}}\right) - \ln\left(\frac{N_{ped}}{N_{tot}}\right). \tag{7.11}$$

The number of pedestal events with and without light are directly obtained by the Gaussian fits of the pedestal peaks for light and dark measurements.
For the PDE measurement the same finger spectra as for the gain measurements were used. The bias voltage of every channel in operation was 55.2V. The dark spectrum was recorded right after recording the finger spectrum. As an example, Figure 7.15 shows a dark spectrum of the measurement of channel B4 of the SiPM array *S13*. The measured QADC values are again connected, the Gaussian fit of the pedestal peak is plotted as a solid line. Since this is a dark measurement only the pedestal peak is visible. Dark counts, crosstalk and noise phenomena wash-out and 'stretch' the Gaussian distributed pedestal peak events to higher QADC channel values. With around 64,500 events under the Gaussian fit curve, the very most of the 70,029 recorded events lie in the pedestal peak.

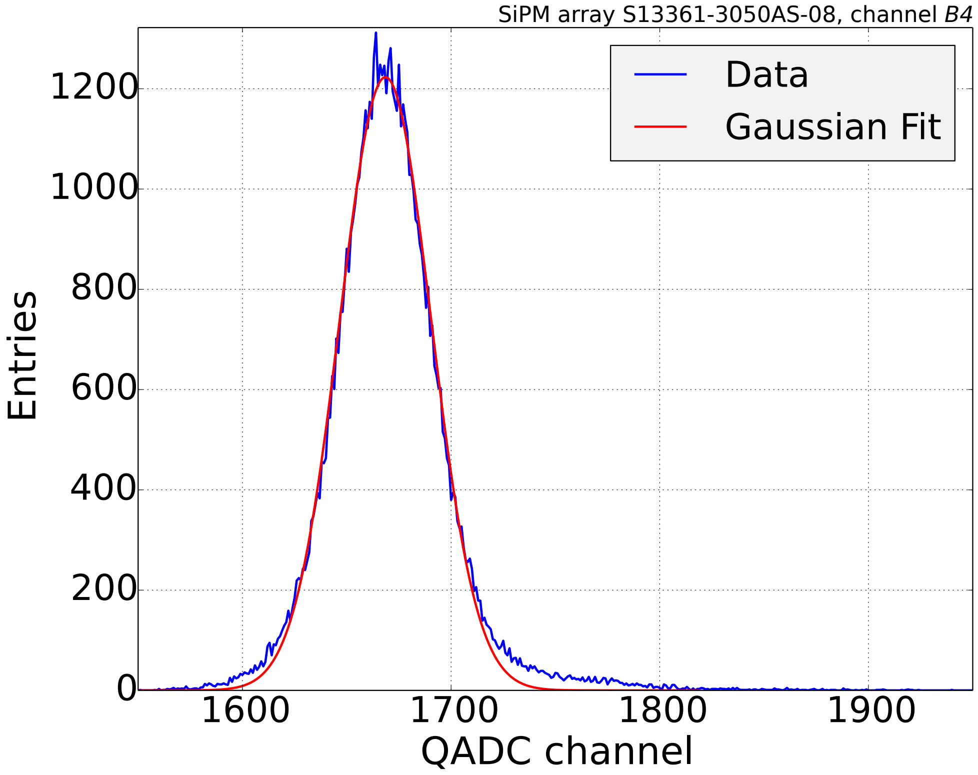

Figure 7.15: Example of a dark spectrum recorded with channel B4 of the SiPM array *S13*.

With equations 4.23 and 4.36 the PDE for ever channel can be calculated as the ratio of N and N_{pe}.

In figure 7.16 the results of the PDE measurement are shown. The average Photo Detection Efficiency over the whole array is

$$\mathrm{PDE} = (44.60 \pm 1.78)\,\%. \tag{7.12}$$

The manufacturer predicts a PDE of 40% at a wavelength of 450 nm and a temperature of 25°C. The measured result for the PDE is about 5 percent higher then predicted. A possible reason for this might be the higher over-voltage with which the channels were operated in these measurements compared to the over-voltage the data sheet recommends. Because of a high noise pollution of the SiPM signal especially by the LED, the over-voltage was chosen to be able to reduce the optical power as much as possible. For this reason the recommended over-voltage was disregarded. More information and a more detailed comparison with the manufacturers information will be given in section 7.4.1.

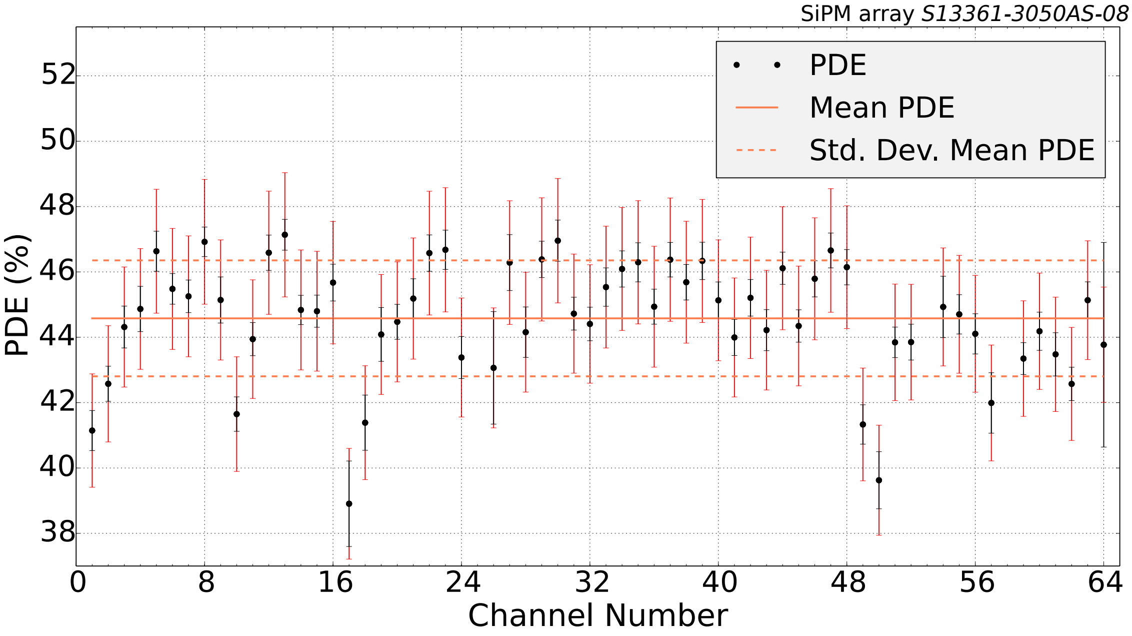

Figure 7.16: Photo Detection Efficiency (PDE) of the SiPM array *S13* at a temperature of 19.5°C and a bias voltage of 55.2 V. The incident light had a wavelength of 423 nm. The systematic and statistical uncertainties are shown with red and black error bars.

DARK-COUNT RATE According to section 4.5 the dark-count rate can be derived with a dark spectrum and the knowledge of the gain of the measured channel. For an ideal SiPM the dark spectrum would just be the pedestal peak with a perfect Gaussian form. Due to dark-counts and crosstalk, events in the region of the first and second p.e. peak are added to this. As definition, all events in the dark spectrum in the area of the first and second p.e. peak plus and minus half of the gain are seen as dark-counts.

Figure 7.17 shows this graphically: The dark spectrum, again of channel B4, is plotted and the area around the first and second p.e. peak, in which the dark-counts are expected, is shaded. To transform the number of dark-counts $\#\xi$ into a dark-count rate ξ, the number of dark-counts has to be divided by the total number of events N_{tot} times the time the QADC measured for one event, which gives together the total time in which the QADC measured during the dark spectrum measurement. According to equation 4.46 this is

$$\xi = \frac{\#\xi}{N_{tot} \cdot (t_{gate} - 15ns)} \tag{7.13}$$

where t_{gate} is the gate time of the QADC which was in every measurement $73\,ns$. Due to an activation time of $15\,ns$, the QADC does not measure right after the gate started. This activation time is subtracted from the gate time.

Figure 7.18 shows the results of the dark-count rate estimation at a mean temperature of 19.5°C and a bias voltage of 55.2 V. The dark-count rate is distributed between $5 \cdot 10^5$ Hz and $1 \cdot 10^6$ Hz with an average value of

$$\xi = (6.76 \pm 1.12) \cdot 10^5 \text{ Hz}. \tag{7.14}$$

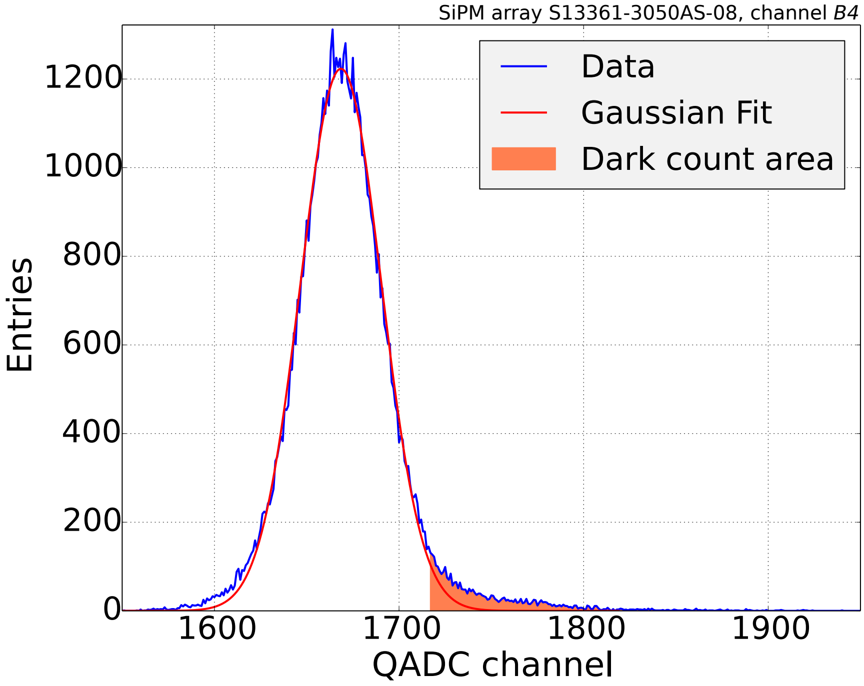

Figure 7.17: Dark-count area in a dark spectrum of a SiPM. The area of ± 1/2 Gain around the first and second p.e. peak, in which all events are assumed as dark-counts, is shaped in the plot.

Compared to the first approximation of the dark-count rate shown in figure 7.4 the dark-count rate increased from $3.124 \cdot 10^5$ Hz to $6.5 \cdot 10^5$ Hz in this more precise measurement. Since the method for finding the approximate dark-count rate via searching for signal peaks is more sensitive to afterpulsing, a decrease of the dark-count rate in the precise measurement is expected. The measured opposite case might come from a to carefully adjusted peakfinding algorithm in the approximate dark-count rate measurement with which not all signal peaks peaks were detected. The measured precise result is comparable to the dark-count rate the manufacturer claims as 0.5 to 1.5 MHz at a temperature of 25°C and bias voltage of circa 56 V.

CROSSTALK PROBABILITY Like it is described in section 4.5 the crosstalk probability ϵ can be investigated with a SiPM dark spectrum. Dark-count events can generate a crosstalk event which results in a two p.e. signal instead an one p.e. signal of a usual dark-count event. The number of crosstalk events $\#\epsilon$ is determined by summing up all events in the dark spectrum at the second p.e. peak within a range of half of the gain. According to equation 4.49 the crosstalk probability is calculated as

$$\epsilon = \frac{\#\epsilon}{\#\xi}. \tag{7.15}$$

with the number of dark-count events $\#\xi$ which has been investigated in the former section. Figure 7.19 shows the results of the crosstalk probability measurement.

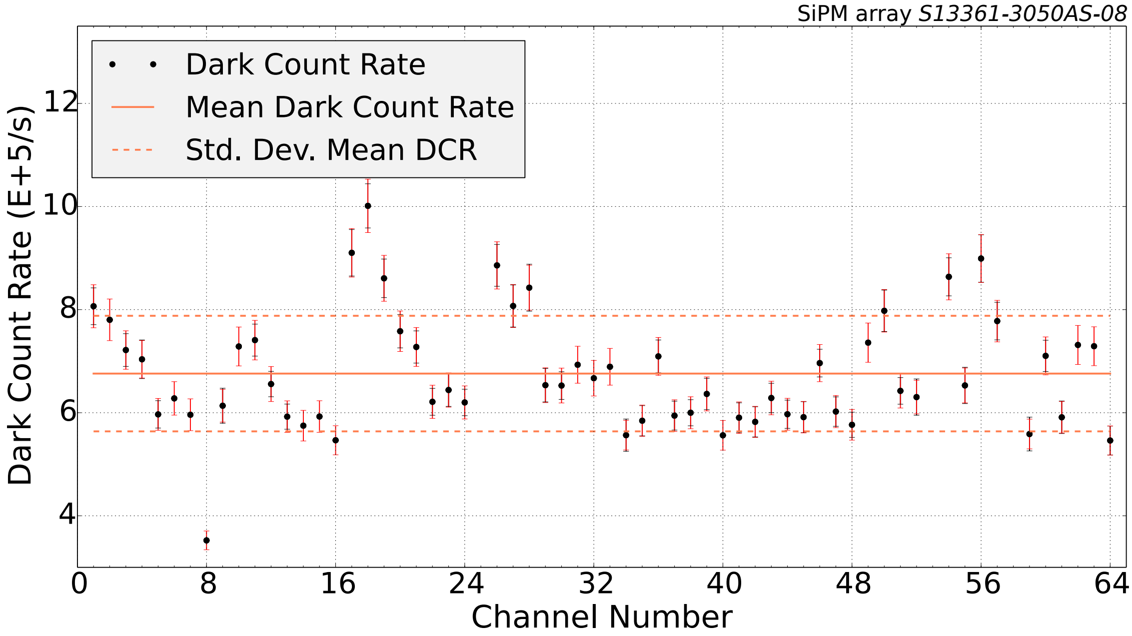

Figure 7.18: Dark-count rate of the SiPM array *S13* at a temperature of 19.5°C and a bias voltage of 55.2 V. The systematic and statistical uncertainties are shown with red and black error bars. The dark-count rate is shown in units of 10^5/s.

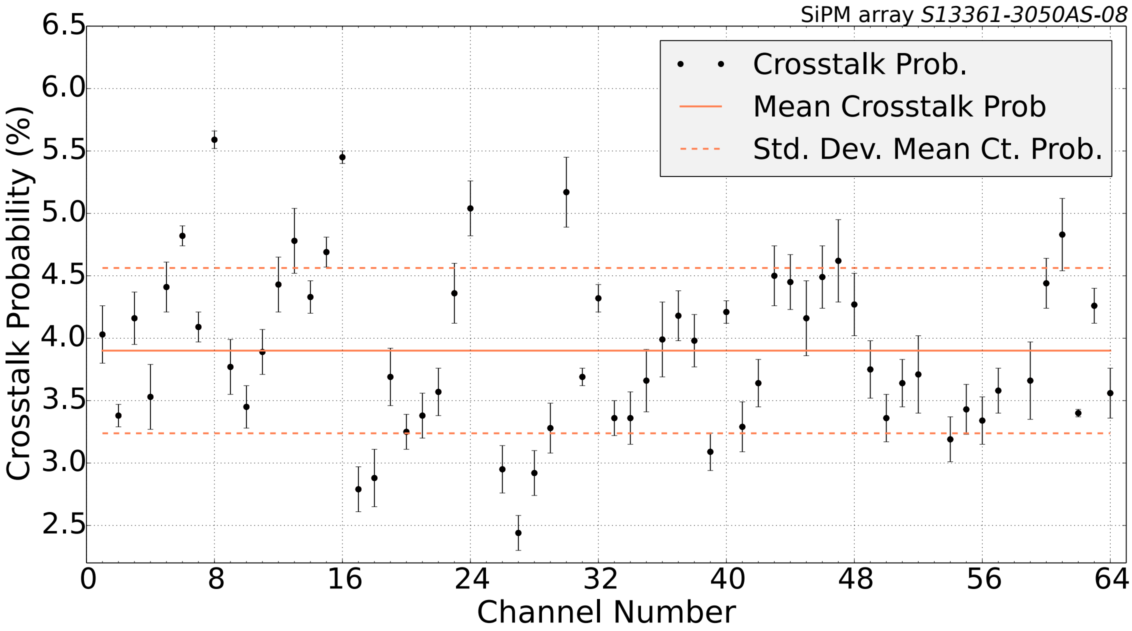

Figure 7.19: Crosstalk probability of the SiPM array *S13* at a temperature of 19.5°C and a bias voltage of 55.2 V . The systematic and statistical uncertainties are shown with red and black error bars.

The average value of the crosstalk probability ϵ over all the measured channels of the SiPM array *S13* results to

$$\epsilon = (3.9 \pm 0.66)\%. \tag{7.16}$$

This results confirms the prediction of the manufacturer of a significantly reduced crosstalk probability compared to former SiPM series. For a comparison of the results of the two measured SiPM arrays and a comparison of this result with the manufacturers information, it is referred to section 7.4.

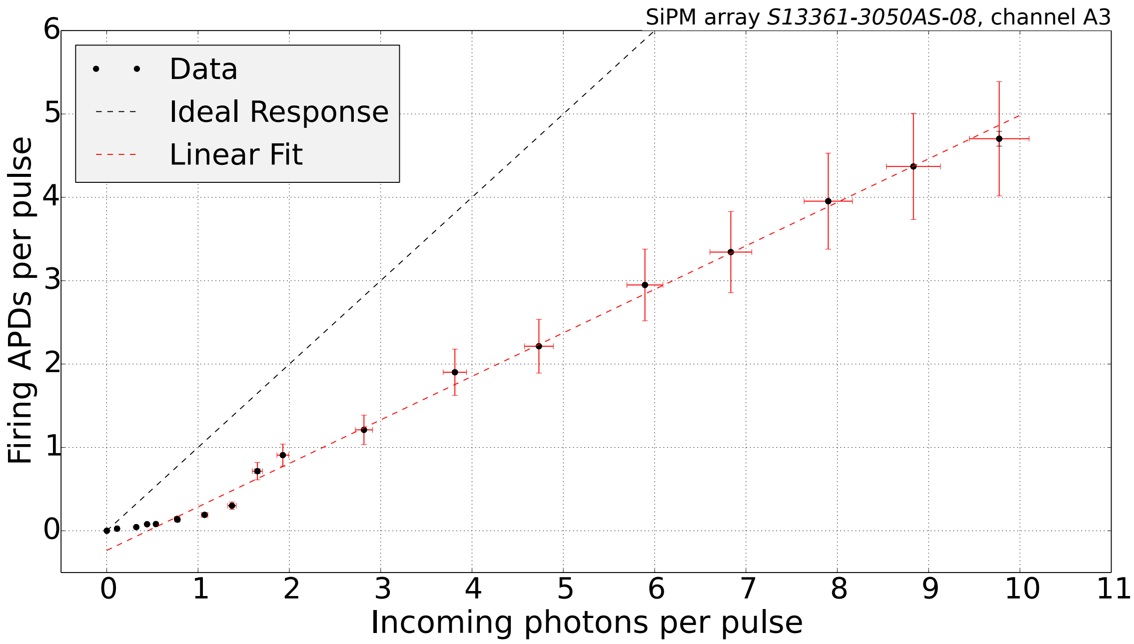

Figure 7.20: Response behaviour of SiPM channel A3 at a bias voltage of 55.2V and at a temperature of 19.5°C. The incident light had a wavelength of 423 nm. The systematic and statistical uncertainties are shown with red and black error bars. The dotted black line symbolizes the ideal response behaviour meaning one firing S-APD per incoming photon.

Response behaviour of the SiPM

The behaviour of the SiPM response is investigated by measuring how many Silicon Avalanche Photo Diodes (S-APDs) fire when a certain amount of photons hit the channel. Like described in section 4.5, this is done by recording finger spectra at different incoming light intensities. Each finger spectrum recorded to investigate the response behaviour contained 50,000 QADC values. To calculate the number of fired S-APDs, the median of each finger spectrum is searched and then divided by the gain of the channel investigated before. According to equation 4.52 this is

$$\#\mathrm{APD}_{\mathrm{fired}} = \frac{x_{\mathrm{med}}}{G_{\mathrm{channel}}}. \tag{7.17}$$

Because both, the median of the SiPM spectrum and the gain, are in units of QADC channel, a transformation into a real charge is not necessary. This also avoids the additional error coming from this transformation. To calculate the number of incoming photons, equation 4.23 was used.
Finding the median of the recorded spectrum is possible for every number of incoming photons. For the gain, the value already found by analysing the finger spectrum was used since the bias voltage of the SiPM of 55.2 V was the same in both measure-

ments. The measurement was made for the channel A3 of SiPM array *S13*. The gain of channel A3 in units of QADC channels was measured as $102.98 \pm 0.38_{stat} \pm 0.02_{sys}$.

Array	Wavelength λ	Systematic uncertainty Δλ
1	371 nm	6 nm
2	376 nm	5 nm
3	395 nm	7 nm
4	423 nm	8 nm

Table 7.2: Table of available LED arrays for measuring the wavelength sensitivity of a SiPM channel

Figure 7.20 shows the results of the investigation of the response behaviour of channel A3. The number of firing S-APDs with respect to the number of incoming photons N is plotted together with a symbolic ideal SiPM response of one firing S-APD per incoming photon and a linear fit of the response behaviour above one incoming photon per pulse. The fit results are

$$\#APD_{fired} = (0.52 \pm 0.01) \cdot N - (0.24 \pm 0.06). \tag{7.18}$$

The ideal linear response behaviour of a SiPM would have an inclination of 1. Since the photo detection efficiency of a SiPM is not 100%, which means that not every photon is detected, an inclination less then 1 is expected. The result of the inclination in figure 7.18 is in agreement to the PDE measurement. A higher inclination of the fit than the measured PDE is expected, since the method for finding the number of fired S-APDs is sensitive to dark counts and crosstalk events. Down to less than one photon per pulse the linear behaviour breaks and the inclination of the response behaviour decreases. A firm explanation for this behaviour has not been found during this thesis. Since the break of the linear behaviour seems to be for less then one photon per pulse, a suggestion is that this behaviour has its origin in the number of recorded QADC values. Due to the low frequency of signal events for photon numbers less than one per pulse, the number of 50,000 measured QADC values per measurement might have been to small. A second measurement with a higher number of recorded values to test this these was no more possible during this thesis.

Wavelength sensitivity of the SiPM

The wavelength sensitivity is investigated by measuring the PDE with incoming light of different wavelengths. According to section 6.1 LED arrays with four different wavelengths were available: 423 nm, 395 nm, 376 nm and 371 nm. Table 7.2 gives an overview of the available LED arrays and the systematic uncertainties of the wavelengths. Since the collimator ratio depends on the used wavelength, the collimator ratio was measured before every PDE measurement with a new wavelength. Table 7.3 shows the results of the collimator ratio measurements.

Wavelength λ	Collimator ratio R ($\cdot 10^{-6}$)	Std. Dev. R ($\cdot 10^{-9}$)
371 nm	5.295	4.306
376 nm	5.016	3.467
395 nm	4.729	2.029
423 nm	4.568	7.567

Table 7.3: Table of the measured collimator ratios for every wavelength used with SiPM array *S13*.

Wavelength λ	PDE	Stat. Er. PDE	Sys. Er. PDE
371 nm	27.029 %	0.395 %	1.13 %
376 nm	39.647 %	0.491 %	1.453 %
395 nm	48.908 %	0.656 %	1.816 %
423 nm	46.486 %	1.187 %	1.885 %

Table 7.4: Table of the results of the PDE for every wavelength used in the wavelength sensitivity measurement of SiPM array *S13*. These results are shown graphically in figure 7.21.

For every wavelength a finger spectrum with an optical power of around $200-300\,\mathrm{p}W$ and a dark spectrum was recorded. Both spectra contained 70,029 measured QADC values. The optical power was monitored and recorded during every PDE measurement. The PDE was calculated like it is presented in 4.5.

The wavelength sensitivity was investigated for channel B4 of the SiPM array *S13*. Table 7.4 and figure 7.21 show the results of the PDE measurements regarding the wavelength of the incoming light.

In the range of the four measured wavelengths, the maximal PDE is obtained at a wavelength of 395 nm. For wavelengths lower than 395 nm the PDE decreases. The manufacturer predicts a maximum PDE at a wavelength of around 450nm and a decrease in PDE for shorter wavelengths then this. The range of wavelengths the SiPM is capable to detect is from 270 nm to 900 nm (see fig. 7.33). Since LED arrays with wavelengths longer then 423 nm were not available during the time of this thesis, no statement can be made about the wavelength of maximum sensitivity. The decrease of

PDE going to shorter wavelengths is confirmed with this measurement.

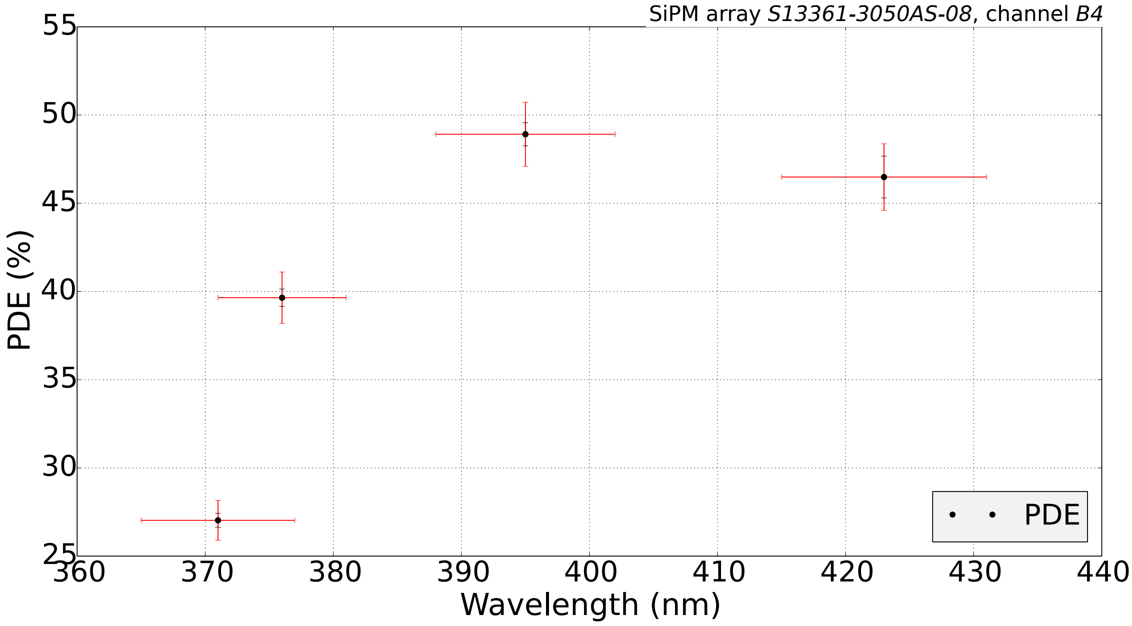

Figure 7.21: PDE at different wavelengths of channel B4 at a bias voltage was 55.2V and at a temperature of 19.5°C. The systematic and statistical uncertainties are shown with red and black error bars. The precise results are given in table 7.4.

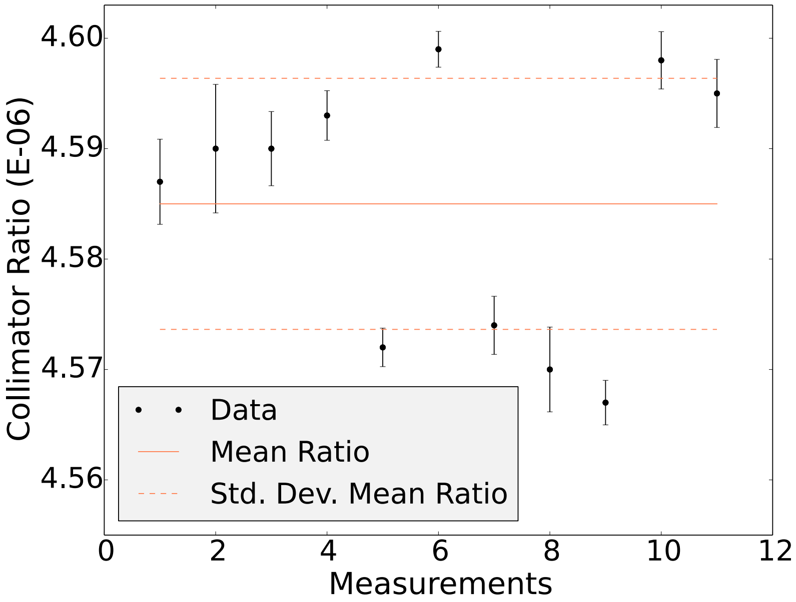

Figure 7.22: Collimator ratio measurements during the *S12* array QADC measurement. The average collimator ratio is calculated to $(4.585 \pm 0.011) \cdot 10^{-6}$, included in the plot.

EPOXY RESIN SIPM ARRAY

The measurements of the characteristics of the SiPM array *S12642-0808PA-50* (*S12*) were made directly after the measurements with the SiPM array *S13*. Since the same measuring methods were used for both arrays, the following presentation of the results for the SiPM array *S12* will be kept short just focusing on the results and a short interpretation. For information about the used measurement methods it is refereed to section 4.5 the previous section 7.2. A scheme of the channel names and numbers can be found in the Appendix section 9.1.

Like for the measurements of the SiPM array *S13*, pulsed light with a frequency of 1 kHz and a pulse width of 50 ns was used for all measurements with light. When nothing else is mentioned, the LED array 4 with a wavelength of 423 nm was used for all light measurements.

In addition to the channels D1 (channel number 25) , G5 (channel number 53) and H2 (channel number 58) which already could not be read out during the measurement of SiPM array *S13*, the channels G4 (channel number 52) and G2 (channel number 50) could not be read out in this consecutive measurement of SiPM array *S12*. This gives hint to a wear out of the Samtec connector sockets on the SiPM read-out board. A second board could not be assembled during this thesis.

Breakdown voltage, gain, PDE, dark-count rate and crosstalk probability

The measurement of the breakdown voltage, the gain, the PDE, the dark-count rate and the crosstalk probability lasted about 34 hours. The collimator ratio was measured at the start and in the end of every measurement day. The results for the collimator ratio measurements are shown in table 7.5.

Measurement Day	Measurement time	R ($\cdot 10^{-6}$)	Std. Dev. R ($\cdot 10^{-8}$)
20.04.16	08:35	4.60	26
20.04.16	16:17	4.59	39
21.04.16	08:34	4.60	16
21.04.16	16:39	4.59	58
22.04.16	10:30	4.59	34
22.04.16	14:00	4.57	20
22.04.16	16:15	4.57	38
25.04.16	08:45	4.59	22
25.04.16	16:42	4.57	17
26.04.16	08:31	4.57	26
26.04.16	12:19	4.60	31

Table 7.5: Collimator ratio measurements during the *S12* array measurement with the QADC. Shown are the measurement day, the time of the collimator ratio measurement, the measured collimator ratio and the standard deviation of the particular collimator ratio measurement

Again, the average collimator ratio was used for all calculations since the collimator ratio is expected to stay constant during the measurement time. The average collimator ratio is calculated as $4.585 \cdot 10^{-6}$ with a deviation of $\pm 0.011 \cdot 10^{-6}$ which is a sufficient result. Figure 7.22 shows the measured collimator ratios and the calculated average collimator ratio with its uncertainty.

Like for the measurements with the SiPM array *S13*, the temperature is assumed to be $(19.5 \pm 1)°\mathrm{C}$. The optical power was not changed during the measurement of the array and varied in a region of $200\,\mathrm{p}W$ to $300\,\mathrm{p}W$. This corresponds to around 2.5 photons hitting the SiPM surface per pulse. The optical power was monitored and recorded during light measurements and calculations are made with this precisely measured optical power.

BREAKDOWN VOLTAGE To obtain the breakdown voltage, 15 finger spectra were recorded starting at a bias voltage of $67.0\,\mathrm{V}$ and increasing it in $0.1\,\mathrm{V}$ steps 14 times to

68.4 V. For every finger spectrum 15,000 data points were recorded with the QADC. Figure 7.23 shows the results of the breakdown voltage measurement for a temperature of 19.5°C. The average breakdown voltage is

$$V_{\mathtt{break}} = (64.62 \pm 0.10)\,V. \tag{7.19}$$

This result is in good accordance with the breakdown voltage value of (65 ± 10) V at 25°C the manufacturer claims in the data sheet of the SiPM array *S12*. A more detailed comparison of the measurement results and the manufacturers information will be given in section 7.4.1.

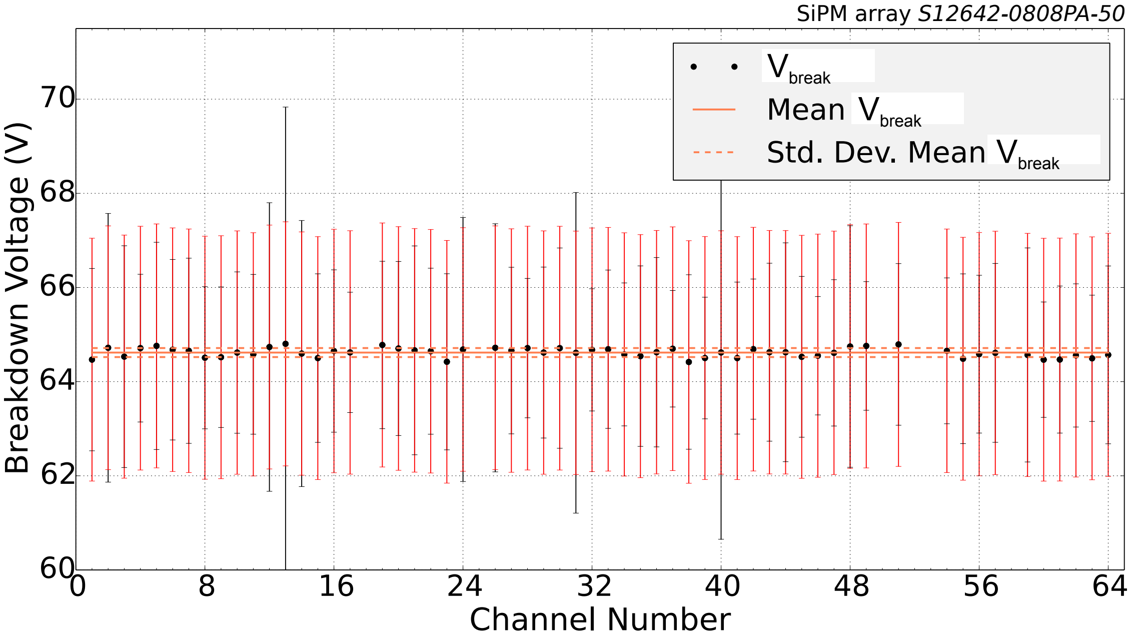

Figure 7.23: Breakdown voltage of the SiPM array *S12* for a temperature of 19.5°C. The systematic and statistical uncertainties are shown with red and black error bars.

GAIN For calculating the gain of the SiPM channels, finger spectra at a bias voltage of 67.6 V have been recorded containing 70,029 data points each. The measured gain in units of QADC channel is then transformed in real units with equation 4.12.

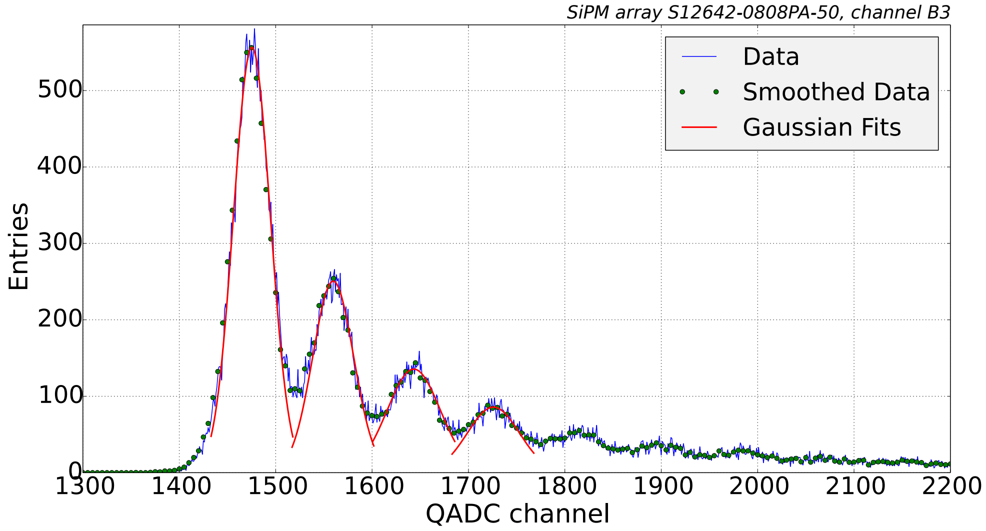

Figure 7.24: Example of a measured finger spectrum of the SiPM array *S12* channel B3.

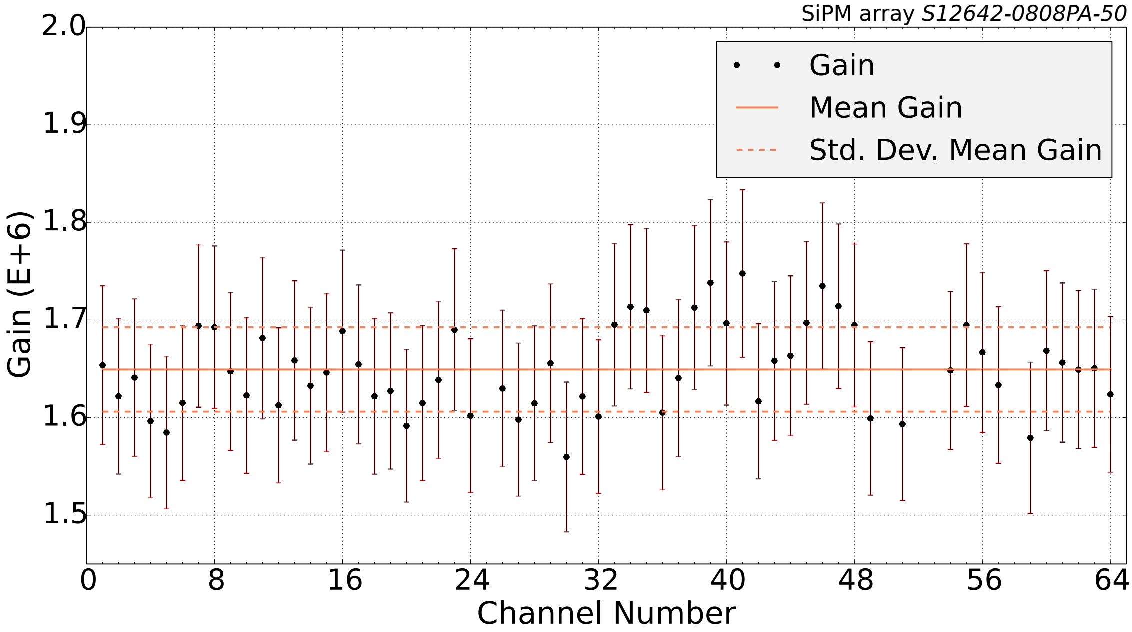

Figure 7.25: Gain of the SiPM array *S12* at a temperature of $(19.5 \pm 1)^\circ\mathrm{C}$ and a bias voltage of $67.6\,\mathrm{V}$. The incident light had a wavelength of $423\,\mathrm{nm}$. The systematic and statistical uncertainties are shown with red and black error bars.

In figure 7.24 a recorded finger spectrum of channel B3 is shown as an example. The measured QADC values are connected with lines. The smoothed data, presenting the mean value of 5 consecutive data points, and the Gaussian fits are included in the plot as points and solid lines. Comparing the two example finger spectra of the arrays *S12* and *S13* shown in figure 7.13, no significant differences are visible. Looking at the areas between the pedestal peak and the first p.e. peak, the finger spectrum of SiPM array *S13* is contaminated with less noise.

In figure 7.25 the results of the gain measurement are shown. The gain varies roughly between $1.5 \cdot 10^6$ and $1.8 \cdot 10^6$ with an average value of

$$G = (1.65 \pm 0.04) \cdot 10^6. \tag{7.20}$$

This is in agreement with the manufacturers information which will be discussed in section 7.4.1.

PHOTO DETECTION EFFICIENCY (PDE) The PDE was calculated with the equations 4.23 and 4.36 for the number of incoming photons N and the number of detected photons N_{pe} by calculating the ratio of these two values. The same finger spectra as for the gain calculation were used. The bias voltage was 67.6 V. The dark spectrum was recorded right after the finger spectrum for every channel.
Figure 7.27 shows an example of a dark spectrum of channel B3 of the SiPM array *S12*. The recorded data is connected with lines and the Gaussian fit is presented as a solid line.

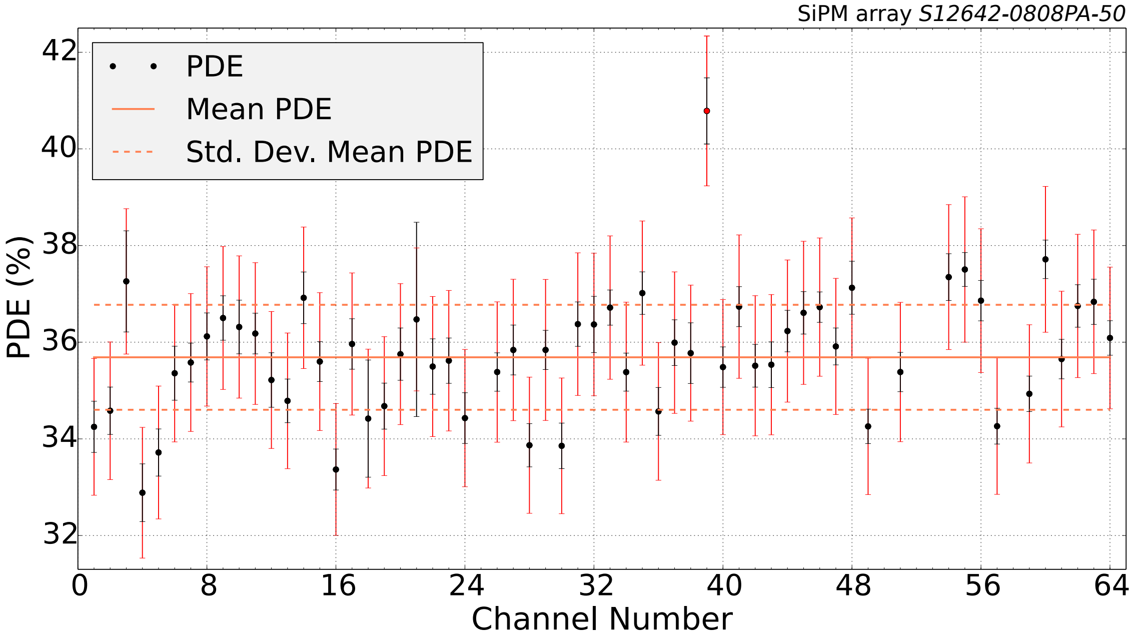

Figure 7.26: PDE of the SiPM array *S12* at a temperature of 19.5°C and a bias voltage of 67.6V. The incident light had a wavelength of 423 nm. The systematic and statistical uncertainties are shown with red and black error bars. For channel E7 (channel number 39) the Gaussian fits failed.

In figure 7.26 the results of the PDE measurement are presented. For channel E7 (channel number 39) the Gaussian fits fails and the channel is excluded from the further calculation. The average photo detection efficiency over the whole array is

$$\mathrm{PDE} = (35.69 \pm 1.09)\,\%. \tag{7.21}$$

This is in good accordance to the PDE value given by the manufacturer of 35 % measured with light of a wavelength of 450 nm and at a temperature of 25°C. A more detailed comparison with the manufacturers information will be given in section 7.4.1.

DARK-COUNT RATE For the number of measured dark counts, the events in the dark spectrum around the first and second p.e. peak position are counted. Figure 7.27 illustrates this for a channel of the SiPM array *S12*. Comparing the dark spectra of the SiPM array *S12* (fig. 7.27) and *13* (fig. 7.17) it is visible, that the new series array *S13* is more noise reduced and has smaller numbers of dark counts and crosstalk events. With equation 4.46 the dark counts are transformed into a dark-count rate.

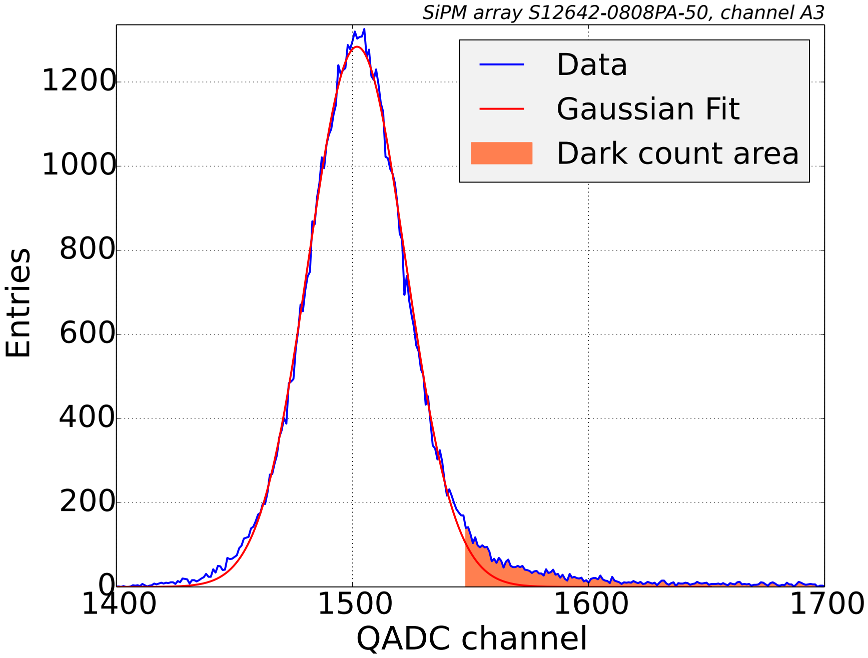

Figure 7.27: Dark spectrum of channel B3 of SiPM array *S12*. The area of ± 1/2 Gain around the first and second p.e. peak, in which all events are assumed as dark-counts, is shaped in the plot.

Figure 7.28 shows the results for the dark-count rates at a mean temperature of 19.5°C. The average dark-count rate results to

$$(1.29 \pm 0.14) \cdot 10^6\ \mathrm{Hz}. \tag{7.22}$$

This is significantly less than the manufacturer predicts for the SiPM array ($2 \cdot 10^6$ Hz). A possible reason for this might be the measurement temperature of 19.5°C which is circa 5.5°C lower than the temperature at which Hamamatsu states the SiPM characteristics (see sec. 7.4.1).

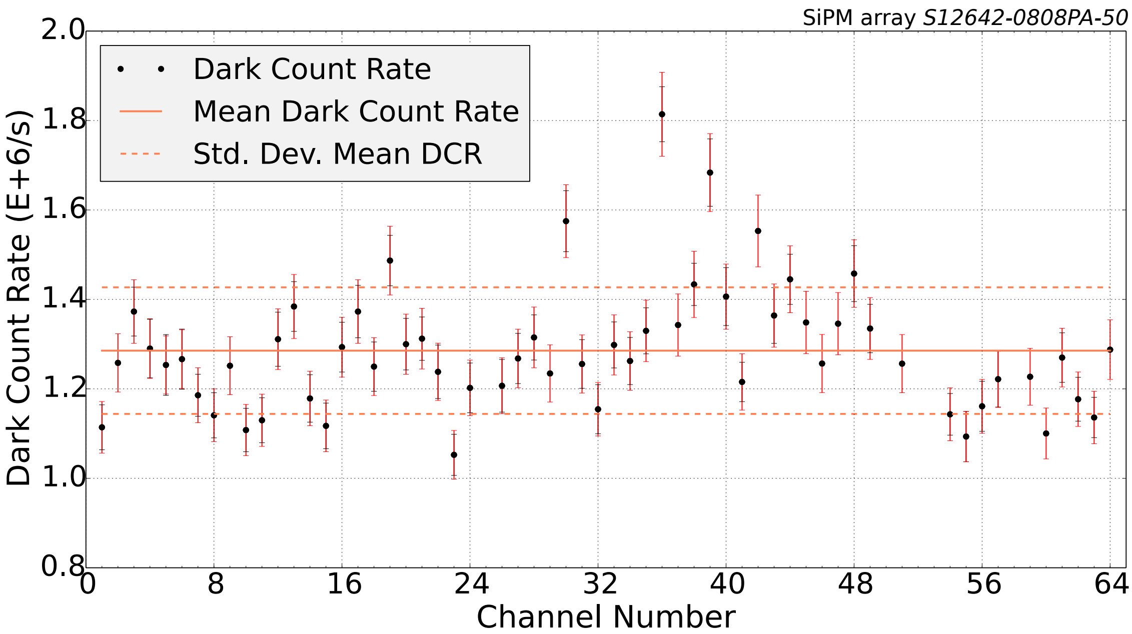

Figure 7.28: Dark-count rate of the SiPM array *S12* at a temperature of 19.5°C and a bias voltage of 67.6V . The dark-count rate is shown in units of 10^6/s. The systematic and statistical uncertainties are shown with red and black error bars.

CROSSTALK PROBABILITY To investigate the crosstalk probability the crosstalk events around the second p.e. peak within a range of half of the gain are counted. The crosstalk probability is the number of crosstalk events divided by the number of dark-count events which was investigated in the former section.

Figure 7.29 shows the results of the crosstalk probability measurement. The average crosstalk probability ϵ is

$$\epsilon = (11.17 \pm 1.27)\%. \tag{7.23}$$

Compared to the average crosstalk probability of array *S13* of $\epsilon = 3.6\%$, this result is considerably higher. For the new series array *S13*, Hamamatsu states to have improved the separation between single S-APDs by deepen the gap between the S-APDs to decrease the crosstalk probability. For a more detailed comparison of the two arrays, it is referred to section 7.4. The manufacturer does not give a prediction of the crosstalk probability for the *S12* SiPM array.

Response behaviour of the SiPM

The response behaviour of the SiPM array *S12* was investigated by finding the median of the finger spectrum at different light intensities for channel B4.

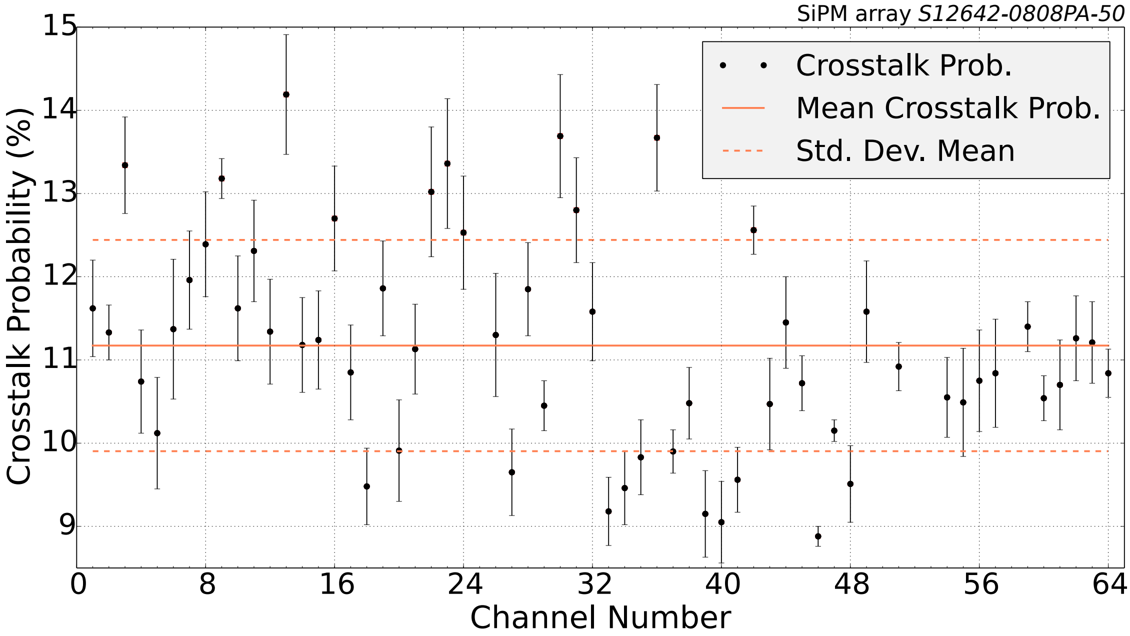

Figure 7.29: Crosstalk probability measurement of the SiPM array *S12* at a temperature of 19.5°C and a bias voltage of 67.6 V. The systematic and statistical uncertainties are shown with red and black error bars.

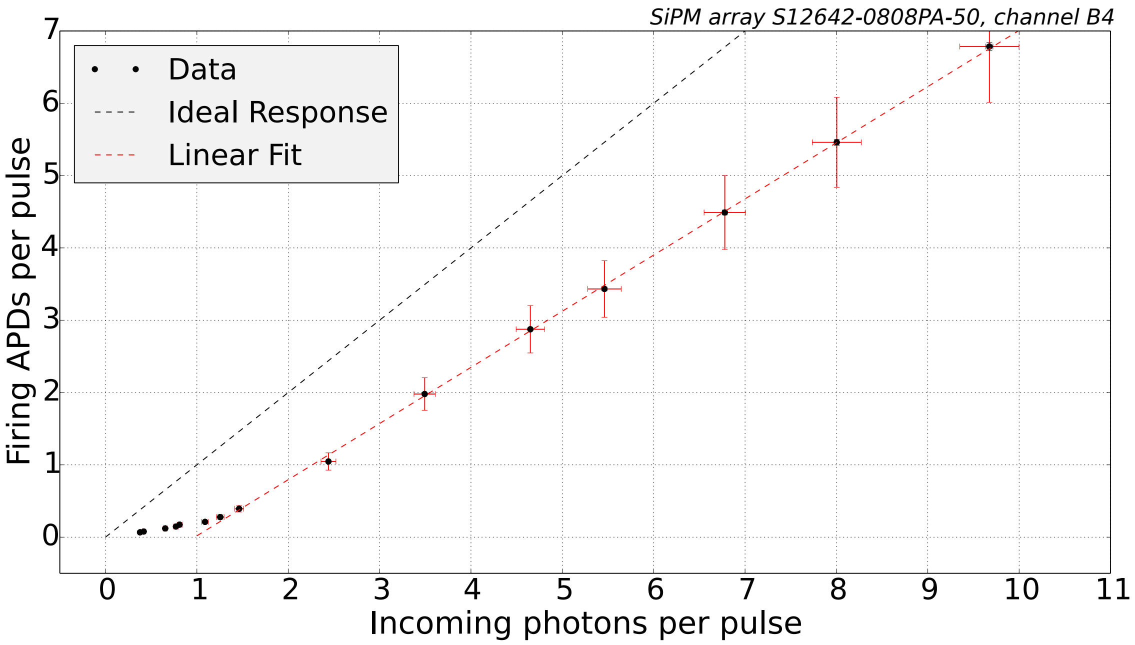

Figure 7.30: Response behaviour of SiPM channel B4 at a temperature of 19.5°C and a bias voltage of 67.6V. The incident light had a wavelength of 423 nm. The dotted black line symbolizes the ideal response behaviour meaning one firing S-APD per incoming photon.

Each finger spectrum contained 50,000 data points. The gain of channel B4 in units of QADC channel was measured as $80.529 \pm 0.57_{\mathrm{stat}} \pm 0.02_{\mathrm{sys}}$. Figure 7.30 shows the results of the investigation of the response behaviour of channel B4. The firing S-APDs per incoming photons per pulse are plotted together with a symbolic ideal SiPM response of one firing S-APD per incoming photon and a linear fit of the response behaviour after around one incoming photon per pulse. The fit results are

$$\#\mathrm{APD}_{\mathrm{fired}} = (0.777 \pm 0.006) \cdot N - (0.758 \pm 0.033). \tag{7.24}$$

The breaking of the linearity of the response of the SiPM was already seen in the data of the SiPM array *S13* and discussed in section 7.2.1. This measurement confirms this behaviour. A suggestion about the decrease of the inclination of the response behaviour for less than one photon is probably a too small chosen number of recorded QADC data points.

For a comparison of this result with the result of SiPM array *S13*, it is referred to the discussion of the measurement results in section 7.4.3.

Wavelength λ	PDE	Stat. Er. PDE	Sys. Er. PDE
371 nm	18.564 %	0.616 %	0.928 %
376 nm	20.851 %	0.292 %	0.906 %
395 nm	36.886 %	0.93 %	1.463 %
423 nm	34.963 %	0.742 %	1.411 %

Table 7.6: Table of the results of the photo detection efficiency for every wavelength used in the wavelength sensitivity measurement of SiPM array *S12*. These results are shown in figure 7.31.

Wavelength sensitivity of the SiPM

The wavelength sensitivity is investigated by measuring the PDE at the wavelengths 423 nm, 395 nm, 376 nm and 371 nm shown in table 7.2 The collimator ratio was measured for every new wavelength before the PDE measurement. The results are presented in table 7.7. The optical power was recorded during the PDE measurements.

Wavelength λ	Collimator ratio R $(\cdot 10^{-6})$	Std. Dev. R $(\cdot 10^{-8})$
371 nm	5.29	47
376 nm	5.05	40
395 nm	4.72	82
423 nm	4.57	76

Table 7.7: Table of the measured collimator ratios for every wavelength used in the wavelength sensitivity measurement of SiPM array *S12*.

Table 7.6 and figure 7.31 show the results of the wavelength sensitivity measurement of channel B4. In the range of the four measured wavelengths, the maximal PDE is obtained at wavelength of 395nm, like it was the case for the SiPM array *S13* too. After this wavelength the PDE decreases fast for shorter wavelengths. The manufacturer predicts a maximum PDE at a wavelength of around 450 nm and a decrease in PDE for shorter wavelengths. The range of wavelengths the SiPM is capable to detect is given from 320 nm to 900 nm. No statements can be made about wavelengths longer then 423nm. The strong decrease of PDE going to shorter wavelengths is confirmed with this measurement. A comparison between the old series SiPM array *S12* and the new *S13* SiPM array will be given in the following section.

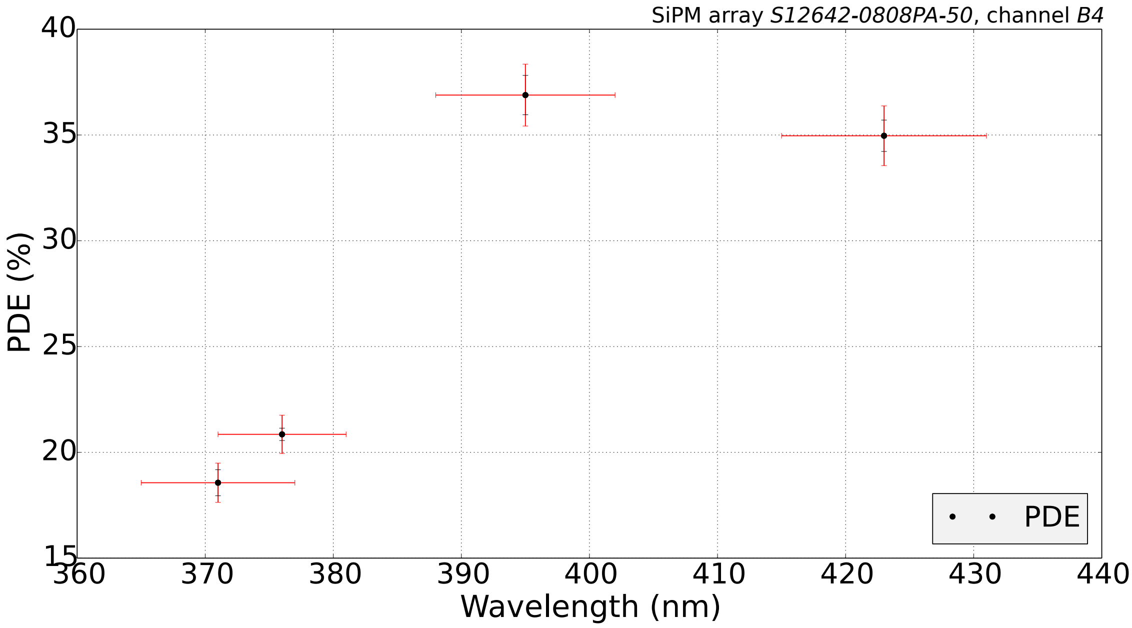

Figure 7.31: PDE at different wavelengths of channel B4 at a temperature of 19.5°C and a bias voltage of 67.6 V. The systematic and statistical uncertainties are shown with red and black error bars. The precise results are given in table 7.6.

COMPARISON OF SIPM ARRAYS *S12* AND *S13*

In this section the measured characteristics of the SiPM array series *S12* (sec. 7.3) and the latest series of SiPM arrays from the manufacturer Hamamatsu *S13* (sec. 7.2) will be compared. This will contribute to the answer of the question whether the new series SiPM have advantages regarding measuring fluorescence light, i.e. to meet the requirements and goals of SiECA.

Breakdown voltage, gain, PDE, dark-count rate and crosstalk probability

Table 7.8 summarises the measured average values for the breakdown voltage, the gain, the PDE, the dark-count rate and the crosstalk probability for both SiPM arrays *S12* and *S13*. Under the prevalent test conditions of a temperature of (19.5 ± 1)°C, a pulsed light source with a frequency of 1 kHz and a wavelength of 423 nm, all four characteristic values of the new series SiPM array *S13* improved compared to the SiPM array *S12*.

The average breakdown voltage decreased in the new SiPM series by about 20% from 64.62 V to 51.65 V. This is seen as an improvement in the sense, that the electrical power consumption of a firing SiPM is reduced compared to a SiPM with the same gain as the SiPM array *S13* but with a breakdown voltage equal to that of the former series

S12. The average Gain increased from $1.65 \cdot 10^6$ to $2.12 \cdot 10^6$, which is an improvement of about 28%. The PDE increased also from 35.69% to 44.6%, equal to an improvement of about 25%. The dark-count rate decreased by 43% from 1.17 MHz to 0.68 MHz. The crosstalk probability decreased by 65% from 11.17% to 3.9%.
One should keep in mind that these results are wavelength specific. Since the two measured SiPM arrays have different resins (section 4.4), the new series of the SiPM arrays with a silicone resin is more sensitive to light with shorter wavelength then the older ones with epoxy resin. This is investigated in the next section. Going to longer wavelengths the degree of advantage of the new SiPM array series might decrease. For the used wavelength of 423 nm the manufacturer predicts no difference of the measured results influenced by the different resins like figure 7.33 shows.

	S12642	S13361	Improvement
Breakdown voltage (V)	64.62 ± 0.10	51.65 ± 0.12	20 %
Gain (E + 06)	1.65 ± 0.04	2.12 ± 0.07	28 %
PDE (%)	35.69 ± 1.09	44.6 ± 1.78	25 %
Dark-count rate (MHz)	1.29 ± 0.14	0.68 ± 0.11	43 %
Crosstalk probability (%)	11.17 ± 1.27	3.9 ± 0.66	65 %

Table 7.8: Summary of the average results of the measured breakdown voltage, gain, PDE and dark-count rate for the SiPM arrays *S12* and *S13*. Column three shows the improvements of the new series SiPM array *S13* compared to the former series SiPM array *S12*

.

COMPARISON WITH THE MANUFACTURERS INFORMATION Table 7.9 shows the product characteristics the manufacturer Hamamatsu provides for the SiPM arrays *S12* and *S13*. The test conditions in which Hamamatsu measured these characteristics are a temperature of 25°C, a wavelength of the incident light of 450 nm and a bias voltage of $V_{\mathrm{Break}} + 2.4\,\mathrm{V}$ for array *S12* and $V_{\mathrm{Break}} + 3\,\mathrm{V}$ for array *S13*. A recommended bias voltage for every individual channel of both arrays was also included in the product information with the SiPM arrays. The QADC measurements to obtain information about the characteristic SiPM parameters in this thesis were performed at a temperature of (19.5 ± 1)°C, bias voltages of 67.6 V and 55.2 V and with a wavelength of 423 nm. Hamamatsu provides a temperature coefficient $\Delta V_{\mathrm{break}}$ for the breakdown voltage which gives information about how the breakdown voltage changes when the SiPM is operated at different temperatures:

$$\Delta V_{\mathrm{Break},S12} = 54\frac{\mathrm{mV}}{^{\circ}\mathrm{C}} \tag{7.25}$$

$$\Delta V_{\mathrm{Break},S13} = 60\frac{\mathrm{mV}}{^{\circ}\mathrm{C}}. \tag{7.26}$$

The recommended bias voltages for the two arrays can be calculated by using the measured average breakdown voltages for the SiPM arrays *S12* and *S13* shown in table 7.8 and the recommended over-voltages of 2.4 V for array *S12* and 3 V for array *S13*. The recommended bias voltages for measurements at 19.5°C would be 67.02 V for array *S12* and 54.65 V for array *S13*. The bias voltages for the measurements in this thesis are a compromise between a sufficient number of visible peaks in the finger spectra and a low optical power, since the noise of the used LEDs increases with optical power produced by them. Focusing on a sufficient signal-to-noise ratio, the recommended bias voltages were disregarded leading to a used over-voltage which is for both arrays higher then recommended $(+(0.58 \pm 0.10)\,\mathrm{V}$ for array *S12* and $+(0.55 \pm 0.12)\,\mathrm{V}$ for array *S13*).

Keeping this in mind, the measured values for gain, PDE and crosstalk probability should be bigger then the data sheet information and the breakdown voltage should be smaller. Regarding the dark-count rate, the situation is a bit more difficult since the dark-count rate decreases for lower temperatures but increases for higher over-voltages. A statement about whether the decrease caused by the lower temperature or the increase by the higher over-voltage is more dominant can not be made in this thesis and needs further investigations. Also the measurements of the dark-count rate can not provide hints, since for the measurement temperature of 19.5°C the result of the average dark-count rate of SiPM array *S12* is about 0.9 MHz lower then the typical data sheet value and the result for SiPM array *S13* is 0.15 MHz higher.

	S12642	S13361
Wavelength Sensitivity Range (nm)	320 - 900	270 - 900
Breakdown Voltage (V)	65 ± 10	53 ± 5
Gain ($E + 06$)	1.25	1.70
PDE (%)	35	40
Typ. Dark-Count Rate (MHz)	2	0.5
Crosstalk Probability (%)	-	3

Table 7.9: Information about the wavelength sensitivity range, the breakdown voltage, the gain, the PDE, the typical dark-count rate and the crosstalk probability the manufacturer Hamamatsu states in the data sheets of the SiPM arrays *S12* and *S13* for a temperature of 25°C [46, 47]. For SiPM array *S12*, no crosstalk probability was given by the manufacturer.

A suggestion is possible since the temperature dependence of the breakdown voltage of array *S13* is slightly higher then for array *S12*: A more temperature depended breakdown voltage like it is the case for array *S13* might be a hint on a more over-voltage depended dark-count rate behaviour since the over-voltage is changing faster with temperature compared to array *S12*, leading to a higher dark-count rate for lower temperatures. Vice versa, a less temperature depended breakdown voltage might be a sign of a more temperature depended dark-count rate behaviour leading to a lower dark-count rate.

Regarding breakdown voltage, gain, PDE and crosstalk probability the measured values change as expected compared to the manufacturers information. The measured breakdown voltages decrease, gain, PDE and crosstalk probability increase. The gain of both arrays increase by roughly the same amount of $0.4 \cdot 10^6$ for both arrays. Regarding array *S12*, the breakdown voltage and the PDE only change by a negligible amount into the right directions. Looking at the results for the new series array *S13* the change of breakdown voltage and PDE is more significant although the decrease of the breakdown voltage is higher then expected. For the SiPM array *S12*, no information about the crosstalk probability are given by the manufacturer. Regarding array *S13*, the crosstalk probability is higher than the manufacturer predicts as it is expected due to the higher over-voltage which was used in the measurements. All together, the measurement results are in accordance to the manufacturers information.

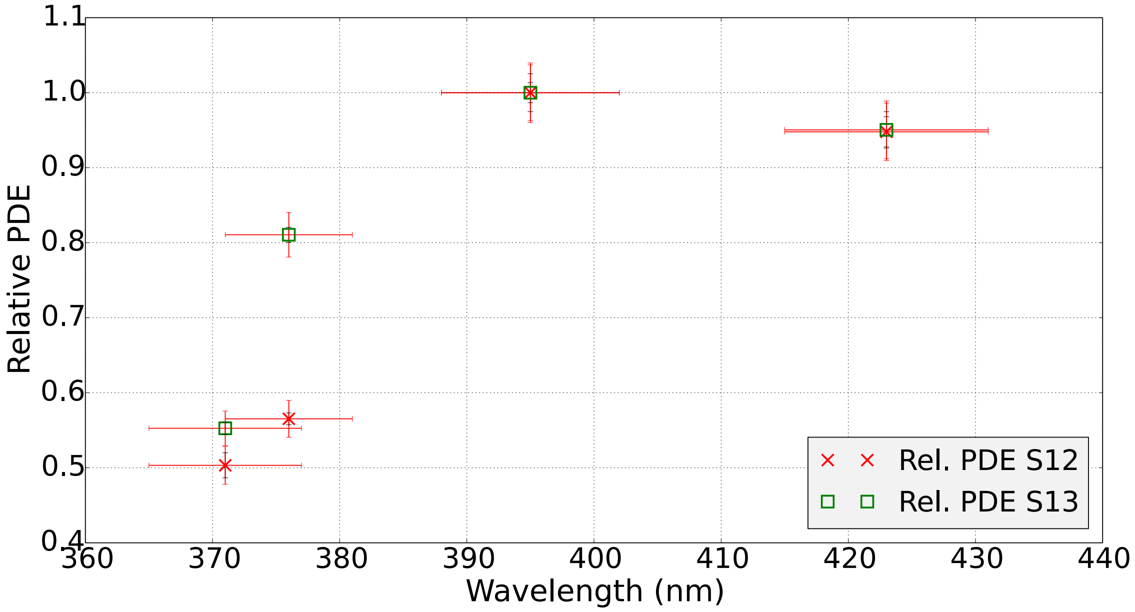

Figure 7.32: Comparison of the PDE for various wavelengths of the SiPM arrays *S12* and *S13*. The data points for the SiPM array *S12* are marked with a cross, those of the SiPM array *S13* as squares. The y-axis shows the relative PDE, normalized on the highest measured PDE value for each SiPM. The systematic and statistical uncertainties are shown with red and black error bars.

Regarding the uniformity of the SiPM channels of both arrays, the results are sufficient. Differences of breakdown voltages between individual SiPM channels within one array in the regime of 0.15 V can easily be balanced by using an ASIC like the mentioned *Citiroc* [36]. Focusing on a uniform gain over the whole array, a standard deviation of the average gain of about 3.3% for the *S13* SiPM array is sufficiently low to also be handled easily by the ASIC.
However, the channel to channel fluctuations of the measured parameters within one array are partly larger than the estimated total uncertainty. More measurements of more arrays are required to decide if these are related to real variations or an additional unidentified systematic effect of the measurement.

The wavelength sensitivity

The results for the PDE at different wavelengths of 423 nm, 395 nm, 376 nm and 371 nm for both SiPM arrays are shown in figure 7.32. The data of the SiPM array *S12* is shown with a cross, the data of the SiPM array *S13* is presented with squares. The relative PDE is plotted on the y-axis to be able to compare the behaviour of the two SiPM arrays. The relative PDE is the measured PDE normalised to the highest measured PDE value which was for both SiPM arrays at a wavelength of 395 nm. For the wavelength 423 nm the behaviour of the two SiPM arrays is similar. For wavelengths < 395 nm the sensitivity of the new series SiPM array *S13* is not so fast decreasing than of the older SiPM array *S12* and has a higher relative PDE for both wavelengths 376 nm and 371 nm. A reason for this is the different resins which covers the SiPM. The SiPM array *S13* is covered with a silicone resin which has a higher acceptance for low range wavelengths then the epoxy resin with which the SiPM array *S12* is covered.

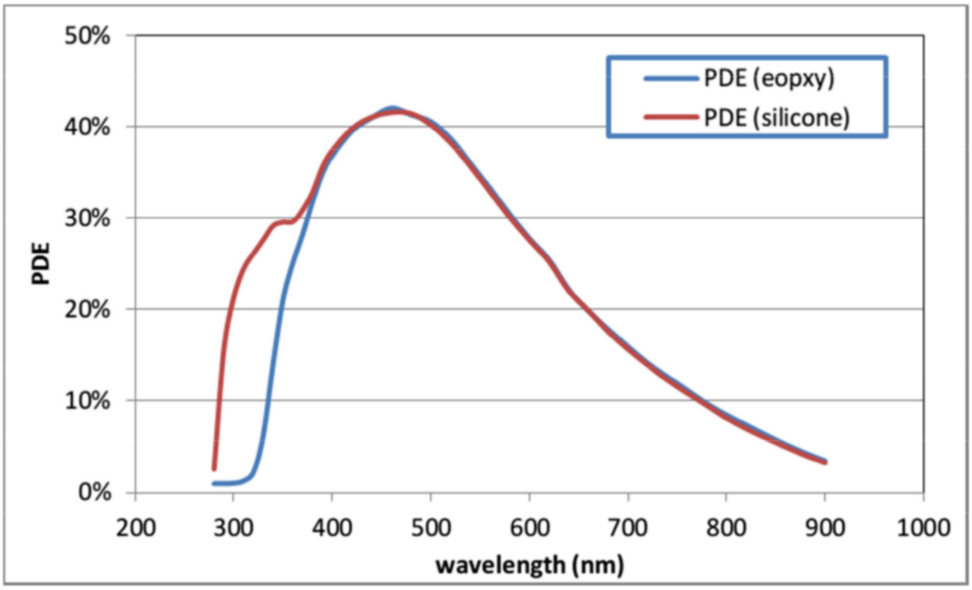

Figure 7.33: Prediction for the wavelength sensitivity for a silicone resin and an epoxy resin covered SiPM array *S13* made by the manufacturer Hamamatsu [46][1].

Figure 7.33 shows a plot from the data sheet of SiPM array *S13* made by the manufacturer Hamamatsu [46]. In the plot the wavelength sensitivity for a SiPM array *S13* with epoxy and with silicone resin is shown. For wavelengths above 400 nm the behaviour of both resins is similar. For wavelengths shorter then 400 nm the silicone resin has a better acceptance of shorter wavelengths leading to a better PDE and a lower minimal detectable wavelength. In the range of the four measured wavelengths, the measurement can confirm this predicted behaviour.

Response behaviour

Figure 7.34 shows the combined measurement results of the response behaviour with increasing light intensity of the SiPM arrays *S12* and *S13*. The data points of the array *S12* are shown as crosses, those of array *S13* with squares. The ideal SiPM response

---

[1] The misprint in 'epoxy' is originally in the data sheet of Hamamatsu.

meaning one firing S-APD per incoming photon per pulse is included in the plot as a black dotted line.

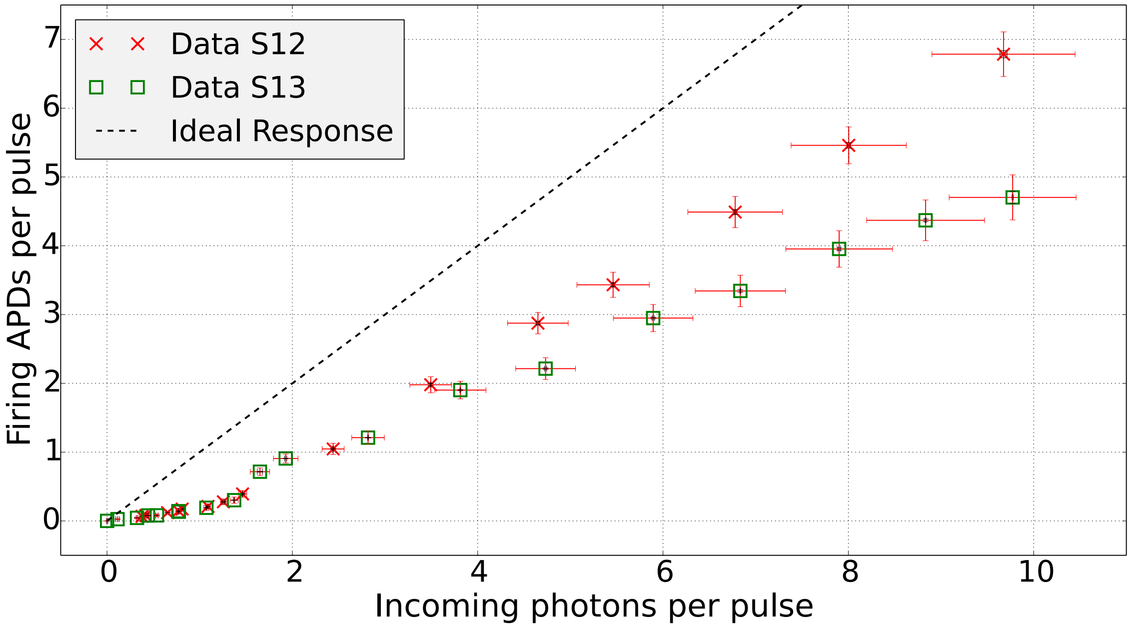

Figure 7.34: Comparing plot of the response behaviour measurements of the SiPM arrays *S12* and *S13*. The data points of array *S12* are shown as crosses, for array *S13* the data is presented with squares. The systematic and statistical uncertainties are shown with red and black error bars. The ideal SiPM response meaning one firing S-APD per incoming photon is included as a dotted line.

Both SiPM have not a linear behaviour from the start but raise until the response behaviour begins to have the expected linear form after around one incident photon per pulse, which was already mentioned and discussed in sections 7.2.1 and 7.3.1. A suggestion about the reason of this behaviour for less then one incident photon might be the insufficient number of measured QADC values. A test of this hypothesis was no more possible during this thesis.

Above around one incoming photon per pulse the inclination of the linear response of the older series SiPM array *S12* is bigger then for the newer SiPM array *S13* and is nearer at the ideal response behaviour of a SiPM although the the SiPM array *S12* has a lower photo detection efficiency.

A possible reason for this is the higher dark-count rate and crosstalk probability of the older *S12* SiPM array. Due to the measurement method, it can not be distinguished between real signals and dark counts or crosstalk events. These are added to the number of photon induced firing S-APDs resulting in a 'better' response behaviour. A deeper investigation of this discrepancy by correcting the measurements for crosstalk and dark-count events was also not possible during this thesis, but should be done in near future.

TEMPERATURE DEPENDENT MEASUREMENTS OF SIPM ARRAY *S13*

Temperature dependent measurements of the breakdown voltage, the gain, the PDE, the dark-count rate and the crosstalk probability were made with channel E4 of SiPM array *S13*. The ambient temperature was cooled down with water ice in a SiPM measurement cooling box consisting of insulation styrofoam covered with a styrofoam lid. The SiPM was placed inside of the cooling box in front of a ~ 5 x 5 cm wide window cut into one side of the box. The measurements were made while the temperature in the box heated up. The temperature was monitored with the temperature sensor *DS18B20* [64] which was placed next to the SiPM array. Figure 7.35 shows the temperature development during the measurement time. After around 500 minutes of the start, the lid of the SiPM measurement cooling box was opened and closed again. After around 530 minutes the lid was removed from the box to accelerate the temperature increase. Beside of the two times in which the lid was removed and the following normalization of the temperature, measurements were made during the whole time of temperature increase.

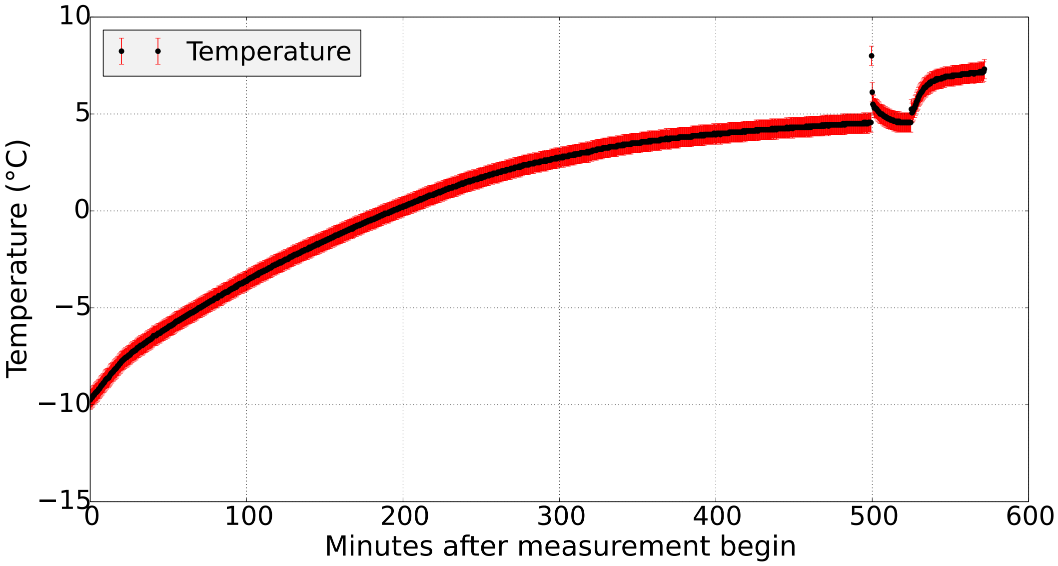

Figure 7.35: Temperature development during the temperature dependent measurements of channel E4. The temperature was measured and with the temperature sensor *DS18B20*.

The obtained values for breakdown voltage, gain, PDE, dark-count rate and crosstalk probability were measured with the QADC as explained in section 4.5 and the last two sections.

BREAKDOWN VOLTAGE Figure 7.36 shows the results for the breakdown voltage measurements vs. the ambient temperature. The breakdown voltage follows the expected linear behaviour like it was supposed in 4.3. The results for the linear fit of the breakdown voltage values is

$$V_{\mathrm{break}}(T) = (0.078 \pm 0.006)\frac{V}{^{\circ}C} \cdot T + (50.514 \pm 0.240)\,V\,. \tag{7.27}$$

The temperature coefficient which gives information about the breakdown voltage behaviour regarding the temperature is measured as

$$\Delta V_{\mathrm{Break},S13} = (78 \pm 6)\frac{mV}{^{\circ}C}. \tag{7.28}$$

Regarding the statistical uncertainties of the measured breakdown voltages, a firm statement about the temperature coefficient can not be made. The temperature coefficient provided by the manufacturer Hamamatsu as $\Delta V_{\mathrm{Break},S13} = 60mV/^{\circ}C$ for the SiPM array *S13* is significantly off the measured value.

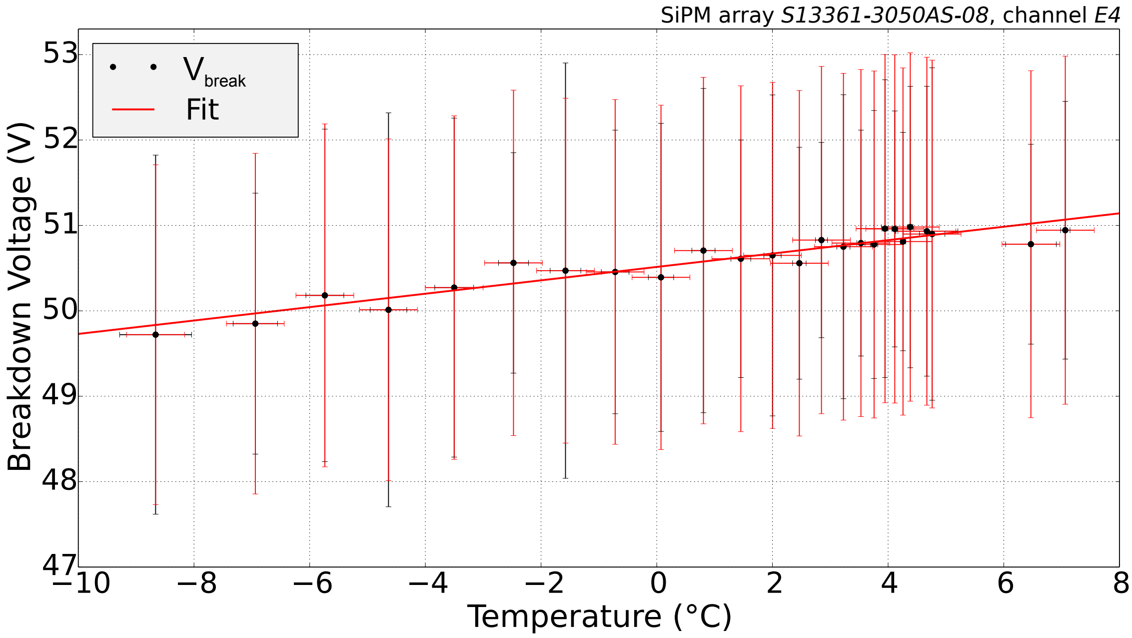

Figure 7.36: Breakdown voltage vs. the ambient temperature. The systematic and statistical uncertainties are shown with red and black error bars. The breakdown voltage follows the expected linear behaviour.

GAIN The results of the gain measurement at a bias voltage of 55.2 V are shown in figure 7.37. Like it is shown in figure 4.7, a linear behaviour of the gain is expected.

The measured gain values confirm this expectation. The result for the linear fit $G(T)$ shown in figure 7.37 as a solid line is

$$G(T) = -0.032\frac{10^6}{^\circ C} \cdot T + (2.648 \pm 0.002) \cdot 10^6. \tag{7.29}$$

The gain of channel E4 measured in section 7.2 at a temperature of $(19.5 \pm 1)^\circ C$ is

$$G_{E4,meas.}(19.5^\circ C) = (2.12 \pm 0.1_{stat} \pm 0.14_{sys}) \cdot 10^6. \tag{7.30}$$

The result for the gain at a temperature of $19.5^\circ C$ calculated with equation 7.29 is

$$G_{E4,calc.}(19.5^\circ C) = 2.02 \cdot 10^6. \tag{7.31}$$

This result is in good accordance with the measured value.

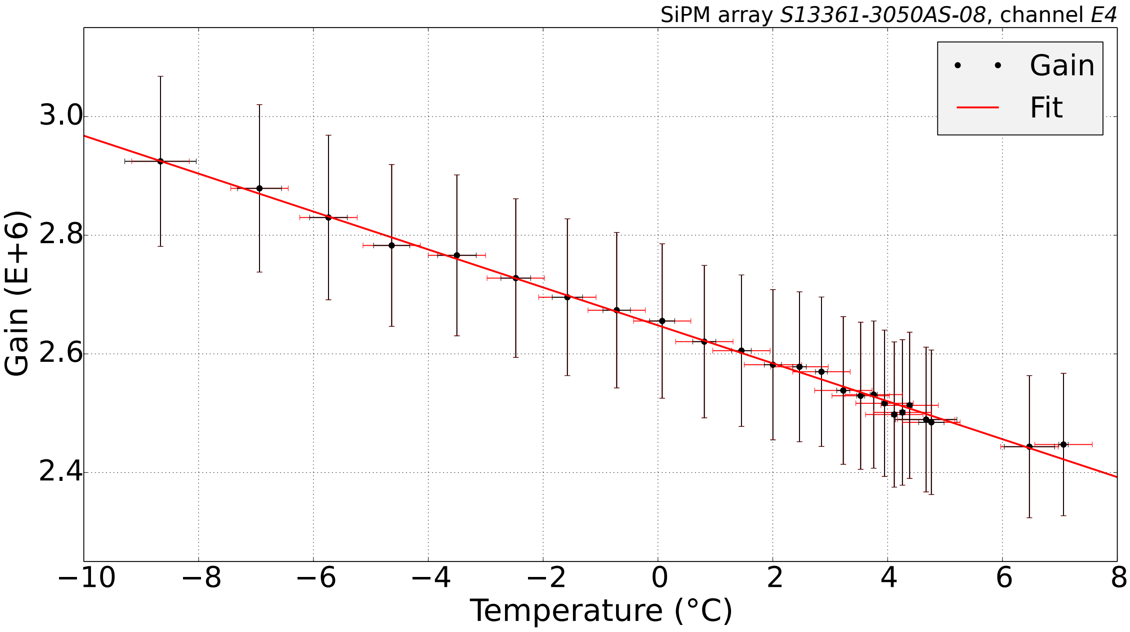

Figure 7.37: Gain vs. the ambient temperature. The uncertainties are shown with red and black error bars. The bias voltage was 55.2 V. The incident light had a wavelength of 423 nm.

PDE The results for the PDE are shown in figure 7.38. With increasing temperature, the breakdown voltage decreases (see fig. 7.36). In the PDE measurement shown in figure 7.38 the SiPM was biased with a constant voltage of 55.2 V. Therefore, the over-voltage decreased with increasing temperature. The expected behaviour of the PDE regarding the over-voltage is an increase of PDE with increasing over-voltage [42]. This means the PDE should decrease with increasing temperature when the SiPM is biased with a constant voltage. The measured PDE values do not follow this expected behaviour. For temperatures under the freezing point the PDE rises, after the freezing point the PDE values seem to fall again but are more randomly distributed.

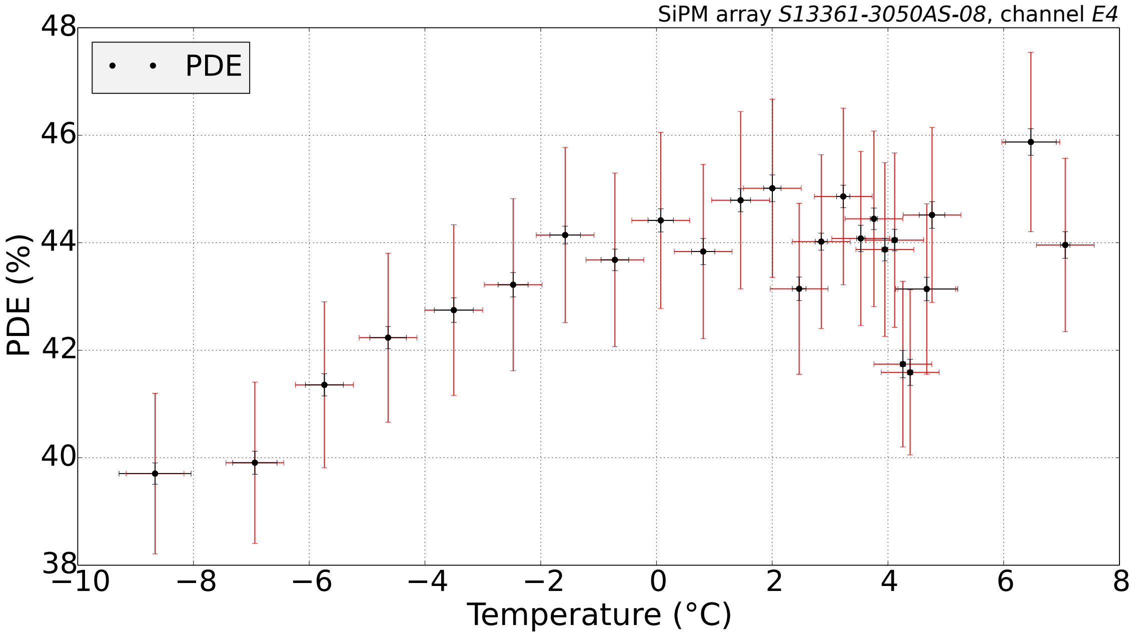

Figure 7.38: PDE vs. the ambient temperature at a bias voltage of 55.2 V. The incident light had a wavelength of 423 nm. The systematic and statistical uncertainties are shown with red and black error bars.

The PDE is the only measured SiPM characteristic that is sensitive to fluctuations in the number of incoming photons. This rather strange behaviour of the PDE could be caused by an ice layer at the SiPM's surface during the measurement holding up photons to penetrate the SiPM. The SiPM was cooled down inside the cooling chamber. Although the SiPM surface was cleaned from ice before the measurement, a new layer might have been build up before the first measurements. With increasing temperature the ice layer became thinner which results in a higher PDE. Above the freezing point the ice melted and water might have covered parts of the SiPM surface leading to the more random like distribution for temperatures higher then zero degrees.

DARK-COUNT RATE Figure 7.39 shows the dark-count rate measurement results. An increase in dark-count rate with an increase in temperature is clearly visible like it is expected. For a constant gain, the dark-count rate $\xi(T)$ should follow equation 4.9:

$$\xi(T) = A \cdot T^{3/2} \cdot e^{\frac{E_g}{2 \cdot k_B \cdot T}}. \tag{7.32}$$

In this measurement the bias voltage of the SiPM was kept constant and the gain decreased with increasing temperature (see fig. 7.37). Therefore, equation 4.9 is not valid for this measurement. In the measured region the fit

$$\xi(T) = (4.55 \pm 0.03) \cdot 10^{-33}\,\mathrm{Hz} \cdot T(K)^{15.4} \tag{7.33}$$

gives the best results. For a temperature of 19.5°C the dark-count rate ξ_{calc} calculated with equation 7.33 is

$$\xi_{calc} = 4.36 \cdot 10^{5}\,\mathrm{Hz}. \tag{7.34}$$

The dark-count rate measured during the characterisation measurements is

$$\xi_{meas} = (6.81 \pm 0.03_{stat} \pm 0.35_{sys}) \cdot 10^{5}. \tag{7.35}$$

The measured dark-count rate at a temperature of 19.5°C is not reproduced by the fit. Since the measured temperature region is small and the fit is chosen to reproduce only the measured dark-count rate values in this region, this is acceptable. Further measurements in a wider temperature region might give information about the dark-count rate behaviour at higher and lower temperatures. Never the less the strong dependency of the dark-count rate regarding the temperature is clearly visible.

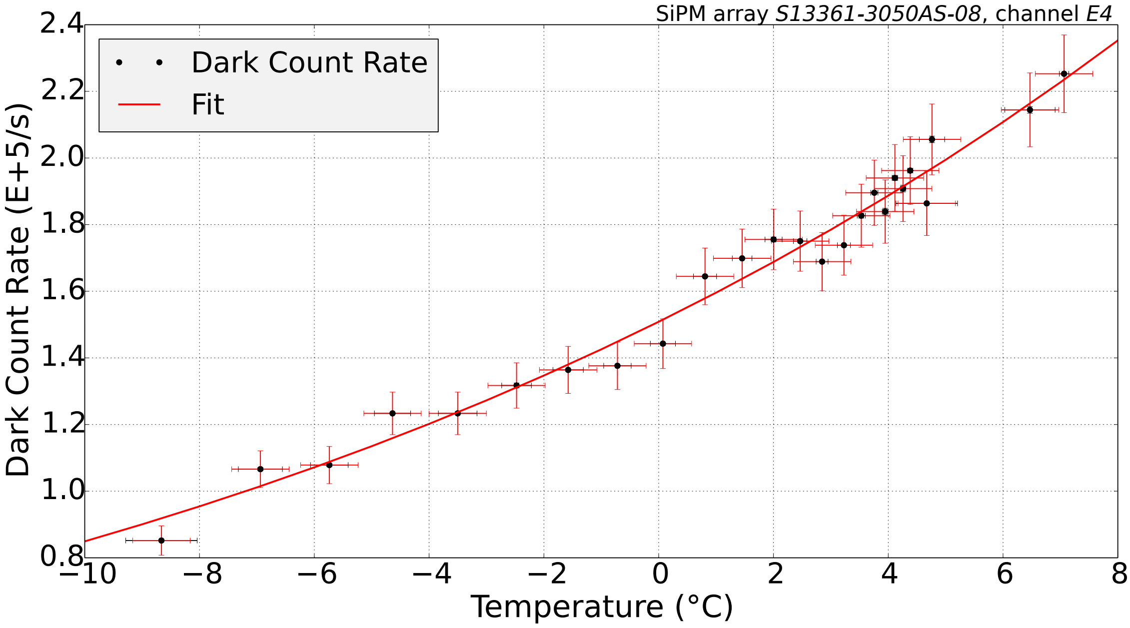

Figure 7.39: Dark-count rate ξ vs. the ambient temperature. The systematic and statistical uncertainties are shown with red and black error bars. The SiPM was biased with a voltage of 55.2 V.

CROSSTALK PROBABILITY The results of the temperature dependent measurement of the crosstalk probability are shown in figure 7.40. The crosstalk probability should decrease with decreasing over-voltage [42]. Therefore the crosstalk probability should decrease with increasing temperature regarding the present measurement setup. Regarding the measured values for the crosstalk probability in figure 7.40, a statement about the change of the crosstalk probability with temperature is hard to make. A linear fit $\epsilon(T)$ was made of the measured data points. The fit results are

$$\epsilon(T) = (-0.004 \pm 0.033)\frac{\%}{^{\circ}\mathrm{C}} \cdot T + (4.793 \pm 0.142)\%. \tag{7.36}$$

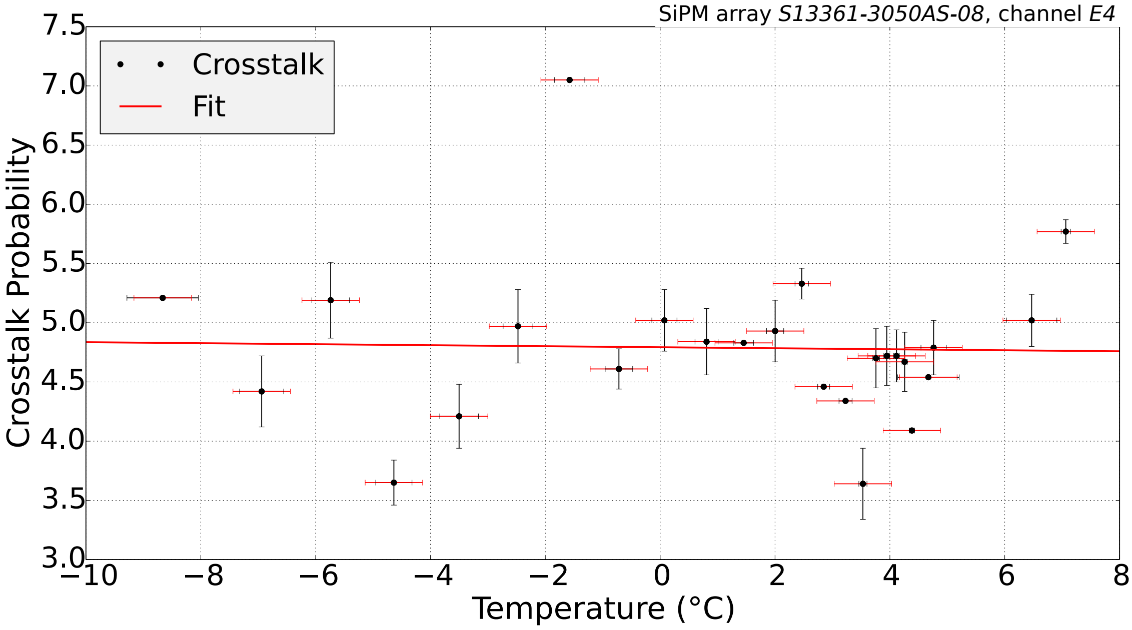

Figure 7.40: Crosstalk probability vs. the ambient temperature at a bias voltage of 55.2 V. The systematic and statistical uncertainties are shown with red and black error bars.

Although the fit results indicate a decrease of the crosstalk probability with increasing temperature, a firm statement can not be given. A reason for this insufficient result is the number of recorded QADC values for this measurement. In every recorded 70,000 QADC values set are only around 2 - 10 crosstalk events. A more precise result might be possible with a larger number of recorded data points. A second measurement was no more possible during this thesis.

8

SUMMARY AND OUTLOOK

The main aim of this thesis was to characterize new SiPM arrays regarding an operation at the Silicon Elementary Cell Add-On SiECA.
This thesis was performed within the frame of the development of new photodetectors for the fluorescence light detection generated by extensive air showers of ultra-high energy cosmic rays. In particular, it is settled within the JEM-EUSO experiment which shall measure UHECRs by observing the Earth's atmosphere from space. According to the baseline design of the experiment, Multi Anode Photomultiplier Tubes (MAPMTs) with 64 channels detect fluorescence photons emitted during an cosmic ray induced EAS. In the last years, SiPM manufacturers improved their SiPM products in a way that an investigation about a possible replacement of the base-line PMTs with SiPM is appropriate. Comparing to PMTs, SiPM have several advantages like a low bias voltage not located in the high voltage regime and a light-weight and robust structure. Especially, regarding an operation in a space-based experiment like JEM-EUSO, these benefits can not be disregarded.

To test a SiPM-based detection of EAS in the near space, SiECA is currently under development at KIT and will fly in the JEM-EUSO prototype mission EUSO-SPB with a super pressure balloon provided by NASA. SiECA will be equipped with four 64 channel SiPM arrays which are located beside of a down-scaled JEM-EUSO prototype focal surface made out of conventional MAPMTs. Two possible SiPM array candidates manufactured by Hamamatsu were available for SiECA. A former series SiPM array *S12642-0808PA-50* (*S12*) and a SiPM of the current series *S13361-3050AS-08* (*S13*). Beside of a stated better performance of the actual series array by the manufacturer, an important difference is the resin of the two arrays. While the former series array *S12* is covered with an epoxy resin which allows photon detection down to a wavelength of 320 nm, the actual series array is equipped with a silicone resin enabling photon detection down to wavelengths of 270 nm. Especially for the detection of UV fluorescence light like it is the purpose of the JEM-EUSO telescope, this is an important difference.

To check the manufacturers information and to investigate the more suitable SiPM array for an operation within SiECA, SiPM characterization measurements have been prepared and performed during this thesis. In addition, temperature dependent measurements of SiPM characteristics of the actual SiPM series *S13* have been made to investigate the expected strong temperature dependency of SiPM.
To enable characterization measurements with 64 channel SiPM arrays, read-out boards

had to be designed and measurement control and analysing software had to be programmed. Two sets of SiPM array read-out boards have been developed to meet different working situations. In a first version read-out board, the individual SiPM array channel is selected manually by closing a jumper connection and the signal amplification has to be arranged externally. In a second version read-out board the actual laboratory equipment is used to remotely select a channel. The SiPM characterisation of the whole array measurement can be performed automatically with a suitable amplification board. In addition to the read-out boards, a SiPM read-out system was developed, including the remote selection of individual channels, a signal amplification and an internal power supply for the SiPM array. Measurements of both SiPM arrays were performed with the first version read-out board.

The characterisation measurements show that the actual series SiPM array *S13* improves in all of the measured characteristic values like breakdown voltage, gain, Photo Detection Efficiency (PDE), dark-count rate and crosstalk probability. The average measured breakdown voltage of the array is (51.65 ± 0.12) V, the average gain is measured to $(2.12 \pm 0.7) \cdot 10^6$, the average photo detection efficiency results to $(44.60 \pm 1.78)\%$, the average dark-count rate is (0.68 ± 0.11) MHz and the crosstalk probability is measured to $(3.90 \pm 0.66)\%$. Also, the uniformity over the whole array is sufficient in the characteristic parameters to build up a focal surface of SiPM arrays fulfilling the requirements for a UV camera. Further measurements of the wavelength sensitivity in the range of $371 - 423\,\mathrm{nm}$ show the positive effect of the silicone resin resulting in a considerable improvement in PDE for wavelengths shorter than $395\,\mathrm{nm}$. The response dynamic was measured for both arrays in the region of low photon numbers up to 11 incident photons per pulse which will be the situation for events detected with SiECA and the later JEM-EUSO experiment. The measurement shows a more ideal response behaviour of the former series array than of the actual one. Nevertheless, this result might not be an argument for the former series but shows the effect of a considerably lower crosstalk probability of the actual SiPM series *S13*.

As a conclusion of this thesis, the actual series SiPM array *S13* is due to the generally better performance and the new silicone resin resulting in an improved UV sensitivity the better choice and definitely suitable for SiECA. Regarding the measured SiPM characteristic parameters, the newest SiPM series can compete against the conventional MAPMTs. The analysis of the experimental data of EUSO-SPB and SiECA starting 2017 will give further hints on the performance of the SiPM in operation and about the readiness of a SiPM based fluorescence light telescope.

In the future, the measurement setup developed during this thesis will be used to characterize the four actual SiECA SiPM arrays. Regarding the possibility of replacing PMTs with SiPM in the base-line design of JEM-EUSO or further experiments, the work with SiPM in the field of research and development will expand. Especially regarding the noise discrimination, more research has to be done. Assuming no breakthrough of decreasing dark counts in further SiPM generations, the only way to decrease the dark-count rate is to cool the SiPM like the measurements within this thesis show. Regarding the use of SiPM arrays as fluorescence light detectors like in SiECA, an adapted trigger algorithm searching for coincidences in neighboured SiPM channels will also decrease the negative effects of a high dark-count rate. The work of this thesis is a good step to increase the efforts in this new field of research in silicon-based cosmic ray detectors.

9

APPENDIX

SIPM ARRAY LAYOUT

Channel naming and numbering for the SiPM arrays *S12642-0808PA-50* and *S13361-3050AS-08*.

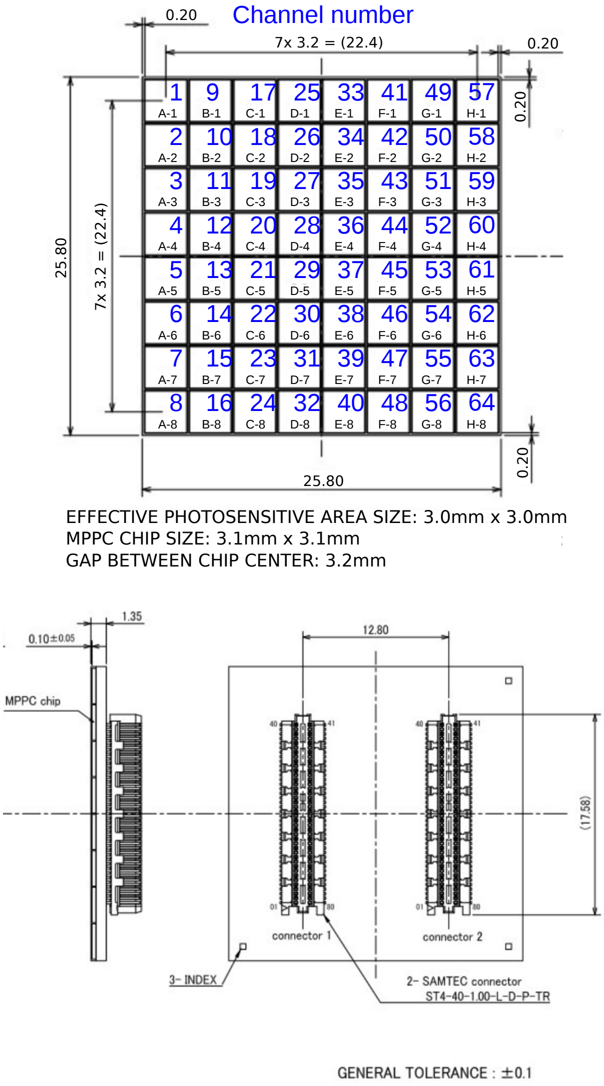

1 A-1	9 B-1	17 C-1	25 D-1	33 E-1	41 F-1	49 G-1	57 H-1
2 A-2	10 B-2	18 C-2	26 D-2	34 E-2	42 F-2	50 G-2	58 H-2
3 A-3	11 B-3	19 C-3	27 D-3	35 E-3	43 F-3	51 G-3	59 H-3
4 A-4	12 B-4	20 C-4	28 D-4	36 E-4	44 F-4	52 G-4	60 H-4
5 A-5	13 B-5	21 C-5	29 D-5	37 E-5	45 F-5	53 G-5	61 H-5
6 A-6	14 B-6	22 C-6	30 D-6	38 E-6	46 F-6	54 G-6	62 H-6
7 A-7	15 B-7	23 C-7	31 D-7	39 E-7	47 F-7	55 G-7	63 H-7
8 A-8	16 B-8	24 C-8	32 D-8	40 E-8	48 F-8	56 G-8	64 H-8

EFFECTIVE PHOTOSENSITIVE AREA SIZE: 3.0mm x 3.0mm
MPPC CHIP SIZE: 3.1mm x 3.1mm
GAP BETWEEN CHIP CENTER: 3.2mm

Figure 9.1: SiPM Channel names and layout for the SiPM arrays *S12642-0808PA-50* and *S13361-3050AS-08* [46].

DATA SHEET OF SIPM ARRAY *s12642-0808PA-50*

Part of the data sheet of SiPM array *S12642-0808PA-50* [47].

PRODUCT
FLYER

2014.03 KSX-I50014-E_S12642 Series（3mm□-TSV – Array）

PRELIMINARY

HAMAMATSU
PHOTON IS OUR BUSINESS

TSV MPPC array

S12642-0404PA-50: 3x3mm^2, 4x4ch, p50µm
S12642-0808PA-50: 3x3mm^2, 8x8ch, p50µm
S12642-1616PA-50: 3x3mm^2, 16x16ch, p50µm

■ Overview

TSV MPPC array is a COB (Chip on board) type MPPC array with a 3x3mm^2 effective photosensitive, using the TSV (Through Silicon Via) technology. There is no wire bonding, so the package outline is very close to the MPPC array. The outer gap from active area edge to package edge is only 0.2mm. The pitch between ch is 3.2mm This package realizes the 4-side buttable arrangement.

This MPPC is designed for the applications in the photon counting region, including medical, non-destructive inspection, high energy physics experiments, and many other fields.

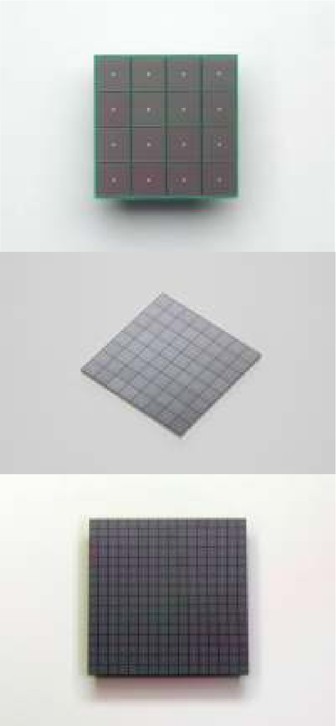

■ Features

- ➢ Significantly reduced after pulse
- ➢ Very compact package with small dead space
- ➢ Superior photon counting capability
- ➢ Low voltage (Vop=65V Typ.) operation
- ➢ High gain: 10^5 to 10^6

■ Application

- ➢ PET
- ➢ Nuclear medicine
- ➢ High energy physics experiment
- ➢ Celestial observation
- ➢ Environmental analysis

■ Structure

Parameters	Symbol	S12642 -0404PA-50	S12642 -0808PA-50	S12642 -1616PA-50	Unit
Number of channel	-	16 (4x4)	64 (8x8)	256 (16x16)	-
Effective photosensitive area / channel	-	3×3			mm^2
Pixel pitch	-	50			µm
Number of pixels / channel	-	3584			-
Geometrical fill factor	-	62			%
Package	-	Chip on board (Surface mount type)			-
Window	-	Epoxy resin			-
Window refractive index	-	1.55			-

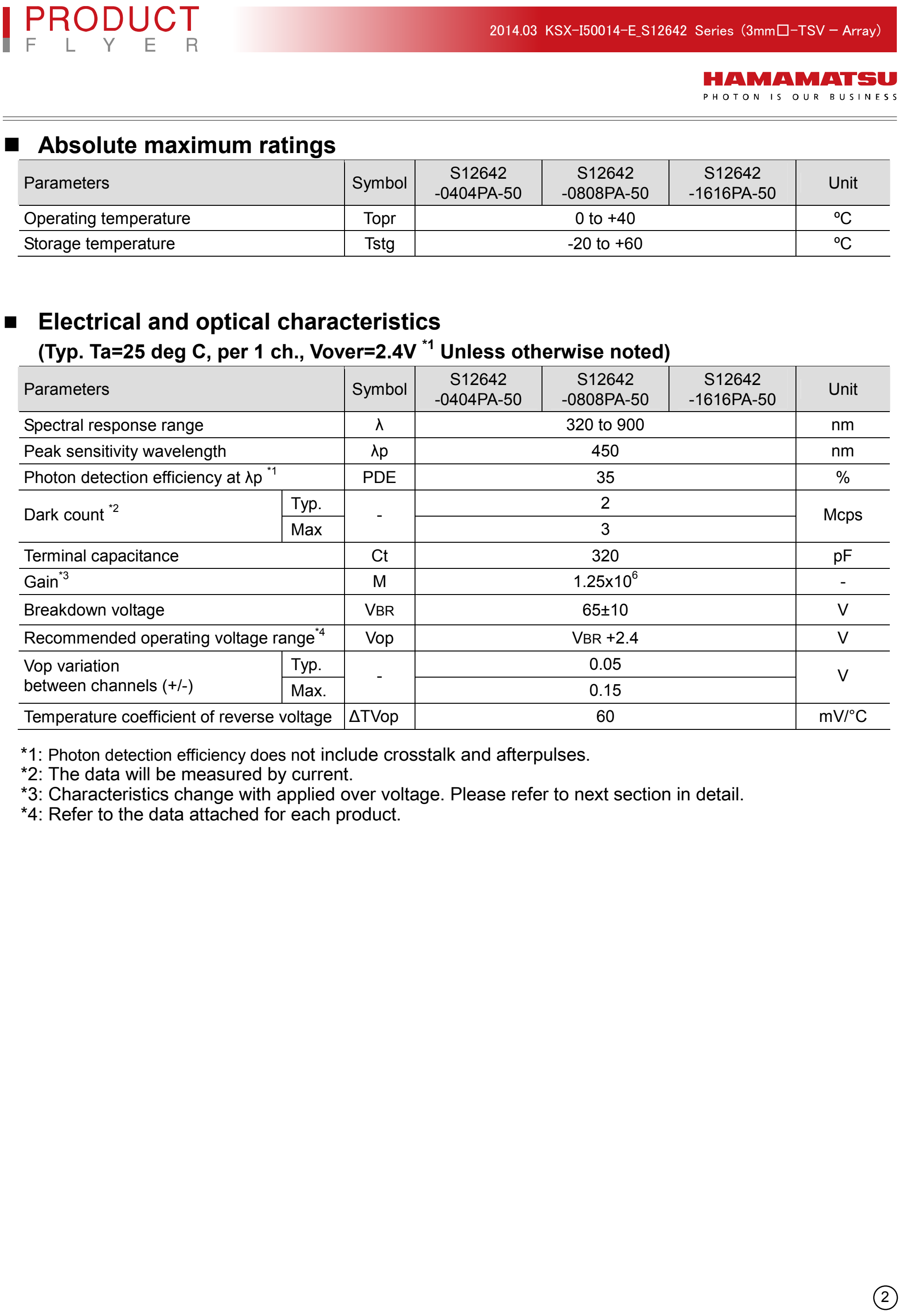

PRODUCT
FLYER

2014.03 KSX-I50014-E_S12642 Series (3mm□-TSV – Array)

HAMAMATSU
PHOTON IS OUR BUSINESS

■ Absolute maximum ratings

Parameters	Symbol	S12642 -0404PA-50	S12642 -0808PA-50	S12642 -1616PA-50	Unit
Operating temperature	Topr	0 to +40			℃
Storage temperature	Tstg	-20 to +60			℃

■ Electrical and optical characteristics

(Typ. Ta=25 deg C, per 1 ch., Vover=2.4V [*1] Unless otherwise noted)

Parameters		Symbol	S12642 -0404PA-50	S12642 -0808PA-50	S12642 -1616PA-50	Unit
Spectral response range		λ	320 to 900			nm
Peak sensitivity wavelength		λp	450			nm
Photon detection efficiency at λp [*1]		PDE	35			%
Dark count [*2]	Typ.	-	2			Mcps
	Max		3			
Terminal capacitance		Ct	320			pF
Gain [*3]		M	1.25×10^6			-
Breakdown voltage		V_{BR}	65±10			V
Recommended operating voltage range [*4]		Vop	V_{BR} +2.4			V
Vop variation between channels (+/-)	Typ.	-	0.05			V
	Max.		0.15			
Temperature coefficient of reverse voltage		ΔTVop	60			mV/°C

*1: Photon detection efficiency does not include crosstalk and afterpulses.
*2: The data will be measured by current.
*3: Characteristics change with applied over voltage. Please refer to next section in detail.
*4: Refer to the data attached for each product.

DATA SHEET OF SIPM ARRAY *S13361-3050AS-08*

Part of the data sheet of SiPM array *S13361-3050AS-08* [46].

PRODUCT
FLYER
2015.05 KSX-I50081-E_S13361-3050xx-08
HAMAMATSU
PHOTON IS OUR BUSINESS

TSV MPPC array

Low Cross Talk type

S13361-3050NE-08, S13361-3050NS-08
S13361-3050AE-08, S13361-3050AS-08

■ Overview

The S13361 series are the MPPCs for the precision measurements. The strongest point of these MPPCs is drastically reduced cross talk, compared to our previous products. The S13361 series use the TSV (Through Silicon Via) technology. There is no wire bonding, so the package outline is very close to the MPPC array. The outer gap from active area edge to package edge is only 0.2mm. The pitch between ch is 3.2mm. This package realizes the 4-side buttable arrangement.

These MPPCs are designed for the applications in the photon counting region, including medical, non-destructive inspection, environmental chemical analysis, high energy physics experiments, and many other fields.

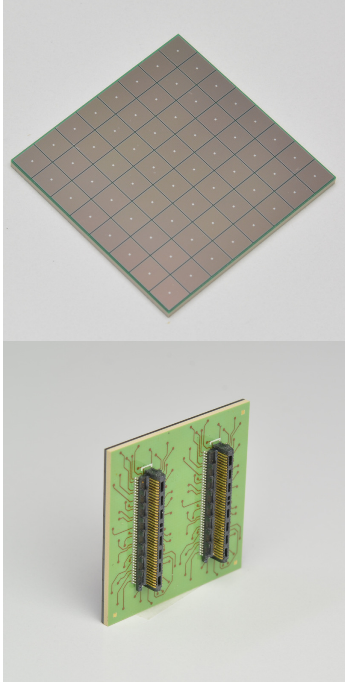

■ Features

- ➢ Significantly reduced Cross talk
- ➢ Low after pulse
- ➢ Very compact package with small dead space
- ➢ Superior photon counting capability
- ➢ Low voltage (Vop=53V Typ.) operation
- ➢ High gain: 10^5 to 10^6

■ Application

- ➢ Astro physical application
- ➢ High energy physics experiment
- ➢ Nuclear medicine
- ➢ PET
- ➢ Environmental analysis

■ Structure

Parameters	S13361				Unit
	-3050NE-08	-3050NS-08	-3050AE-08	-3050AS-08	
Effective photosensitive area	3x3				mm^2
Pixel pitch	50				μm
Number of pixels / channel	3584				-
Geometrical fill factor	74				%
Package	Surface mount type		Connector *		-
Window	Epoxy resin	Silicone resin	Epoxy resin	Silicone resin	-
Window refractive index	1.55				-

* SAMTEC Header ST4-40-1.00-L-D-P-TR is installed back side of the package.
This connector mates with: SAMTEC SS4-40-3.00-L-D-K-TR.
See detail at http://www.samtec.com/ftppub/pdf/ss4.pdf

Absolute maximum ratings

Parameters	Symbol	S13361-3050NE-08 S13361-3050NS-08	S13361-3050AE-08 S13361-3050AS-08	Unit
Operating temperature[*1]	Topr	-20 to +60		°C
Storage temperature[*1]	Tstg	-20 to +80		°C
Reflow Soldering conditions	Tsol	Peak temperature: 240 °C, twice (see below) [*2]	-	-

*1: No condensation
*2: JEDEC level 5a

Electrical and optical characteristics
(Typ. Ta=25 deg C, Vover=3V unless otherwise noted)

Parameters		Symbol	S13361-3050NE-08, S13361-3050AS-08 S13361-3050NE-08, S13361-3050AS-08	Unit
Spectral response range		λ	320 to 900 (NS, AE type)	nm
			270 to 900 (NS, AS type)	
Peak sensitivity wavelength		λp	450	nm
Photon detection efficiency at λp [*3]		PDE	40	%
Dark count [*4]	Typ.		0.5	Mcps
	Max.		1.5	
Crosstalk probability		-	3	%
Terminal capacitance		Ct	320	pF
Gain [*5]		M	1.7x10^{6}	-
Breakdown voltage		V_{BR}	53 ±5	V
Recommended operating voltage [*6]		V_{op}	V_{BR} +3	V
Temperature coefficient of recommended reverse voltage		ΔT_{Vop}	54	mV/ °C

*3: Photon detection efficiency does not include crosstalk and after pulse.
*4: The data will be measured by current.
*5: Characteristics change with applied over voltage. Please refer to next section in detail.
*6: Refer to the data attached for each product.

Measured example of temperature profile with our hot-air reflow oven for product testing

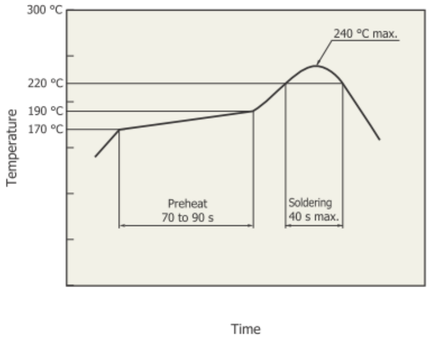

- This product supports lead-free soldering. After unpacking, store it in an environment at a temperature of 25 °C or less and a humidity of 60% or less, and perform soldering within 24 hours.

- This effect that the product receives during reflow soldering varies depending on the circuit board and reflow oven that are used. Before actual reflow soldering, check for any problems by testing out the reflow soldering methods in advance.

ACKNOWLEDGEMENTS

First of all, I want to thank Prof. Dr. Johannes Blümer for giving me the chance to write my masters thesis in the frame of this very interesting field of astro-particle physics. Also, I want to thank Prof. Dr. Ivan Perić for agreeing as second examiner.

I kindly thank Dr. Andreas Haungs for guiding me through the time of my thesis and to give me the possibility to participate in several collaboration meetings. Although there were fortunately not many occasions for this, I always had the feeling that I can ask for advice and help any time I need it.

A special thanks goes to my colleagues Francesca Bisconti, Michael Karus, Thomas Huber and William Painter. Without your help and advise, this thesis would not have been possible. I want to thank you also for the very friendly and warm working atmosphere. Mainly because of you, I was pleased every day to come to work.

Without the help of Bernd Hoffmann, I would not have come so far. He helped me out with every technical problem I had and answered all my questions coming up during this year in his own calm and very friendly kind. Also I want to thank him for all the soldering work he made for me. I apologize for the lack of soldering talent I certainly have.

Finally, I want to thank Sabine Bucher for finding solutions for every administration problem I had, Dr. Harald Schieler, Andeas Weindl and the whole staff of IKP/IEKP for their help and friendly company.

BIBLIOGRAPHY

[1] Gregor Herten. "The First Year of the Large Hadron Collider: A Brief Review." In: *Mod. Phys. Lett.* A26 (2011), pp. 843–855. DOI: 10.1142/S0217732311035687. arXiv: 1104.4205 [hep-ex].

[2] Domenico D'Urso. "Cosmic Ray Physics." In: (2014). arXiv: 1411.4642 [astro-ph.HE].

[3] Sidney R. Coleman and Sheldon L. Glashow. "Cosmic ray and neutrino tests of special relativity." In: *Phys. Lett.* B405 (1997), pp. 249–252. DOI: 10.1016/S0370-2693(97)00638-2. arXiv: hep-ph/9703240 [hep-ph].

[4] Jorge Alfaro and Gonzalo Palma. "Loop quantum gravity and ultrahigh-energy cosmic rays." In: *Phys. Rev.* D67 (2003), p. 083003. DOI: 10.1103/PhysRevD.67.083003. arXiv: hep-th/0208193 [hep-th].

[5] Jes Madsen. "Cosmic ray strangelets." In: *J. Phys.* G31 (2005), S833–S840. DOI: 10.1088/0954-3899/31/6/025. arXiv: astro-ph/0411601 [astro-ph].

[6] Wolfgang Bietenholz. "Cosmic Rays and the Search for a Lorentz Invariance Violation." In: *Phys. Rept.* 505 (2011), pp. 145–185. DOI: 10.1016/j.physrep.2011.04.002. arXiv: 0806.3713 [hep-ph].

[7] Alexander Aab et al. "The Pierre Auger Cosmic Ray Observatory." In: *Nucl. Instrum. Meth.* A798 (2015), pp. 172–213. DOI: 10.1016/j.nima.2015.06.058. arXiv: 1502.01323 [astro-ph.IM].

[8] P. Abreu et al. "The Pierre Auger Observatory V: Enhancements." In: *Proceedings 32nd International Cosmic Ray Conference (ICRC 2011)*. 2011. arXiv: 1107.4807 [astro-ph.IM]. URL: https://inspirehep.net/record/919727/files/arXiv:1107.4807.pdf.

[9] Toshikazu Ebisuzaki for the JEM-EUSO Collaboration. "The JEM-EUSO mission." In: *ArXiv e-prints* (Apr. 2012). 32nd International Cosmic Ray Conference , Beijing, 2011. arXiv: 1204.5065 [astro-ph.IM].

[10] Mario Bertaina, Pavol Bobik, and Francesco Fenu on behalf of JEM-EUSO Collaboration. *Expected Performances of the JEM-EUSO Mission*. URL: www.isas.jaxa.jp/j/researchers/symp/sss13/paper/P2-039.pdf.

[11] Victor F. Hess and Carl D. Anderson. *The Nobel Prize in Physics 1936: Award Ceremony Speech*. 1936. URL: http://www.nobelprize.org/nobel_prizes/physics/laureates/1936/press.html.

[12] Bruno Rossi. "Misure sulla distribuzione angolare di intensita della radiazione penetrante all'Asmara." In: (1934).

[13] P. Auger, P. Ehrenfest, R. Maze, J. Daudin, and R. A. Fréon. "Extensive Cosmic-Ray Showers." In: *Reviews of Modern Physics* 11 (July 1939), pp. 288–291. DOI: 10.1103/RevModPhys.11.288.

[14] G. W. Clark, J. Earl, W. L. Kraushaar, J. Linsley, B. B. Rossi, F. Scherb, and D. W. Scott. "Cosmic-Ray Air Showers at Sea Level." In: *Physical Review* 122 (Apr. 1961), pp. 637–654. DOI: 10.1103/PhysRev.122.637.

[15] Masaki Fukushima. "Recent Results from Telescope Array." In: *EPJ Web Conf.* 99 (2015), p. 04004. DOI: 10.1051/epjconf/20159904004. arXiv: 1503.06961 [astro-ph.HE].

[16] H.V. Klapdor-Kleingrothaus and K. Zuber. *Astroteilchenphysik*. Teubner Studienbuecher, 1997.

[17] Johannes Blümer, Ralph Engel, and Jörg R. Hörandel. "Cosmic rays from the knee to the highest energies." In: *Progress in Particle and Nuclear Physics* 63.2 (2009), pp. 293 –338. ISSN: 0146-6410. DOI: http://dx.doi.org/10.1016/j.ppnp.2009.05.002. URL: http://www.sciencedirect.com/science/article/pii/S0146641009000362.

[18] The KASCADE-Grande Collaboration et al. "The spectrum of high-energy cosmic rays measured with KASCADE-Grande." In: *ArXiv e-prints* (June 2012). arXiv: 1206.3834 [astro-ph.HE].

[19] Michael Karus. "Developement of a cailbration stand for photosensors for extremely high-energy cosmic ray research." PhD thesis. Karlsruhe Institut fuer Technologie (KIT), 2016.

[20] S. Schoo et al. "KASCADE-Grande Review, Recent Results, Future Endeavors." In: *JPS Conf. Proc.* 9 (2016), p. 010010. DOI: 10.7566/JPSCP.9.010010.

[21] Frank G. Schröder. "Radio detection of high-energy cosmic rays with the Auger Engineering Radio Array." In: *Nucl. Instrum. Meth.* A824 (2016), pp. 648–651. DOI: 10.1016/j.nima.2015.08.047. arXiv: 1601.00462 [astro-ph.IM].

[22] Miguel Mostafa. "Hybrid Detection of UHECR with the Pierre Auger Observatory." In: *Vulcano Workshop 2006: Frontier Objects in Astrophysics and Particle Physics Vulcano, Italy, May 22-27, 2006*. 2006. arXiv: astro-ph/0608005 [astro-ph].

[23] R. U. Abbasi et al. "Study of Ultra-High Energy Cosmic Ray composition using Telescope Array's Middle Drum detector and surface array in hybrid mode." In: *Astropart. Phys.* 64 (2015), pp. 49–62. DOI: 10.1016/j.astropartphys.2014.11.004. arXiv: 1408.1726 [astro-ph.HE].

[24] B. Keilhauer, M. Bohacova, M. Fraga, J. Matthews, N. Sakaki, Y. Tameda, Y. Tsunesada, and A. Ulrich. “Nitrogen fluorescence in air for observing extensive air showers.” In: *European Physical Journal Web of Conferences*. Vol. 53. European Physical Journal Web of Conferences. June 2013, p. 01010. DOI: `10.1051/epjconf/20135301010`. arXiv: `1210.1319 [astro-ph.HE]`.

[25] A. Santangelo, P. Picozza, and T. Ebisuzaki for the JEM-EUSO Collaboration. *Status of the JEM-EUSO Mission*. arXiv 1307.7071. 33re International Cosmic Ray Conference , Rio de Janeiro, 2013. URL: `https://arxiv.org/abs/1307.7071`.

[26] The JEM-EUSO Collaboration. *Report on the Phase A Study 2010 (Purple Book)*.

[27] J. Adams et. al. *An evaluation of the exposure in nadir observation of the JEM-EUSO mission*. Astroparticle Physics 44. 2013.

[28] The JEM-EUSO Collaboration. *The JEM-EUSO Instruments*. arXiv 1307.7071. 33re International Cosmic Ray Conference , Rio de Janeiro, 2013. URL: `https://arxiv.org/abs/1307.7071`.

[29] Yoshiyuki Takiizawa, Alessandro Zuccaro Marchi, and Toshikazu Ebisuzaki for the JEM-EUSO Collaboration. *The TA-EUSO and EUSO-Balloon optics designs*. arXiv 1307.7071. 33re International Cosmic Ray Conference , Rio de Janeiro, 2013. URL: `https://arxiv.org/abs/1307.7071`.

[30] The JEM-EUSO Collaboration. *Calibration and testing of a prototype of the JEM-EUSO telescope on Telescope Array site*. arXiv 1307.7071. 33re International Cosmic Ray Conference , Rio de Janeiro, 2013. URL: `https://arxiv.org/abs/1307.7071`.

[31] Francesca Bisconti. *Privat Comunication*. 2016. URL: `francesca.bisconti@kit.edu`.

[32] F Fenu et al. “Preliminary analysis of EUSO—TA data.” In: *Journal of Physics: Conference Series* 718.5 (2016), p. 052011. URL: `http://stacks.iop.org/1742-6596/718/i=5/a=052011`.

[33] M. Casolino et al. *EUSO-TA, a ground telescope at the telescope array to test JEM-EUSO detector performance*. 34st international cosmic ray conference , The Hague, 2015. PoS(ICRC2015)636.

[34] The JEM-EUSO Collaboration. *EUSO-BALLOON : a pathfinder for observing UHECR's from space*. arXiv 1307.7071. 33re International Cosmic Ray Conference , Rio de Janeiro, 2013. URL: `https://arxiv.org/abs/1307.7071`.

[35] Lawrence Wiencke for the JEM-EUSO Collaboration. *EUSO-Balloon mission to record extensive air showers from near space*. 34st international cosmic ray conference , The Hague, 2015. PoS(ICRC2015)631. URL: `userpages.irap.omp.eu/~pvonballmoos/eusoballoon/publications_files/34-0816-euso_spb_wiencke3.pdf`.

[36] Weeroc. *Citiroc Datasheet*. URL: http://www.weeroc.com/asic-products/citiroc-1.

[37] William Painter. "Private communication." In: *Institute of Experimental Nuclear Physics (IEKP) - Karlsruhe Institute of Technology (KIT)* (2016). URL: william.painter@kit.edu.

[38] Hamamatsu Corperation. *Datasheet SiPM power supply C11204-02*. 2014.

[39] SensL. *An Introduction to the Silicon Photomultiplier*. URL: www.sensl.com/downloads/ds/TN%20-%20Intro%20to%20SPM%20Tech.pdf.

[40] Alexander Tadday. "Characterisation Studies of Silicon Photomultipliers." In: *Kirchhoff-Institut fuer Physik, Universitaet Heidelberg* (2010).

[41] Slawomir Piatek. *Physics and operation of an MPPC*. Hamamatsu Corporation and New Jersey Institute of Technology. 2014. URL: http://www.hamamatsu.com/us/en/community/optical_sensors/sipm/physics_of_mppc/index.html.

[42] Hamamatsu Corperation. *Hamamatsu Handbook*. 2014.

[43] G.A. Baraff. "Maximum anisotropy approximation for calculating electron distributions; application to high field transport in semiconductros." In: *Physical Review* 133 (1964), pp. 26 –33.

[44] Chen Xu. "Study of the silicone photomultipliers and their applications in positron emission tomography." PhD thesis. Universität Hamburg, 2014.

[45] Samtex. *Samtec SS4 Razor Beam Datasheet*. URL: https://www.samtec.com/products/ss4#related.

[46] Hamamatsu Corperation. *Datasheet 64 channel SiPM array S13361 series*. 2015.

[47] Hamamatsu Corperation. *Datasheet 64 channel SiPM array S12642 series*. 2014.

[48] Thomas Huber. "Silicon Photomultiplier for the space-based fluorescence telescope JEM-EUSO." MA thesis. Karlsruhe Institut fuer Technologie (KIT), 2016.

[49] Simon Ehnle. "Calibration of a charge-integrating analog-digital converter and test measurements of multianode photomultiplier tubes." In: *Bachelor thesis* (2016). Karslruhe Institut für Technologie.

[50] Keysight Technologies. *Datasheet Agilent E3612A*.

[51] Tektronix. *Datasheet PWS2000 Series*.

[52] Thurlby Thandar Instruments. *Datasheet EL Series*.

[53] Bernd Hoffmann. "Private communication." In: *Institute of Experimental Nuclear Physics (IEKP) - Karlsruhe Institute of Technology (KIT)* (2015). URL: bernd.hoffmann@kit.edu.

[54] Stefano Vercellone. "The ASTRI mini-array within the future Cherenkov Telescope Array." In: *EPJ Web Conf.* 121 (2016), p. 04006. DOI: 10.1051/epjconf/201612104006. arXiv: 1508.00799 [astro-ph.IM].

[55] D. Impiombato et al. “Characterization and performance of the ASIC (CITIROC) front-end of the ASTRI camera.” In: *Nucl. Instrum. Meth.* A794 (2015), pp. 185–192. DOI: `10.1016/j.nima.2015.05.028`. arXiv: `1506.00264 [physics.ins-det]`.

[56] Sonja Schneidewind. *Ongoing Bachelor thesis at IKP, KIT*. Private Communication.

[57] Analog Devices Inc. *Datasheet ADG1606*.

[58] Analog Devices Inc. *Datasheet ADG704*.

[59] Michael Karus for the JEM-EUSO Collaboration. “Calibration of photo sensors for the space-based cosmic ray telescope JEM-EUSO.” In: *Karlsruhe Institut fuer Technologie (KIT)* (2015). URL: `http://dx.doi.org/10.1063/1.4909600`.

[60] Pro-Lite Technology. *Spectralon Reflectance Material*. 2016. URL: `http://www.pro-lite.co.uk/File/spectralon_material.php`.

[61] Hamamatsu Corperation. *Datasheet driver circuit for MPPC C12332-01*. 2015. URL: `http://www.hamamatsu.com/jp/en/product/category/3100/4004/4149/C12332-01/index.html`.

[62] Texas Instruments. *Datasheet Amplifier IC OPA864*. URL: `http://www.ti.com/product/OPA846`.

[63] CAEN Costruzioni Apparecchiature Elettroniche Nucleari S.p.A. *Datasheet QADC CEAN v965*. 2008. URL: `http://www.caen.it/csite/CaenProd.jsp?parent=11&idmod=398`.

[64] Dallas Semiconductor. *Datasheet Temperature Sensor DS18B20*. URL: `www.dalsemi.com`.